

**Robust, Fast and High Resolution Multimode Fiber
Endoscopes**

by

Sakshi Singh

B. Tech, Amrita Vishwa Vidyapeetham, 2015

M.S., University of Colorado Boulder, 2018

A thesis submitted to the
Faculty of the Graduate School of the
University of Colorado in partial fulfillment
of the requirements for the degree of
Doctor of Philosophy
Department of Electrical Engineering
2021

Committee Members:

Rafael Piestun, Chair

Kelvin Wagner, Robert Mcleod, Shu-Wei Huang, Hervé Rigneault

Singh, Sakshi (Ph.D., Electrical Engineering)

Robust, Fast and High Resolution Multimode Fiber Endoscopes

Thesis directed by Prof. Rafael Piestun

Current optical imaging techniques to image inside biological matter are limited in penetration to a depth of about a millimeter due to the highly scattering nature of tissue. Multimode fibers (MMF), with their small footprint, high resolution and efficient light collection make excellent candidates for minimally invasive endoscopes that can potentially go much deeper inside tissue. Light propagating through an MMF however experiences modal dispersion and inter-modal coupling, leading to a random speckle pattern on the other end. Imaging through them requires a means of controlling the illumination on the object and measuring the return signal from the object for many such controlled illuminations. Wavefront shaping enables this control by employing an interferometric calibration of the fiber's input-output relationship or transmission matrix.

In this thesis, we address three main challenges in MMF imaging: robustness, speed and resolution. We first present a technique to improve the MMF imaging speed and simplify the calibration process by employing the naturally occurring speckle patterns at the MMF output for scanning the object. By combining the return signals for different speckle illuminations with a reconstruction algorithm, the object can be recovered using fewer measurements from a simpler and more robust system.

Secondly, we demonstrate high-speed wavefront shaping using a one-dimensional modulator operating at 350 kHz, known as a grating light valve (GLV). We characterize the wavefront shaping performance of the modulator, present an optimal optical configuration to maximize its performance and show record speed of focusing light through an MMF using it, hence paving the way to faster MMF imaging.

Furthermore, we demonstrate mode control through an MMF with more than 7000 modes. With the achieved mode tunability, we can select a smaller subset of modes to create focal spots

at the fiber output and characterize the bend sensitivity of different mode groups within the fiber mode set. We show that certain modes of the fiber are more resilient to bending than others.

Finally, we present a technique to achieve the optical sectioning and resolution gain of confocal imaging, while retaining a high signal to noise ratio. The technique generalizes the principles of image scanning microscopy to complex media and enables a practical solution to achieve optical sectioning for imaging 3-D samples with high resolution by employing multiple virtual pinholes to collect the back-scattered light from the endoscope.

Dedication

Dedicated to my Mom, Dad and Eashan

Acknowledgements

This thesis would not have been possible without the support and encouragement of my mentors, peers, friends and family who have stayed with me through thick and thin in this incredible graduate school journey.

Firstly, I would like to thank my advisor, Prof. Rafael Piestun for accepting me in his research group and giving me the opportunity to pursue my Ph.D. under his supervision. He has inspired me every step of the way and motivated me to keep pushing through the challenges of research. I want to convey my sincerest gratitude to him for being the ideal advisor and an enthusiastic well-wisher throughout graduate school.

I would also like to thank my thesis committee members, Prof. Kelvin Wagner, Prof. Hervé Rigneault, Prof. Robert Mcleod and Prof. Shu-Wei Wang for their time in providing me constructive feedback and useful suggestions that have helped improve my thesis. I am also thankful to Prof. Juliet Gopinath, Prof. Robert Mcleod, Prof. Alan Mickelson, Prof. Shu-Wei Wang, Prof. Kelvin Wagner and Dr. Tony Barsic, for providing me all the foundation in optics essential for my research endeavors.

Furthermore, I would like to convey my heartfelt thanks to my mentors and friends from Piestun group, Dr. Antonio Caravaca and Dr. Omer Tzang for teaching me experimental optics from scratch and sharing their words of wisdom about research and life in general. I also want to thank Dr. Simon Labouesse for providing his fresh perspectives to my work, for teaching me optimization algorithms and for the countless brainstorming sessions.

A big thanks to my lab members and friends Evolene Premillieu, Haiyan Wang and Sarah

Kerr for all the thought-provoking conversations and for keeping life in the lab interesting and fun. I also want to thank all my other Boulder friends who made life outside the lab enjoyable and became my second family away from home.

Finally, I am grateful beyond words can express to my family, especially my mom, dad and brother, who have always been supportive of my decisions and have cheered for me to get past all challenges and to keep growing into a better version of myself.

Contents

Chapter

1	Introduction	1
1.1	Optical fibers	2
1.2	State of the Art in minimally invasive endoscopy	3
1.2.1	Single modes fibers (SMFs)	4
1.2.2	Gradient index (GRIN) lenses	5
1.2.3	Multicore fibers (MCFs)	5
1.2.4	Multimode fibers (MMFs)	6
1.3	Light propagation through a multimode fiber	7
1.3.1	Helmholtz equation	7
1.3.2	Step-index fibers	8
1.3.3	Graded-index fibers	10
1.3.4	Dispersion in MMFs	11
1.4	MMF Imaging using the transmission matrix method	13
1.4.1	Calibration	13
1.4.2	Scanning	15
1.5	Multimode fiber imaging timeline	15
1.6	Current challenges and benchmarks	17
1.6.1	Speed	18
1.6.2	Robustness	18

1.6.3	Optical sectioning and resolution	20
1.7	Thesis overview	21
2	Speckle imaging through multimode fibers	24
2.1	Introduction	24
2.2	Methods	26
2.2.1	Calibration	26
2.2.2	Scanning	27
2.2.3	Reconstruction algorithm	28
2.3	Selection of speckle patterns for best compression	30
2.4	Resolution limit	32
2.5	Experimental Setup	33
2.6	Results	35
2.6.1	Fluorescence imaging	35
2.6.2	Influence of speckle pattern selection	36
2.7	Hybrid photoacoustic and fluorescence imaging	38
2.8	Conclusion	40
2.9	Appendix	41
2.9.1	Fast iterative shrinkage-thresholding algorithm (FISTA) for sparsity constrained optimization problems	41
3	High speed focusing using a 350 kHz wavefront modulator	43
3.1	Introduction	43
3.2	2D control through scattering media using a 1D modulator	46
3.2.1	Model of a scattering medium with memory effect	47
3.2.2	Speckle shape analysis	47
3.3	Experimental Setup	48
3.4	Results	51

3.4.1	Focusing through a ground glass diffuser and dynamic media	51
3.4.2	Focusing through multimode fibers	55
3.4.3	Statistical analysis of enhancement	56
3.5	Discussion	57
3.6	Conclusion	58
3.7	Appendix	59
3.7.1	Phase calibration of the GLV	59
3.7.2	Experimental speckle shape and enhancement for different illumination configurations	61
3.7.3	Analysis of factors affecting focus enhancement	62
4	Tunable mode control through multimode fibers	67
4.1	Introduction	67
4.2	Mode control in the fiber mode basis	69
4.3	Experimental setup	72
4.4	Results	73
4.5	Discussion and conclusion	79
4.6	Appendix	81
4.6.1	Focusing with mode control outside the optimal region of a mode set	81
4.6.2	Comparison of efficiency statistics of experimental and digitally computed mode-controlled output fields	83
4.6.3	Enhancement statistics of experimental and digitally computed mode-controlled output fields	83
4.6.4	Influence of mode selection on robustness	85
4.6.5	Mode control metrics	86
5	Multiview Scattering Scanning Imaging Confocal Microscopy through a Multimode Fiber	89
5.1	Introduction	89

5.2	Principle of image scanning microscopy	92
5.3	Generalized Matrix Formalism	93
5.4	Principle of MUSSIC microscopy through a multimode fiber	96
5.5	Methods	98
5.5.1	Calibration of forward TM, T	98
5.5.2	Calibration of backward TM, T^b	99
5.5.3	Optimal inversion of backward TM and band-pass filtering	100
5.5.4	Bandpass filtering, normalization and mean subtraction	100
5.5.5	Imaging without full field back-propagation	101
5.6	Experimental Setup	102
5.7	Results	103
5.7.1	SNR and resolution analysis	103
5.7.2	Experimental results	106
5.8	Discussion and conclusions	107
5.9	Appendix	110
5.9.1	MUSSIC reconstruction from a system with different excitation and detection PSFs	110
5.9.2	Generalized MUSSIC microscopy using speckle illumination	110
5.9.3	Effect of Normalization in image reconstruction	111
5.9.4	MUSSIC Reconstructions using different inversion strategies	111
6	Summary, future work and outlook	113
6.1	Summary	113
6.2	Future Work	115
6.2.1	Improving speed and SNR in speckle imaging through Multimode fibers . . .	115
6.2.2	Towards high SNR fluorescence imaging with optical sectioning through MMFs	115
6.2.3	Faster MUSSIC microscopy and better reconstruction algorithm	116

6.2.4	Deep learning for learning the multimode fiber model	116
6.2.5	Towards in-vivo microscopy with deep penetration in live animals	117
6.3	Outlook	117

Bibliography		119
---------------------	--	------------

Tables

Table

S1	Efficiency calculations for the experimental fields w.r.t to the target fields and fidelity and RMSE calculations for experimental intensities w.r.t the target intensities. . . .	87
S2	Efficiency calculations for the digitally computed fields w.r.t to the target fields and fidelity and RMSE calculations for digitally computed intensities w.r.t the target intensities.	87
S3	Cross-fidelity and RMSE calculations between digitally computed and experimental output intensities.	88

Figures

Figure

1.1	Schematics of different types of optical fibers on the basis of number of propagating modes and refractive index profile.	2
1.2	State of the art endoscopes	4
1.3	Example mode field solutions for a GRIN fiber with a parabolic index profile	11
1.4	Schematic of imaging through MMFs using the TM method	14
1.5	Timeline of multimode fiber imaging	17
1.6	Thesis Overview	23
2.1	Principle of speckle illumination imaging through a MMF	27
2.2	Correlations in experimentally recorded speckle patterns	31
2.3	Resolution in speckle imaging	32
2.4	Experimental setup for speckle imaging	33
2.5	Experimental results for fluorescence speckle imaging through an MMF	35
2.6	Effect of speckle pattern optimization	37
2.7	Hybrid photoacoustic and fluorescence imaging through an MMF	39
3.1	State of the art wavefront shaping technology	44
3.2	Model of a scatterer with memory effect	46
3.3	Speckle shape analysis for different illumination configurations	49
3.4	Experimental Setup for focusing through scattering media using a grating light valve	50

3.5	Focusing through a ground glass diffuser and dynamic scattering samples using the GLV	52
3.6	Enhancement as a function of number of modes used for TM measurement	54
3.7	Focusing through a multimode fiber using the GLV	55
3.8	Statistics of GLV focusing performance as a function of pixel ratios and number of modes	56
3.9	Experimental calibration of the GLV	61
3.10	Speckle shape and enhancement comparison for image and Fourier plane illumination configurations	62
3.11	Simulation of enhancement as a function of the number of optimized modes for various GLV imperfections	63
3.12	Background signal due to the inter-pixel gaps in the GLV	65
3.13	First order diffraction efficiency for different horizontal locations of the GLV pixel array	66
4.1	Illustration of methods for mode control in the fiber mode basis	68
4.2	Illustration of mode control for focusing through a fiber using its transmission matrix	71
4.3	Experimental setup for mode control and focusing through an MyF	72
4.4	Experimental demonstration of focusing with mode control	74
4.5	Statistics of mode control through MyFs as a function of radial location of the focal spots and the number of modes selected for optimization.	75
4.6	Experimental demonstration of bending resilience of focal spots created using different mode sets	78
4.7	Experimental demonstration of focusing with mode control outside the optimal regions of the respective mode sets	82
4.8	Average efficiency of focal spots as a function of their radial location	83
4.9	Enhancement as a function of radial position and mode selection	84

4.10	Experimental demonstration of bending resilience of focal spots created with and without mode selection	85
5.1	Principle of resolution and SNR gain in image scanning microscopy	93
5.2	Generalized matrix formalism for imaging through complex media	95
5.3	Principle of MUSSIC microscopy in complex media	98
5.4	Experimental setup for image scanning microscopy through an MMF	103
5.5	Comparison of confocal and MUSSIC image reconstructions	105
5.6	SNR comparison in MUSSIC microscopy	107
5.7	Comparison of optical sectioning in MUSSIC microscopy and conventional single pixel imaging through multimode fibers	108
5.8	Effect of normalization on image reconstruction	112
5.9	Comparison of MUSSIC reconstructions using different inverse estimates of the backward TM	112

Chapter 1

Introduction

Endoscopes are powerful imaging tools that have enabled huge advances in medicine. While the concept of examining the inaccessible parts of the body has been around since the ancient times, the actual term, endoscopy was coined in the 1850s by Antonin Jean Desormeaux. By the end of the nineteenth century, endoscopes had become common tools for examining body cavities such as the bronchial, gastro-intestinal and urethral passages. However the lack of availability of viable illumination sources that could be safely transported to the region of interest was a major deterrent to further advances.

The emergence of fiber optics brought about a change in this scene when Harold Hopkins developed a fibroscope consisting of a bundle of flexible glass fibres that could coherently transmit an image. The next few years saw a rapid improvement in the design, efficiency and miniaturization of fiber optic systems, which opened doors to various life saving endoscope-assisted as well as purely endoscopic surgical procedures.

However, thus far, the applications of endoscopes have been limited only to body cavities. The large footprint of current endoscopes prohibits their use in in-vivo microscopy. In this Thesis we propose a minimally invasive single- multimode fiber endoscope capable of deep-tissue penetration for enabling in-vivo micro-endoscopy. In what follows, we review some general concepts around different types of fiber endoscopes and multimode fibers (MMFs). We also present a literature review of multimode fiber imaging research followed by a discussion of current benchmarks and open challenges in the field. Finally, we end the chapter with an overview of this Thesis.

1.1 Optical fibers

Optical fibers are transparent waveguides typically made of glass or polymers that can guide light through them by the principle of total internal reflection. They typically consist of two regions: a high refractive index core which confines the light and a lower refractive index cladding that surrounds the core. They can be broadly classified into two types- single and multimode fiber. Single mode fibers (SMFs) support a single mode and have a small core with a diameter of a few microns. Multimode fibers (MMFs) on the other hand supports multiple modes and have core diameters in the range of 10-100 microns.

MMFs can be further classified on the basis of the refractive index profile of the core into step and graded index (GRIN) MMFs. While the step index fibers have a constant core index, the GRIN fibers have a radially varying graded index profile. The gradual decrease in index from the center of the core towards the cladding helps minimize modal dispersion. A schematic of an SMF and step-index and GRIN MMFs is shown in Fig 1.1 .

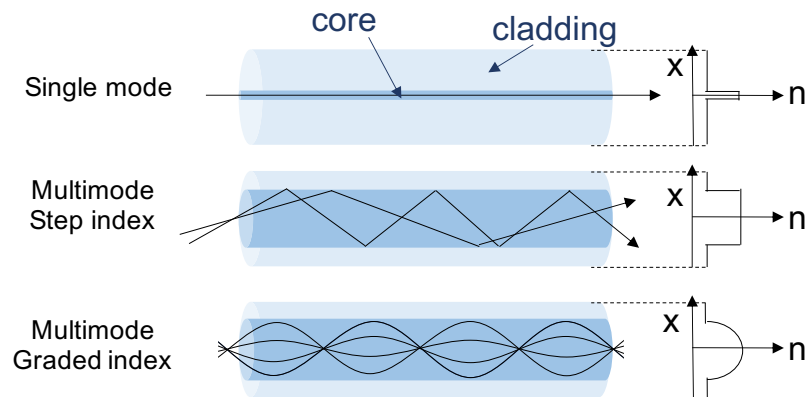


Figure 1.1: Schematics of different optical fibers on the basis of number of propagating modes and refractive index profile. The refractive index (n) profile of each of the fiber cross-sections is shown on their right. Ray trajectories in different fibers are also depicted. In a single mode fiber, the incident light can only propagate in a straight path through the fiber. In a multimode step-index fiber, the light that enters within the acceptance cone reflects back and forth from the core-cladding interface. In contrast the rays in a graded index fiber bend gradually due to the gradually changing refractive index inside the core.

Besides the two standard types above, there are specialty fibers that are designed for specific applications. An example is Multicore fibers (MCFs) that have multiple cores embedded in a common cladding within a single fiber. These are made from all-glass fiber technology where an index variation due to a varying glass composition is the guiding mechanism. MCFs can be useful as they can support as many independent modes as the number of cores within a single strand of flexible fiber.

Photonic crystal fibers (PCFs) are another type of optical fibers that consist of a microstructured arrangement of air holes inside another higher refractive index material such as undoped silica. PCFs can have either a solid core like conventional optical fibers or a hollow core. Light propagation in solid and hollow-core fibers is governed by the effective index model and the Photonic Bandgap (PBG) effect respectively. Hollow-core PCFs are especially useful for delivering high peak power ultrashort pulses due to their low loss and non-linear effects [16, 102].

Fibers can also be classified on the basis of the number of claddings they have. Double clad fibers (DCFs) that have a separate inner and outer cladding of different refractive indices are useful for various endoscopic applications. These are often used to decouple the regions of illumination and detection in endoscopic applications to improve collection efficiency.

1.2 State of the Art in minimally invasive endoscopy

Modern endoscopes are largely made either using one of the optical fibers mentioned in the previous section, their hybrids, or miniature rod lenses. We describe below each of the above types in more detail along with their advantages and disadvantages for endoscopic applications. A summary of the cross-sectional diameters and the advantages and disadvantages of all the types is provided in figure 1.2. The outer diameter for the optical fibers corresponds to their cladding diameter.

Type	Typical cladding diameter	Advantages	Disadvantages
Fiber bundle	0.25-few millimeters	Memory effect eliminates mechanical scanning, low dispersion	Bulky, low light throughput to thickness ratio, pixelation artefacts
Single mode fiber	80-125 microns	Flexible, preserves phase information, no dispersion	Needs mechanical scanning, low light throughput although can be improved using a double clad fiber, sensitive to misalignment
GRIN lens	0.35-2 millimeters	Compact, high tolerance to perturbation, low dispersion	Rigid, prone to aberrations, FOV smaller than diameter, cannot be made longer without increasing thickness
Multicore fiber	125-300 microns	Memory effect eliminates mechanical scanning, low dispersion	Low light throughput without a double cladding, replicas due to core periodicity limit FOV, sensitive to bending
Multimode fiber	125-300 microns	Maximum light throughput, many degrees of freedom	Prone to modal and chromatic dispersion, highly sensitive to bending

Figure 1.2: Summary of current state of the art endoscopes

1.2.1 Single modes fibers (SMFs)

Most widely used endoscopes consist of SMF bundles [66, 86, 172] where each fiber is used to relay one pixel of image information. These fibers exhibit low dispersion and a phenomenon called the memory effect, which allows laterally shifting the distal illumination by tilting the incident wavefront sent through the fiber, hence eliminating the need for a distal scanning mechanism. However, the field of view (FOV) is limited by the range of memory effect. Moreover, these bundles are bulky and rigid with a typical thickness of a few millimeters. The core in SMFs is only about a few microns in diameter and comprises a small fraction of the fiber cross-sectional area, which limits their light carrying capacity and leads to pixelation in images. While they are quite useful for imaging within body cavities, inserting them through soft tissue can cause significant

damage.

Alternatively, a single SMF equipped with a scanning mechanism on its far or distal side such as a MEMS mirror or a piezo actuator has been used as a flexible endoscope [99, 136]. However, despite the advantage of flexibility they have low throughput unless separate fibers are used for light collection, which makes it bulky. The use of DCFs [70, 27] as endoscopes, where the core is used for guiding the excitation light and the collection is done through the inner cladding which is larger in area and supports multiple modes, has also shown to improved collection efficiency. Moreover, with an optimized photonic crystal fiber design that minimizes group velocity dispersion (GVD) and pulse distortion, these fibers can enable high quality nonlinear imaging modalities such as two photon excitation (TPE) imaging, coherent anti-Stokes Raman scattering (CARS) imaging and second harmonic generation (SGH) imaging [116]. However the need for a scanning mechanism at the distal tip for both these types of endoscopes limits their robustness and makes them difficult to miniaturize.

1.2.2 Gradient index (GRIN) lenses

GRIN lenses are another popular choice of endoscopes which have a parabolic radial refractive index profile and behave like conventional lenses except, they are miniature rods. These are more compact with typical diameters of 500 microns and can be used for multiple imaging modalities such as confocal microscopy [108] TPE imaging [13], CARS imaging [193] and SGH imaging [152]. However, they are prone to optical aberrations, which limit their FOV and image quality. Thin GRIN lenses are also short in length and hence have limited penetration. Furthermore, their rigidity limits their maneuverability inside tissue.

1.2.3 Multicore fibers (MCFs)

Endoscopes made using MCFs have also been gaining interest due to their various advantages [11] such as minimal inter-core coupling, low dispersion compared to MMFs, and a number of independent degrees of freedom dictated by the number of cores in a single fiber strand. Other

advantages include the memory effect which eliminates the need for a distal scanning mechanism [168, 170], as described earlier for SMF bundles. MCFs can also be employed for non-linear imaging [44, 168] due to their low dispersion characteristics. Moreover, MCFs often have a large collection efficiency when the fiber is double-clad and the inner cladding is used for light collection, however the second cladding increases the fiber footprint. MCFs also have their own set of drawbacks such as difficulty of fabrication and scalability. Moreover, the imaging field of view is limited by the occurrence of replicas due to the periodicity of the cores.

1.2.4 Multimode fibers (MMFs)

MMFs on the other hand, can support thousands of modes in a hair-thin cross-section of 100 μm , making them the highest bandwidth, minimally invasive endoscope of a given cross-sectional area. Moreover, the large number of degrees of freedom allows creating complex field distributions at their distal end and enables high resolution imaging through them, limited by their numerical aperture (NA), when a means of shaping the incident illumination is available. They also do not require a mechanical scanning mechanism and are low cost and easy to fabricate. All these ideal endoscopic characteristics however are also accompanied with a few challenges.

MMFs are prone to modal dispersion and inter-modal coupling, which needs to be compensated for, to enable imaging through them. Furthermore, the output of an MMF is sensitive to bending and other perturbations which can affect imaging quality when they are used in a dynamic environment. The dispersion also makes non-linear imaging through MMFs challenging. Luckily linear imaging can be accomplished through MMFs by means of wavefront shaping [145, 83, 30]. Furthermore, combined with methods for compensating temporal dispersion, nonlinear imaging [126, 166, 50, 175] has also been successfully demonstrated through MMFs. There have also been various effective attempts in dealing with the problem of fiber bending [58, 30, 83, 65, 78, 105]. Methods for further improvement still remain an interesting area of research.

Despite the challenges, the efficient design of MMFs and their immense potential as a minimally invasive endoscope provide compelling reasons for further investigation into MMF imaging

and makes it the central topic of this Thesis. In the following sections, we provide a background into the basic principles, origin, existing work and current benchmarks for imaging through MMFs which will unveil the motivation behind the work presented in this Thesis.

1.3 Light propagation through a multimode fiber

A light beam incident at the input of the MMF is guided through it only if it is launched at an angle α that allows total internal reflection within the fiber. By applying Snell's law, the maximum acceptance angle is given by Eq. 1.1.

$$\sin(\alpha_{max}) = \frac{(n_1^2 - n_2^2)^{1/2}}{n_0} = \frac{NA}{n_0} \quad (1.1)$$

where $NA = (n_1^2 - n_2^2)^{0.5}$ is a characteristic parameter of an optical fiber known as the numerical aperture and n_1 , n_2 and n_0 are the refractive indices of the core, cladding and the medium in which the fiber exists respectively. Another important parameter of a fiber whose core radius is r_0 is its V-number or the normalized frequency, which is related to the NA by Eq. 1.2.

$$V = \frac{2\pi r_0}{\lambda} NA \quad (1.2)$$

An MMF supports a set of modes determined by its refractive index profile. The mode field solutions for a given MMF can be obtained by solving the wave equation. In the following subsections, we present the derivation of mode fields for a step-index and graded index MMF along with expressions for their propagation constants and number of supported modes.

1.3.1 Helmholtz equation

An electric field, $E = E(r, \phi, z)$ sent towards an MMF obeys the Helmholtz equation, $\Delta^2 E + n^2(r)k_0^2 E = 0$, assuming a homogeneous medium with a constant refractive index, $n(r) = n_1$. When the refractive index has a radial dependence, the Helmholtz equation is still approximately valid using a piece-wise constant model, assuming that the index varies much slower than a wavelength. In the above equation, Δ denotes the Laplacian operator in cylindrical coordinates, $k_0 = 2\pi/\lambda_0$,

λ_0 is the wavelength of the incident field. The Helmholtz equation, with the Laplacian operator expanded, is given by Eq. 1.3.

$$\frac{\partial^2 E}{\partial r^2} + \frac{1}{r} \frac{\partial E}{\partial r} + \frac{1}{r^2} \frac{\partial^2 E}{\partial \phi^2} + \frac{\partial^2 E}{\partial z^2} + n^2 k_0^2 E = 0 \quad (1.3)$$

If we assume that the guided modes are travelling in the z -direction with a propagation constant, β and are periodic in the angle ϕ with a period 2π , then $E = E(r, \phi, z) = u(r)e^{-jl\phi}e^{-j\beta z}$, where $u(r)$ is the radial field function and l corresponds to the azimuthal mode number and takes integer values. Substituting this form in Eq. 1.3, we get Eq. 1.4:

$$\frac{d^2 u}{dr^2} + \frac{1}{r} \frac{du}{dr} + (n^2(r)k_0^2 - \beta^2 - \frac{l^2}{r^2})u = 0 \quad (1.4)$$

1.3.2 Step-index fibers

Let us consider a step-index fiber with a constant core refractive index, n_1 and a cladding refractive index, n_2 . Let the core diameter be r_0 . A wave is guided through the fiber if its propagation constant obeys $n_2 k_0 < \beta < n_1 k_0$. We define k_T and γ in Eq. 1.5 and 1.6:

$$k_T^2 = n_1^2 k_0^2 - \beta^2 \quad (1.5)$$

$$\gamma^2 = \beta^2 - n_2^2 k_0^2 \quad (1.6)$$

Hence, for guided waves, k_T and γ are real. We can then rewrite Eq. 1.4 for the core and the cladding separately as shown in Eq. 1.7 and 1.8.

$$\frac{d^2 u}{dr^2} + \frac{1}{r} \frac{du}{dr} + (k_T^2 - \frac{l^2}{r^2})u = 0, \quad r < r_0 \text{ (core)} \quad (1.7)$$

$$\frac{d^2 u}{dr^2} + \frac{1}{r} \frac{du}{dr} - (\gamma^2 + \frac{l^2}{r^2})u = 0, \quad r > r_0 \text{ (cladding)} \quad (1.8)$$

The solution to the above two differential equations are the family of Bessel functions. Excluding the functions approaching ∞ at $r = 0$ and $r = \infty$, the bounded solutions are given by Eqs. 1.9

and 1.10, where $J_l(x)$ is the l^{th} order Bessel function of the first kind and $K_l(x)$ is the modified l^{th} order Bessel function of the second kind.

$$u(r) \propto J_l(k_T r), \quad r < r_0 \text{ (core)} \quad (1.9)$$

$$u(r) \propto K_l(\gamma r), \quad r > r_0 \text{ (cladding)} \quad (1.10)$$

Most fibers are designed to be weakly guiding i.e., $n_1 \approx n_2$. Under this condition, the guided rays are paraxial and the longitudinal field components are much weaker than the transverse field components, making the guided waves approximately transverse electromagnetic (TEM) in nature. The linear polarization in the x and y directions then form orthogonal polarization states. The linearly polarized (l,m) modes, denoted as LP_{lm} have the same propagation constants and spatial distribution. The weakly guiding approximation or the LP approximation hence allows us to fully describe the mode field solutions using Eqs. 1.9 and 1.10.

To determine the propagation constants of the guided modes, we match the tangential components of the fields in Eqs. 1.9 and 1.10 at the core/cladding interface to obtain the condition in Eq. 1.11.

$$\frac{(k_T r_0) J_l'(k_T r_0)}{J_l(k_T r_0)} = \frac{(\gamma r_0) K_l'(\gamma r_0)}{K_l(\gamma r_0)} \quad (1.11)$$

By simplifying the above expression using Bessel function identities for the derivatives, J_l' and K_l' , and defining, $X = k_T r_0$ and $Y = \gamma r_0$ we obtain the characteristic equation, Eq. 1.12.

$$\frac{X J_{l\pm 1}(X)}{J_l(X)} = \frac{Y K_{l\pm 1}(Y)}{K_l(Y)} \quad (1.12)$$

Recalling the definition for the V-number of the fiber, $V = (NA)k_0 r_0$, we observe that $V^2 = X^2 + Y^2$. Hence given V and l, the above equation can be written in terms of a single unknown, X, with $Y^2 = V^2 - X^2$. The solutions for this equation can be obtained graphically by plotting the left and right hand sides of the equality and finding the points of intersections of the two curves.

For large V-number fibers, an approximate expression for the propagation constants is given by Eq. 1.13.

$$\beta_{lm} = n_1 k_0 \left[1 - \frac{(l + 2m)^2}{M} \Delta \right] \quad (1.13)$$

where M is the number of propagating modes, given by $4/\pi^2 V^2$ for large V-number fibers and $\Delta = (n_1^2 - n_2^2)/(2n_1^2) \approx (n_1 - n_2)/n_1$.

1.3.3 Graded-index fibers

For a Graded-index fiber with a continuously varying refractive index in the core, the Helmholtz equation in Eq. 1.3 is approximately obeyed, subject to the substitutions, $k = n(r)k_0$ and $n^2(r) = \epsilon(r)/\epsilon_0$, when the index, $n(r)$ varies slowly within a wavelength. Consider a power-law refractive index profile, $n(r)$ given by Eq. 1.14.

$$n(r) = n_1 \left[1 - 2\Delta \left(\frac{r}{a} \right)^\alpha \right]^{1/2}, \quad \left(\frac{r}{a} \right) \leq 1 \quad (1.14)$$

where, α is the profile parameter that determines the steepness of the profile. For the special case of a parabolic index profile, with $\alpha = 2$ in Eq. 1.14, solution to the Helmholtz equation has the form of Laguerre-Gauss modes [18] as shown in Eq. 1.15.

$$E_{l,m}(\rho, \phi, z) = \rho^l e^{-\rho^2/2} L_{m-1}^l(\rho^2) \sin(l\phi + \theta_0) e^{-j\beta z} \quad (1.15)$$

where, the radial variable is given as $\rho = r/a\sqrt{V}$ and the generalized Laguerre polynomial is defined in Eq. 1.16.

$$L_{m-1}^l(\rho^2) = \sum_{s=0}^{m-1} \frac{(m-1+l)!(-1)^s \rho^{2s}}{(l+s)!(m-1-s)!s!} \quad (1.16)$$

where $\theta_0 = 0$ or $\pi/2$ represents the pairs of degenerate modes when l is non-zero.

Using the WKB approximation [75], the propagation constant of a mode in a GRIN MMF is given by Eq. 1.17 [76].

$$\beta = k_0 n_1 \left[1 - 2\Delta \left(\frac{P}{P} \right)^{2\alpha/(2+\alpha)} \right]^{1/2} \quad (1.17)$$

where, p is the principle mode number defined as, $x = 2m + l - 1$ and P is the maximum principle mode number, given by Eq. 1.18.

$$P = \sqrt{\frac{\alpha}{\alpha + 2}} k_0 n_1 r_0 \sqrt{\Delta} \quad (1.18)$$

The total number of modes in a GRIN MMF is given by $M = \frac{\alpha}{\alpha + 2} V^2 / 2$, which is $V^2 / 4$ for a GRIN MMF with a parabolic index profile. Fig. 1.3 shows two example LG modes with $(m=1, l=4)$ and $(m=3, l=4)$ respectively.

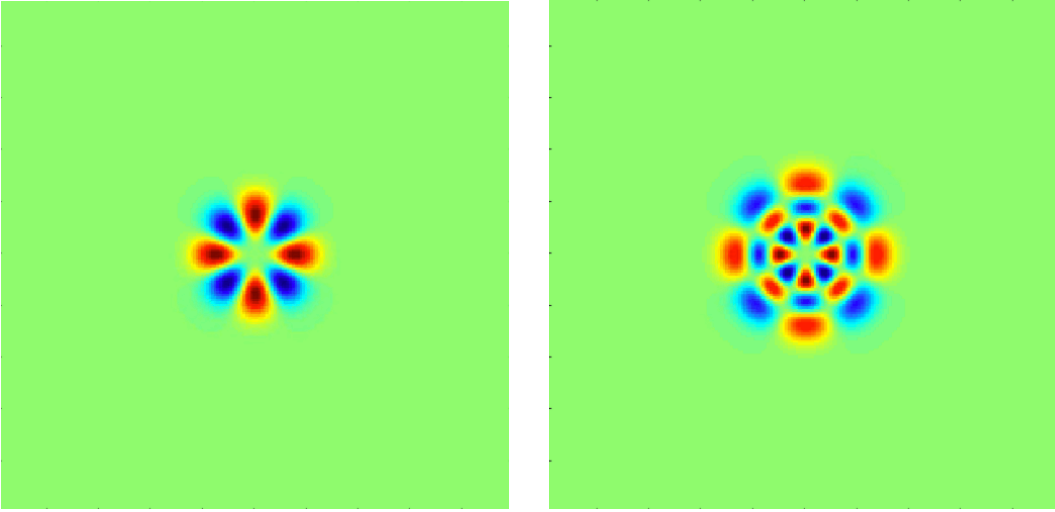


Figure 1.3: Example Laguerre-Gauss mode field solutions for a GRIN fiber with a parabolic index profile with $(m=1, l=4)$ and $(m=3, l=4)$ respectively.

1.3.4 Dispersion in MMFs

A short pulse travelling through an MMF experiences a number of dispersion effects that spread it into a wider time interval. We discuss different sources of dispersion in optical fibers below.

Modal dispersion occurs in MMFs due to the difference in group velocities of the different modes of the fiber. The differential delay between modes increases as a function of the length of the fiber. For a fiber of length L and minimum and maximum group velocities of v_{min} and v_{max} respectively, the spread in the received pulse is given by $L/v_{min} - L/v_{max}$. However, since all the

modes are not excited equally, the overall pulse duration estimated for a triangular envelope is $\sigma_\tau = 1/2(L/v_{min} - L/v_{max})$. For a step-index fiber, $v_{min} = c_1(1 - \Delta)$ and $v_{max} = c_1$, leading to a delay time of $\sigma_\tau = L\Delta/(2c_1)$. On the other hand, a GRIN MMF has a much smaller modal dispersion since its group velocities are equalized by the gradually varying refractive index profile. A GRIN MMF with a parabolic index profile is found to be optimal for minimizing dispersion, with $v_{min} = c_1(1 - \Delta^2/2)$ and $v_{max} = c_1$. The delay time for a parabolic profile GRIN fiber is hence a factor of $\Delta/2$ smaller, i.e., $\sigma_\tau = L\Delta^2/(4c_1)$. Although the pulse broadening due to modal dispersion is proportional to the fiber length, inter-modal coupling, which comes into play beyond a certain critical length, alters this dependence. Inter-modal coupling leads to exchange of optical power between modes that have similar propagation constants as a result of imperfections in the fiber, random surface irregularities and refractive index inhomogeneities.

Material dispersion is another type of dispersion, which occurs due to the wavelength dependence of the refractive index of the glass used in fabricating the optical fiber. Material dispersion is also proportional to the fiber length. Even when material dispersion is negligible, the group velocities of the different modes have a wavelength dependence, leading to another type of dispersion namely, **waveguide dispersion**. The combined effect of material and waveguide dispersion is also known as chromatic dispersion.

Another source of pulse broadening is **polarization mode dispersion**(PMD). This effect arises due to small random variations in the birefringence of the fiber along its length, caused by slight refractive index variations and ellipticity of the fiber cross-section. While the effects of these inhomogeneities is difficult to assess, a statistical model used to consider them predicts that the RMS value of the pulse broadening due to PMD is proportional to the square root of the fiber length.

Finally, **nonlinear dispersion** is a yet another source of dispersion of high-intensity beams travelling through the fiber core. After a certain intensity level is reached, the refractive index becomes intensity dependent. Since the phase is proportional to the refractive index, the high-intensity portions of the beam undergo a phase shift with respect to the low-intensity portions, an

effect called self-phase modulation. This effect gives rise to instantaneous frequencies shifted by different amounts, hence contributing to pulse dispersion.

The combination of the above effects in a given MMF leads to a random interference pattern at the output end, known as a speckle pattern, which distorts all spatial information. Although the spatial information is distorted, it can still be recovered by characterizing the input-output relationship of the MMF using its transmission matrix (TM). In principle, this relationship should be theoretically derivable by solving the wave equation for the Eigen modes of the fiber, using the fiber's precise index distribution and including all the dispersion effects. However in practice, the exact geometrical and refractive index parameters are difficult to precisely control during fabrication and the fiber is prone to inherent defects and asymmetries as well as environmental perturbations and temperature variations that modify its properties, making it impractical to predict its TM. Therefore, we measure the TM of an MMF experimentally. The following section describes how this is achieved.

1.4 MMF Imaging using the transmission matrix method

Imaging through MMFs can be accomplished by experimentally measuring the fiber's TM [145]. Once the TM is known, it can be used to predict the input illumination required to generate a controlled output illumination. By scanning a set of orthogonal illuminations over the object, its reconstruction can be obtained. The entire process can be described in two steps: calibration and scanning as detailed below and illustrated in figure 1.4.

1.4.1 Calibration

The purpose of calibration is to measure the TM of the MMF, which provides information about the expected output field for an arbitrary input field launched into the fiber. A vectorized output field E_{out}^m appearing on the distal side of the fiber, where m is the output mode index, can be described as a weighted sum over all the input modes, E_{in} launched into the fiber, each with a

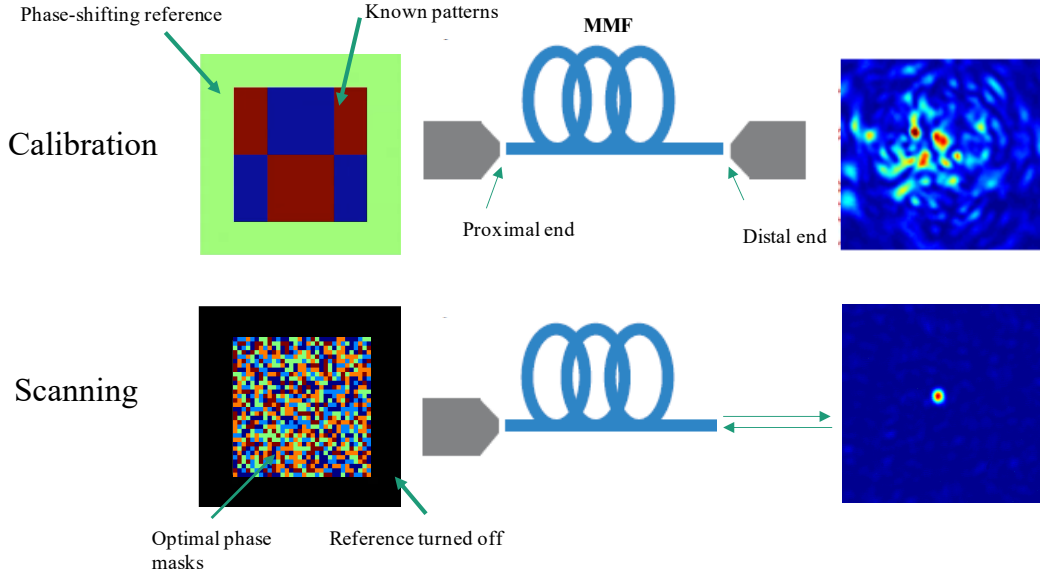


Figure 1.4: Illustration of imaging through MMFs using the TM method. Top and bottom schematics describe the calibration and scanning processes respectively.

weight t_{mn} corresponding to the m^{th} output mode and n^{th} input mode, as described in Eq. 1.19.

$$E_{out}^m = \sum_{n=1}^N t_{mn} E_{in}^n \quad (1.19)$$

The set of TM coefficients for all N number of input modes and M number of output modes generates the full TM.

In order to measure these weights experimentally with both phase and amplitude information, we send a complete basis set of orthogonal input fields into the fiber accompanied with a phase-stepping reference field. . In most cases these fields are constant in amplitude with their phase dynamically modulated. If using an amplitude spatial light modulator such as the DMD, phase modulation is achieved by projecting computer-generated amplitude holograms [31]. The DMD's active area is divided into two sections, one (typically centered) for the basis-function changing pattern and another for the phase-stepping reference, typically surrounding the first one.

The intensity measurements of the fiber output for each projected pattern, as the reference field is phase stepped three times, enables recovery of the output field using phase-shifting inter-

ferometry [32] as described in eq 1.20.

$$t_{*n} = \frac{I_n^0 - I_n^\pi}{4} - i \frac{I_n^0 - 2I_n^{\pi/2} + I_n^\pi}{4} \quad (1.20)$$

Here I_n^i denote the output mode intensities for the n^{th} input mode and their superscripts denote the phase step of the reference field. Repeating the above output field measurements for N input modes gives us the observed TM, which we denote as K_{obs} . K_{obs} is only an estimate of the fiber TM, since the reference field employed for calibration propagates through the fiber and transforms into a speckle pattern instead of an ideal plane wave reference typically employed for interferometry.

1.4.2 Scanning

Once the TM of the MMF is measured, we can use it to predict the input field, E_{in} required to generate any desired out field, E_{target} using Eq. 1.21.

$$E_{in} = K_{obs}^\dagger E^{target} \quad (1.21)$$

A common choice of scanning illumination is the canonical basis of focal spots. To recover an N -pixel object, N focal spots are created through the fiber and projected on the object. The object then reflects back a signal proportional to their overlap back into the fiber which can be detected using a bucket detector. This signal put together provides the desired image of the object.

Over the decade, this technique has been widely adopted for MMF imaging. However it is not the only one in existence and neither the first one. The following section delves into a brief history of the origin of MMF imaging.

1.5 Multimode fiber imaging timeline

The idea of using MMFs for imaging was not born recently. The first attempt to retrieve images through MMFs was made by Spitz et al. [169] more than 50 years ago where the hologram of an object placed in front of the fiber, was recorded using a photographic plate on its distal

side. The hologram was then read out with a counter-propagating beam to reconstruct the object in its initial position. Although this was interesting, it did not allow controlling the light coming out on the distal side of the fiber, which is where the object of interest is located in endoscopic applications. Many other papers came out following this work centered around the idea of optical phase conjugation [80, 189, 72, 69]. However, at the time, photo-refractive crystals were the only available option to dynamically perform phase conjugation and they were slow and inefficient. Imaging with MMFs was hence not feasible yet. This scenario changed with the advances in the wavefront shaping technology that made devices like spatial light modulators (SLMs) and digital micromirror devices (DMDs) available, to modulate the wavefront of light almost in real-time.

Four decades after Spitz's work on phase conjugation, Vellekoop et al. [182] demonstrated wavefront shaping to create a focal spot behind a scattering medium using an iterative algorithm. This work kick started the field of wavefront shaping for imaging through turbid media. Soon after that, Popoff et al. [145] showed that one can measure the TM of a scattering medium by projecting known orthogonal patterns on it and measuring the output response for each such pattern on the distal side. Using the TM, one can then predict the input wavefront to create a desired complex pattern on the other side, as explained in the previous section. Both these papers were not directly linked to MMF imaging, but they set the foundation for the future work in the field.

Beginning around 2011, the first publications employing liquid-crystal spatial light modulators for controlling the distal fields through MMFs came out [52, 138, 41, 139, 30]. Much of this work either employed the TM measurement approach by Popoff or digital phase conjugation to produce focal points on the distal end and scan them laterally to recover the object. Other approaches included a technique called turbid lens imaging that allowed widefield imaging by averaging over many speckle projections [40] or non-local sampling and optimization based reconstruction of the object [123]. Yet another interesting approach employed spatio-spectral encoding for a bend or motion-insensitive approach to perform incoherent imaging [12]. Most of these used SLMs for phase modulation of the input wavefront which could update at upto 100 Hz and served as the bottleneck in imaging speed. Caravaca et al. [30] showed that DMDs, which are binary amplitude

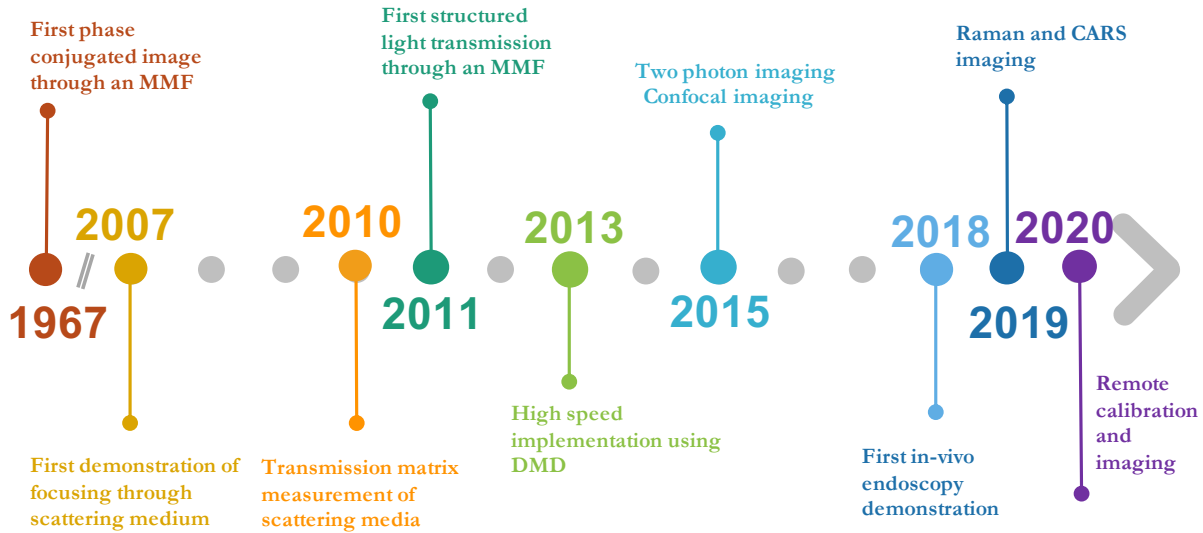


Figure 1.5: Schematic timeline of multimode fiber imaging

modulators and operate at a refresh rate of 22 kHz could be used for phase modulation by combining pixels, projecting gratings on the macro-pixels and shifting them. Their fast switching speed allowed an order of magnitude improvement in imaging speed, thereby making real-time MMF imaging more feasible.

Other important milestones in the progress of MMF imaging include two photon imaging [126, 166], confocal MMF imaging [118, 117], first in-vivo imaging in a live mouse [133] and just recently, Raman and CARS imaging [50, 175]. With such significant developments, all within the last decade, the prospects for MMF endoscopy are encouraging and suggest that their progress towards feasibility in clinical applications.

1.6 Current challenges and benchmarks

Although excellent imaging capabilities have been demonstrated with MMFs, there are still a few significant challenges that remain to be addressed. In this section, we identify three of the major challenges and present some of the existing work and current benchmarks related to them that will allow us to gauge the path to in-vivo imaging.

1.6.1 Speed

In in-vivo imaging, speed is an important consideration as speckle decorrelations occur due to scattering of light from blood at the millisecond timescale besides other slower decorrelation phenomena due to breathing and motion[111]. In the context of functional brain imaging as well, neural activity can change at a rate as fast as a few milliseconds [158]. A practically feasible endoscope therefore needs to be able to acquire an image ideally faster but at least at the same timescale. The bottleneck for speed in MMF imaging is limited by the refresh rate of the wavefront shaper. Caravaca et al. set the benchmark for wavefront shaping speed to 22 kHz by demonstrating the use of DMDs for phase modulation [30]. Since imaging with MMFs is done using a scanning approach, it follows that to image a 100×100 pixel object, it would need 10000 measurements leading to an imaging frame rate of 2.2 frames/sec. There is considerable room for improvement here. Besides the wavefront refresh rate, the imaging frame rate can also be improved if the number of measurements needed to generate a given size of image could be reduced. One approach to enable this is to perform a random access to probe predefined points at a faster rate instead of using the sequential raster scan approach currently used.

1.6.2 Robustness

Another important challenge as mentioned before, is the sensitivity of MMFs to bending. A lot of interesting work has been done along this path over the years. In an initial attempt, the speckle from a straight fiber was restored after it was bent by applying a second compensating bend to the fiber [10]. Caravaca et al. proposed a real-time bend correction [30] by continuously measuring the fiber TM very quickly using a DMD for fast wavefront update. However, it requires access to the distal side for correction.

Another approach proposed by Farahi et al. [58] is to use a virtual coherent light source that allows the reflected speckle from the MMF to act as a signature for different bend configurations. By calibrating for all possible configurations, the reflected speckle allows identifying and applying

the appropriate correction to restore the original foci on the distal end. While it is interesting, the method works only for a finite number of bend configurations that have been calibrated for. Also if there are too many configurations, the computation time increases, making a real-time implementation difficult. Ploshner et al. [142] proposed a theoretical model to mimic real fiber TMs and to estimate how they change when their geometrical configuration is known. This is interesting, however knowing the exact bend configuration of the fiber in real-time is often infeasible.

Gu et al. [83] proposed to use a partial reflector at the distal end of the fiber for bend correction feedback. However, it is based on the assumption that the fiber TM is unitary or lossless, which is unrealistic since even precision-fabricated MMFs have an associated non-zero loss [34, 82]. Also the fabrication of the partial reflector can be challenging. The same group later relaxed the unitary constraint and performed bend correction [82] by exploiting correlations between TMs of the fiber before and after bending. However, the correction calculated without knowledge of the distal fields shows only slight improvement and suggests need for better design of the reflector at the distal tip.

Recent preliminary efforts have also been made to overcome the bending problem by replacing the distal calibration with a proximal calibration. Theoretical studies have demonstrated that with the help of a reflection feedback mechanism, we can measure three unique realizations of the double pass TM and use it to solve for the single-pass TM [78]. A design of a metasurface reflector stack to measure the double-pass TM for three unique wavelengths has been proposed [78], however its practical implementation needs significant work towards design and fabrication of reflector stacks and their installation at the distal end of the fiber while keeping it ultrathin. Another approach uses a guide star at the distal end and exploits the quasi-radial memory effect in MMFs [110] to measure the approximate TM from the proximal end. While this is promising work, it allows only partial images to be retrieved, limited by the spatial extent of the guide star.

There have also been experimental studies to identify robust types of fibers and more resilient bend configurations. Loterie et al. [119] present a study of different bend configurations and identify a specific bend geometry- s-bends - as more robust to bends than others. Caravaca et al. [32] shows

that the refractive index profile of MMFs is also a factor in robustness. Their experiments show that graded index fibers are more robust. Both these papers also establish that there is some intrinsic tolerance to bending and a focus created on the distal end is retained for displacements of a few millimeters of the distal tip or the middle part of the fiber. Although it is hard to predict a hard bound to the motion range within which live animal imaging can be accomplished, it would undoubtedly be useful to extend the bend tolerance of MMFs from a few millimeters to centimeters.

Another factor in robustness comes from the sensitivity and stability requirements of the system as a whole. As described earlier, imaging using the TM method requires interferometric stability for calibration, which might not be feasible in a dynamic environment. Relaxing stability constraints will also make way for more robust endoscopes.

1.6.3 Optical sectioning and resolution

When imaging inside a tissue volume, optical sectioning is very important to eliminate background and improve axial resolution. Depth of field in MMF imaging is limited by the NA of the fiber. A typical NA of MMFs used for imaging is 0.3, which gives a wavelength dependent depth of field of 22.2λ . For a 532 nm laser source, this figure is about $12\ \mu\text{m}$. The diffraction limited resolution in MMF imaging on the other hand is determined by the numerical aperture of the MMF, which is $0.89\ \mu\text{m}$ for a fiber with NA 0.3 and a laser wavelength of 532 nm. Since a zero working distance is impractical and the effective NA decreases with increasing working distance, the practical resolution limit is close to a micrometer. Sub-micron scale imaging can be useful to explore, for instance, fine dendritic structure, actin filaments etc.

Several techniques have been demonstrated to achieve both better sectioning and resolution. Two photon imaging [166, 126] was shown to provide excellent intrinsic optical sectioning, however it needs time gating and dispersion pre-compensation optics design to account for the temporal dispersion of ultrashort pulses. Confocal imaging [118, 117] uses a virtual or physical pinhole to improve sectioning and resolution, however, it suffers from the problem of low signal to noise ratio (SNR) and difficulty in translation to fluorescence imaging since most of the light is rejected.

Saturated excitation [106], which uses the nonlinear fluorescence from saturated fluorophores to provide both better sectioning and resolution has also been demonstrated as an effective solution however, it requires very high peak power levels that are infeasible for use with biological tissue.

Resolution enhancement has also been shown by use of a multiple scatterer before the fiber [39, 140, 21] however it comes at the cost of transmission loss of light. Another interesting approach used a parabolic tip design [21] to increase the effective NA of the fiber to up to 1. However the design requires a non-zero working distance, which makes the endoscope more susceptible to tissue induced light distortions due to index mismatch. Recently, resolution beyond the diffraction limit [6] has also been demonstrated using MMFs by assuming sparsity in samples. This work is similar to our work presented in chapter 2 [33]. However, it uses extremely sparse point objects with limited fields of view and requires SNR levels of the sample higher than those feasible with bio-compatible markers. Although a host of effective methods exist to achieve sectioning and resolution, a reliable and robust method that could work while maintaining reasonable SNR levels is desirable.

1.7 Thesis overview

The goal of this Thesis is to deal with the challenges in MMF imaging described in the previous section- speed, robustness, optical sectioning, SNR and resolution. In chapter 2, we present a technique that simplifies MMF imaging by employing speckle patterns for scanning the object. Using the naturally occurring output of the MMF for imaging allows simplifying the calibration and eliminating the need for coherent control over the output field. Furthermore, the method requires intensity-only measurements and fewer number of illuminations than one would need for focal spot scanning, hence leading to improved imaging speed and robustness. We further present a method to optimize the compressibility of our measurements by eliminating redundancies in our sampling illuminations. Our algorithm minimizes the correlations in the speckle patterns used for imaging, hence improving sampling efficiency and allowing higher compression. Furthermore, the technique relies on assuming sparsity of the sample which also enables some degree of optical sectioning and resolution improvement.

In chapter 3, we present an approach to further push the speed of MMF imaging by more than an order of magnitude by employing a one-dimensional wavefront modulator called a grating light valve (GLV) that has a refresh rate of 350 kHz. The speckle produced after the scatterer that is subject to one-dimensional wavefront modulation shows some interesting features, especially when the scatterer exhibits a phenomenon known as the memory effect [95]. We present an analysis on the dependence of the speckle shape on the amount of memory effect of a scatterer and propose the optimal configurations for imaging through them. We also show focusing through an MMF using the GLV at a record speed of 2 ms, as well as focusing through a dynamically changing scattering medium. We make the case that the single dimension control does not limit our capability to manipulate the output through the scattering media as long as enough degrees of freedom are available.

In chapter 4 we diverge from imaging and present a technique to tailor the fiber mode composition at the output of an MMF with thousands of modes, which we refer to as myriad-mode fiber (MyF). While precise mode control has been demonstrated in relatively few-mode fibers, the method proposed here is scalable, enables generation of complex mode combinations and is particularly useful for MyFs, such as when the number of modes is comparable to the number of modes of the wavefront shaping spatial light modulator. MyFs are attractive for imaging due to their higher NA and bigger field of view. By selecting only a subset of fiber modes to create focal spots at the output as an example, we demonstrate the ability to combine the advantages of MyFs for imaging with the advantages of few-mode fibers for bend resilience and robustness.

Chapter 5 addresses the challenge of optical sectioning and resolution in multimode fiber imaging for imaging through 3-D samples. Towards this end, we generalize the principle of image scanning microscopy [130] and adapt it to imaging through complex media like MMFs. We also describe an imaging methodology where the excitation and detection pathways could be different, as is common in various endoscopy applications. We demonstrate high signal-to-noise ratio imaging with good optical sectioning and improved resolution compared to the single pixel imaging approach used in the earlier work. We also present a scheme to generalize the method to arbitrary output

illumination such as speckle patterns.

Finally in chapter 6, we discuss the future directions to advance the work presented in this Thesis and conclude with a summary of its contributions. Fig. 1.6 shows a schematic mapping of the contribution of each chapter to the different goals of this Thesis namely, speed, robustness, and resolution, SNR and optical sectioning.

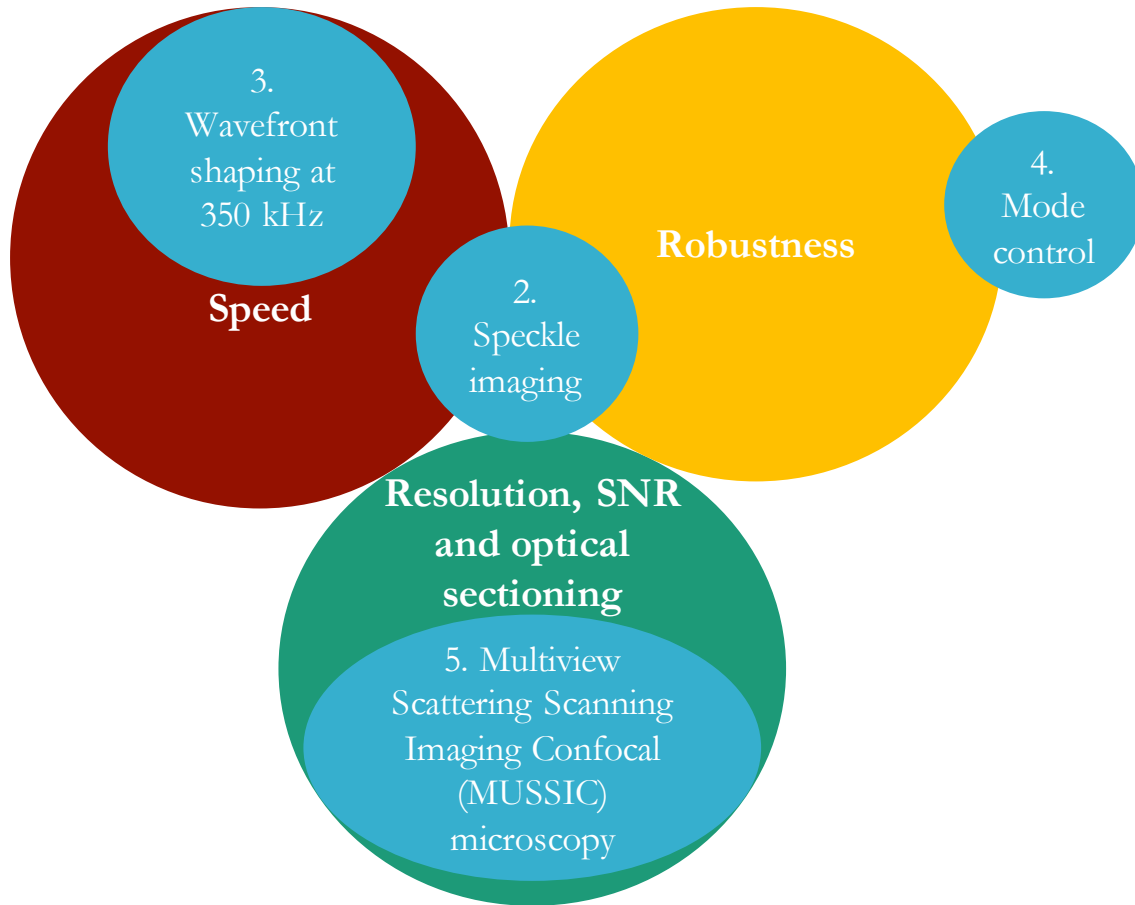


Figure 1.6: Thesis Overview

Chapter 2

Speckle imaging through multimode fibers

2.1 Introduction

Coherent light propagating through an MMF is randomized through it leading to a speckle pattern at its distal end. Current methods for imaging through an MMF requires control over the distal illumination of the MMF, which is achieved either by (1) measuring the MMF's TM, (2) using an optimization procedure [52, 122], or (3) by training a neural network [150, 148]. The TM calibration is an interferometric procedure that is sensitive to environmental perturbations. Moreover, since the quantities being measured are fields, at least three intensity measurements are required for measuring each speckle field. An alternate method for TM measurement using only intensity measurements involves using phase retrieval algorithms [132, 53], however they usually require careful tuning of multiple parameters and their convergence is often not guaranteed. The optimization approach on the other hand is time consuming while the neural network approach also requires hours of training over large data-sets before it can learn the TM.

In this chapter, we present a method for simplifying the TM calibration process by eliminating the need for controlling the distal illumination and by employing the natural output of the MMFs-speckle patterns as the sampling illuminations. Our method uses only intensity measurements and all the computation required for image recovery can be done offline, unlike in the case of TM recovery using phase retrieval algorithms, where computation is required before imaging can be performed.

The idea of using speckle patterns for scanning the object for imaging with MMFs is in fact

not a recent discovery. It was first proposed by Bolshtyansky et al. [23] who simulated the total integrated signal coming from a reflective object illuminated with speckles produced by an MMF and demonstrated coherent imaging. The concept was later demonstrated experimentally through an MMF first with reflective samples [123]. Although this approach still requires a calibration step, it is simpler because it only requires to measure the optical speckle intensities as opposed to wavefront shaping based methods that require speckle field measurements.

Interestingly, besides the advantage that speckles are readily produced by propagation through MMF, they have also been shown to have ideal properties for reducing or compressing the number of measurements needed to fully characterize the object due to their ability to perform non-local sampling [180, 184, 4]. This means that as opposed to scanning focal spots, the most common choice of distal illuminations for imaging through MMFs, which typically need scanning of N number of focal spots, speckle patterns require a smaller number, $M < N$ measurements to obtain an N pixel image of an object.

This compression is achieved with the help of some prior knowledge about the object such as its sparsity, where sparse matrices refer to matrices whose most elements are zero-values. This technique of applying object sparsity information to solve for it is known as compressive sensing [29].

Although speckle imaging has been demonstrated before, the advantage of speckles for compressive sampling had remained unexploited. In our work reported in [104], we demonstrate compressive imaging through MMFs for the first time, which allows reducing the number of measurements. Our work is also the first fluorescence imaging demonstration using speckles. Soon after, Amitonova et. al. [5] also demonstrated a similar method using well-separated binary objects made of fluorescent beads.

Our work demonstrates that the technique can be scaled up using a bigger fiber with more modes and larger and more densely populated fields of view. Moreover, in our further work reported in [33], we also demonstrate that the technique works well with relatively thicker objects which introduce background light to the scene of interest. We show that we are able to eliminate this

background effectively with the help of the sparsity assumption to obtain a clean image of the object. Furthermore, we present an algorithm to optimize the set of speckle pattern used for reconstruction so as to recover the object with the least number of sampling efficient speckle patterns.

Finally, we show that the above concept can also be extended to implement both photoacoustic and fluorescence endoscopic imaging through a small cross section MMF. Combining the pre-recorded speckle patterns and the corresponding fluorescence and photoacoustic signals from the object at the distal tip of the MMF with reconstruction algorithms, we obtain images of biological test samples in vitro with both modalities with a minimally invasive microendoscope.

2.2 Methods

Speckle imaging through an MMF can be performed in two steps- calibration and scanning similar to the TM method, followed by a third offline step to process the acquired data for object reconstruction. All of these steps are detailed below.

2.2.1 Calibration

The purpose of the calibration process in speckle imaging is to acquire knowledge of all the distal speckle pattern intensity distributions. The set of speckles used in imaging should ideally form a complete basis to ensure that every point in the field of view is being sensed by at least one speckle pattern and that there are no holes or unprobed regions. Furthermore, each speckle pattern should ideally be unique and sample the object differently so as to avoid redundancy in measurements. In order to ensure such speckle patterns are being produced by the MMF, the input illuminations sent through the MMF must consist of uncorrelated patterns. We choose the binary Gaussian random basis for input illuminations. As the random patterns are projected onto the near side or proximal facet of the fiber, the speckle patterns emerging on the distal side are recorded. Unlike the TM method, we do not need phase information here, so all measurements are intensity-only and single shot. A complete basis of speckle patterns forms the incoherent TM of the fiber, which we will denote as A .

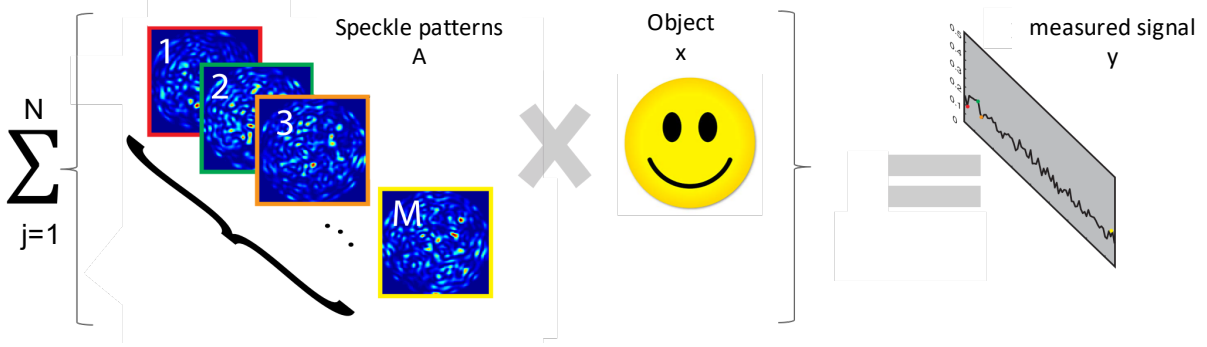


Figure 2.1: Principle of speckle illumination imaging through a MMF: A set of M pre-calibrated speckle intensity patterns sample the object plane to generate M corresponding signals y_i proportional to the overlap between each speckle A_i and the object, x . The total integrated signal is detected using a single pixel detector.

2.2.2 Scanning

After calibration, the camera and accompanying optics after the fiber are removed and the sample object is brought to the distal end. Each speckle pattern produced during calibration is then reproduced and projected onto the object which in response, produces a return signal proportional to the amount of overlap between itself and the projected speckle pattern. This signal, which could be fluorescence or a photoacoustic signal or both, then recouples into the fiber and is detected on the proximal side using a bucket detector.

This detected signal, which we denote by y_i , where i is the index of the speckle pattern is mathematically given by the overlap integral of the object and the i^{th} speckle pattern given by Eq. 2.1

$$y_i = \iint_{\text{area}} A_i(u, v)x(u, v)dudv \quad (2.1)$$

The intensity fluctuations from speckle pattern to speckle pattern in the object plane translates into fluctuations of the signal A_i , thereby encoding sample information at the positions at which the speckle grains overlap with the object, reminiscent of the working principle of a single pixel camera [54]. Figure 2.1 illustrates the principle of imaging with speckle illumination.

2.2.3 Reconstruction algorithm

Given the matrix A containing the recorded speckle patterns in its rows and vector y containing the measured return signal from the sample, the entire imaging system can be represented in matrix form by eq 2.2.

$$y = Ax \tag{2.2}$$

A conventional choice for the A matrix is the canonical basis where the object is scanned point-by-point. The matrix A is then an identity matrix, which means that y is a direct mapping of x . Focal point scanning however requires a coherent TM calibration as described in the TM method. Alternately, when A consists of random speckle patterns, solving for x requires inversion of the matrix A . Unfortunately, A is often a large, rectangular and badly conditioned matrix and its inverse does not exist. Nevertheless, there are still various ways of finding an estimate of x . We choose to combine and employ the techniques detailed below for our reconstruction.

- (1) Correlation or ghost imaging: Correlation imaging [4, 143, 98] relies on the fact that every return signal y_i is a measure of the overlap between the i_{th} speckle pattern and the object and therefore is similar to the weight of the speckle pattern contributing to the object. Hence, every j^{th} pixel of the object is computed as the correlation of the j^{th} pixel of all the speckle patterns with return signals y as shown in Eq. 2.3.

$$x_j = \frac{E[\tilde{A}_j \tilde{y}]}{\sigma_A \sigma_y} \tag{2.3}$$

- (2) Regularized least square: Solving for x by minimizing the least square difference of the left and right hand side of Eq. 2.2 is an effective method to solve inverse problems with the simple solution $A^{-1}b$ when the matrix A is non-singular. However when A is non-invertible and poorly conditioned, the closest estimate to its inverse can be noisy and leads to meaningless solutions with huge norms. Regularizing the problem by adding the euclidean norm of the object to the cost function helps reduce noise and improve the estimate for x . This is also known as Tikhonov regularization and a free parameter, β is

used to determine the amount of regularization or weight of the object’s euclidean norm in the cost function.

- (3) Least square optimization with priors: When we have some prior information about the object of interest such as sparsity, it can be used to improve the estimate of the object and enable recovery with fewer number of measurements. Depending on the type of object that we are interested in, different priors such as sparsity in the spatial domain [84] or the spatial gradient domain [164] are suitable. An advantage of using a sparsity prior is its robustness to outliers. Since we are interested in enabling imaging of neural activity which is sparse in the spatial domain or objects representative of them such as fluorescent beads, we employ the spatial sparsity constraint to solve for the object.

Sparsity can be enforced in our solution by adding an l_1 norm in the cost function [29]. We introduce a free parameter, α to tune the weight of this term in the cost function. We also know that the fluorescence signal being detected is positive and hence impose a positivity constraint on the object.

On combining the priors described in (2) and (3), we solve for the object using a sparsity and positivity constrained and Tikhonov regularized least square optimization problem given by Eq. 2.4.

$$\min_x \|\mathbf{Ax} - \mathbf{y}\|_2^2 + \alpha \|\mathbf{x}\|_1 + \beta \|\mathbf{x}\|_2 \quad s.t. x \geq 0 \quad (2.4)$$

We use a fast converging algorithm called fast iterative shrinkage algorithm (FISTA) [14], which has a convergence rate of $O(\frac{1}{k^2})$ for solving the above problem. We initialize the algorithm with the correlation image obtained in (1) as a first guess. An optimal solution is reached in a computation time of less than 2 minutes and 50 iterations for a $10,000 \times 40,000$ A matrix. This computation is done offline after all data acquisition.

2.3 Selection of speckle patterns for best compression

As mentioned earlier, the ability to reduce the number of measurements needed for object recovery depends on how sampling efficient and how unique the speckle patterns being used to scan the object are. An ideal set of M speckle patterns would form a complete basis set which can encode information about every point at the fiber distal tip.

At the same time, each speckle pattern must be able to retrieve unique information about the sample in order to eliminate redundancies. The optimal compression ratio N/M is achieved when we have enough speckle patterns to sample the whole field of view and the correlations between speckle patterns is minimized. We quantify these correlations by their mutual coherence, defined as

$$\mu_{ij} = \frac{A_{i,*} \cdot A_{j,*}}{|A_{i,*}| \cdot |A_{j,*}|} \quad (2.5)$$

where μ_{ij} is the mutual coherence between the i^{th} and j^{th} patterns. The $M \times M$ mutual coherence matrix can be constructed containing the correlation of each speckle with every other speckle. Candes et al. presented the lower bound for the number M in terms of the number of pixels in the object, N , the sparsity of the object, S , maximum coherence function μ_{max} and a constant C given by Eq. 2.6.

$$M \leq C \mu_{max} S \log(N) \quad (2.6)$$

For any given object, the only parameter that we can optimize is the mutual coherence of speckle pattern. It turns out that it is infeasible to make the correlation between speckle patterns zero. This is because a fraction of the light reflected from the DMD could be unmodulated. Moreover, the modes of the fiber have naturally overlapping trajectories making it impossible for their intensity correlations to be zero.

We recorded speckle intensities at the distal side of the fiber in experiment and plot their mutual coherence matrix In fig. 2.2. We also plot the same matrix for a simulated Gaussian random intensity matrix. It can be observed here that the mutual coherence matrix for the recorded speckle patterns show some structure due to higher correlations as compared to the former. there

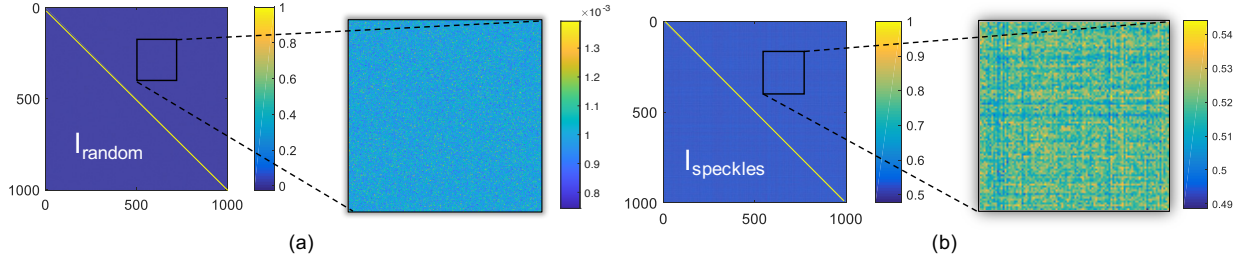


Figure 2.2: Comparison of mutual coherence matrix of 1000 experimentally recorded speckle intensity patterns through the fiber and of simulated Gaussian random intensity patterns in the computer. (a) Coherence matrix of random patterns shown almost no structure and little correlations. (b) The coherence matrix of speckle patterns on the other hand shows line-like structures due to high correlations that have a mean of about 0.5.

is therefore room for improvement.

We present an algorithm below that allows us to pick a smaller optimal set of speckle patterns with reduced correlations from a larger set of speckle patterns. The algorithm involves the following steps:

- (1) Set the speckle self-correlation terms on the diagonal elements of the coherence matrix, to zero. This way only correlations between different speckles are analyzed.
- (2) Calculate the norm of each row in the mutual coherence matrix. The row R_i with maximum norm signifies that the i^{th} speckle pattern has maximum correlations with all other speckle patterns in the set.
- (3) Set the i^{th} row and column in the coherence matrix to zero and note the index, i , of the speckle to be deleted from the set. The new coherence matrix corresponds to correlations among $M-1$ patterns.
- (4) Repeat 2 and 3 till the number of non-zero rows in the coherence matrix becomes equal to the size of the desired optimized set.

Note that the coherence matrix is symmetric, which means the above optimization can equivalently be performed on columns instead of rows of the coherence matrix, leading to the same results. The

last M number of patterns left in the coherence matrix constitute the optimal set of least correlated speckle patterns.

2.4 Resolution limit

Resolution limit in speckle imaging is dictated by the NA of the MMF. The fiber used in our experiments has an NA of 0.29. With a green laser source of wavelength 532 nm, the diffraction limited resolution is $0.92\mu\text{m}$. However, the object is placed a small distance away from the fiber to prevent damage to the fiber tip. By the time the speckle diffracts to the object plane, it has a slightly larger grain size of $1.6\mu\text{m}$, which we calculate by performing the autocorrelation of the recorded speckle pattern. We prove using experimental data in fig. 2.3 that the resolution in the TM method which is dictated by the full-width half maximum of the focal spot matches the resolution in speckle imaging measured by the speckle grain size. In chapter 5, we propose a method to improve the imaging resolution by a factor of 2.

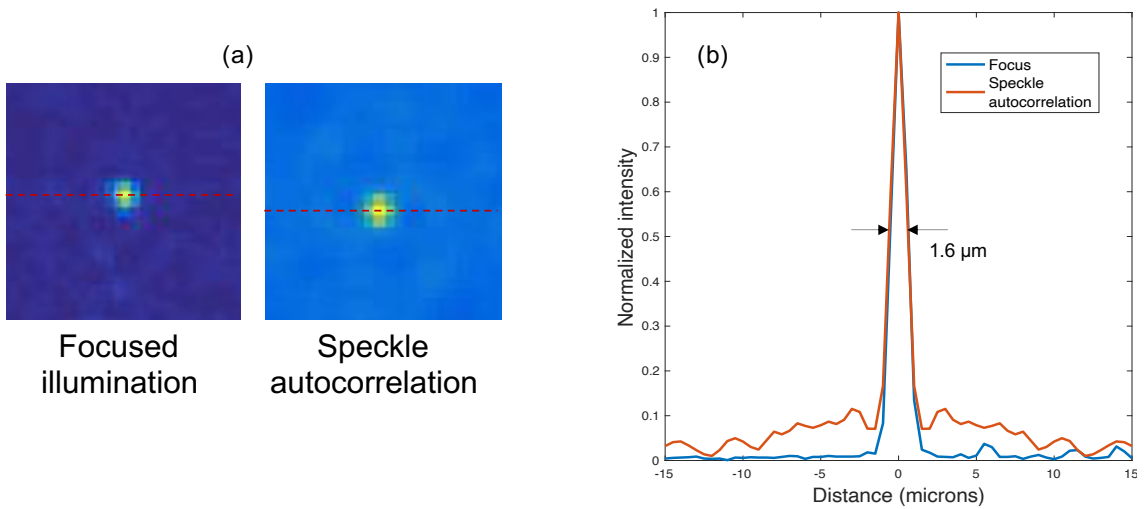


Figure 2.3: Comparison of resolution in the TM method and Speckle imaging. (a) Zoomed in images of a focal spot recorded on a camera during imaging with the TM method and the computed autocorrelation of a speckle pattern recorded during correlation imaging. (b) Overlaid cross-sections and the full width at half maxima extracted at positions indicated by red lines in the two images in (a) show that the resolution in both cases are identical.

2.5 Experimental Setup

A schematic description of the experimental setup used for speckle imaging is shown in figure 2.4. The excitation light is provided by a 532 nm CW Coherent Verdi-G laser which passes through a spatial filter SF and is incident on a DMD (TI-DLP Discovery 4100) which performs wavefront modulation at a refresh rate of 22 KHz. A 30-cm long graded index MMF (Newport F-MLD) with an NA of 0.29 is used for imaging. The outer diameter of the MMF (without protective cladding) is $125 \mu\text{m}$ and accounts for the total footprint of the endoscope. The $100 \mu\text{m}$ -diameter MMF core is used to guide the source light, and also collect fluorescence.

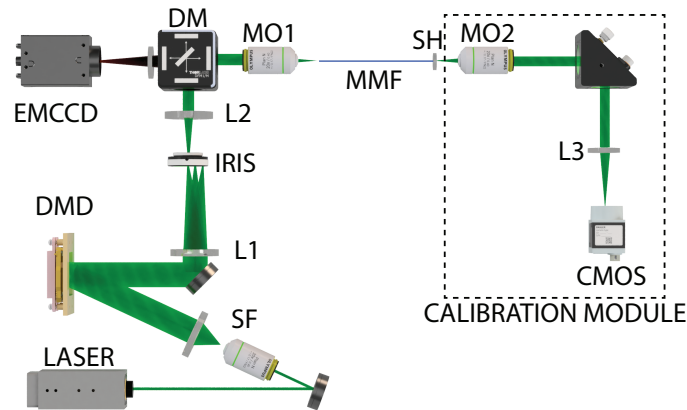


Figure 2.4: Experimental setup for fluorescence imaging using speckle illumination through a multimode fiber.

For the calibration step, a set of 10,000 binary random patterns are projected onto the DMD using a square patch of 96×96 independent macropixels on its active area. Each macropixel is used to project a grating and consists of 8×8 physical pixels of the DMD. The gratings projected on the macropixels can be shifted in the transverse direction to allow phase modulation in the -1^{st} order of the Fourier plane of the DMD [43]. A 4f system is used to image the DMD plane onto the the back focal plane of a a 20x magnification microscope objective MO1. The phase modulated

-1^{st} order is isolated using a pinhole placed in the Fourier plane of this 4f-system. The microscope objective MO1 then couples the Fourier plane of the phase modulated patterns into the fiber.

This light is scrambled through the fiber and a speckle pattern appears on the distal end which is then imaged using a 40x microscope objective MO2 and lens L3 onto a CMOS camera (Hamamatsu Orca Flash 2.8). The plane where the speckle patterns are being imaged is slightly offset from the distal facet of the fiber so that the sample to be imaged placed right after it can be in sharp focus.

After calibration, the calibration module composed of the microscope objective, lens and CMOS camera is removed and replaced with the fluorescent sample mounted on a sample holder SH. The same set of patterns used for calibration are projected on the sample and for each pattern projection, a corresponding fluorescence signal coming back to the proximal end of the fiber is recorded using an Andor iXon+ Electron multiplying gain CCD (EMCCD). The excitation photons are rejected using a dichroic mirror DM (Chroma ZT532rdc-UF1) and a bandpass filter (Chroma ET590/50m).

It should be noted here that the only information we require is the total integrated fluorescence intensity across the whole fiber cross-section. A photomultiplier tube (PMT), which is faster and cheaper can therefore also serve our purpose instead of the EMCCD. We employ the EMCCD in our experiments simply because of its availability in the system and other parallelly ongoing experiments.

Luckily, using the EMCCD and capturing images instead of the total signal allowed a small boost in the SNR in our measurements. The fluorescent light collected at the proximal end of the fiber contained a contribution from the autofluorescence of the fiber, more prominently in the fiber cladding. This undesired signal added noise to our measurements and could be discarded (by operating in the image acquisition mode of the EMCCD) by selectively cropping out the fluorescence signal coming from the fiber core region.

Once all the fluorescence data is collected the experiment is complete. Lastly, an additional background signal in the absence of the object is also recorded and subtracted from all the fluo-

rescence data to improve the SNR further. The processed fluorescence data is finally fed to the reconstruction algorithm, which yields our desired images.

2.6 Results

2.6.1 Fluorescence imaging

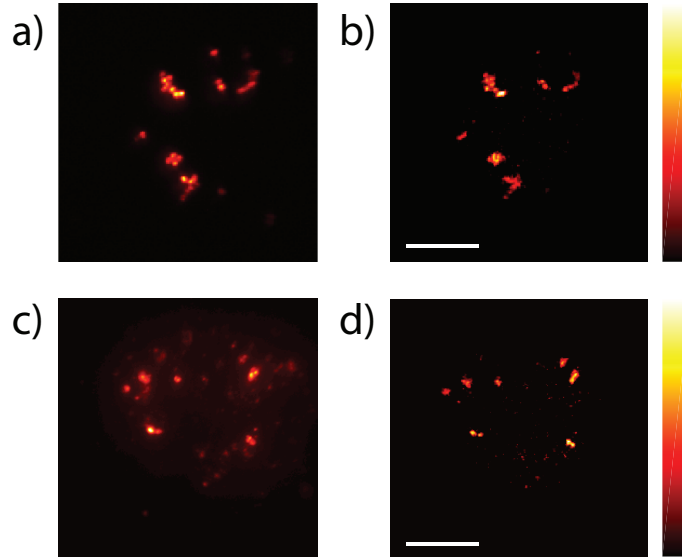


Figure 2.5: Experimental results of fluorescence imaging using an MMF with a numerical aperture of 0.29. a,b) Imaging of $4\ \mu\text{m}$ orange beads from TetraSpeck Fluorescent Microspheres Sampler kit: a) Widefield fluorescence image captured on the distal side of the fiber. b) 192×192 pixel object reconstruction using 10000 speckle patterns. (c,d) Fluorescence imaging of red fluorescent retrobeads in a mouse brain slice: c) Widefield fluorescence image of the sample. d) 192×192 pixel object reconstruction using 10000 speckle patterns. Scale bar is $30\ \mu\text{m}$.

We perform imaging of $4\ \mu\text{m}$ orange beads from a TetraSpeck fluorescent microspheres sampler kit and summarize the results in Fig. 2.5. Fig.2.5 a shows a reference widefield fluorescent image that was obtained with a CMOS camera directly imaging the fluorescent sources at the output/distal side illuminated with speckle patterns. The image is averaged over 1000 speckle pattern illuminations. The 192×192 pixels ($N = 36864$) image from fluorescence collected at the input/proximal side of fiber is shown in Fig. 2.5 b. It can be observed that the complex distribution of beads is well-recovered while preserving the boundaries of both individual and clustered beads.

$M = 10,000$ speckle patterns were used to reconstruct the image, corresponding to about 25% of the total number of reconstructed pixels.

We also performed imaging of red fluorescent retrobeads ($0.05 - 0.2\mu\text{m}$) from Lumafluor, microinjected into the dorsomedial striatum (DMS) of a mouse brain, which was then sliced and mounted on a microscope slide. This sample has a thickness of $30\ \mu\text{m}$. Fig. 2.5 c shows a reference widefield fluorescent image of the sample and Fig. 2.5 d shows the corresponding image reconstructed with our approach, and also clearly demonstrates the recovery of individual clusters of retrobeads in neurons.

It can be observed that the resolution of the reconstructed object is dictated by the grain size of the speckle produced by the excitation wavelength, thanks to which the reconstruction image on Fig. 2.5 d is better resolved than the reference widefield fluorescence image on Fig. 2.5 c obtained by direct imaging with the longer wavelength fluorescent light. Another interesting feature that can be observed is that the sparsity assumption allows a better z-sectioning by eliminating the out-of-focus features from the reconstruction image seen in the reference widefield fluorescence image on Fig. 2.5 c.

2.6.2 Influence of speckle pattern selection

We further present an analysis on the effect of choosing an optimal set of speckle patterns with least cross-correlations for imaging. The selection is made using the algorithm described in section 2.3. Fig. 2.6 a illustrates an example showing how speckle pattern optimization affects the image quality when imaging with $M = 3000$ speckle patterns. When the 3000 speckle patterns are chosen randomly out of a larger set of 10000 patterns, the reconstructed image is shown in Fig. 2.6 a (middle image, "No Optimization") and when an optimized set of 3000 speckle patterns is chosen for imaging, a better recovery of the image is obtained as illustrated in Fig. 2.6 a (right image, "After Optimization").

In Fig. 2.6 b and c respectively, we further demonstrate imaging with higher compression ratios, N/M using a range of decreasing number of optimized speckle patterns and observe the trend

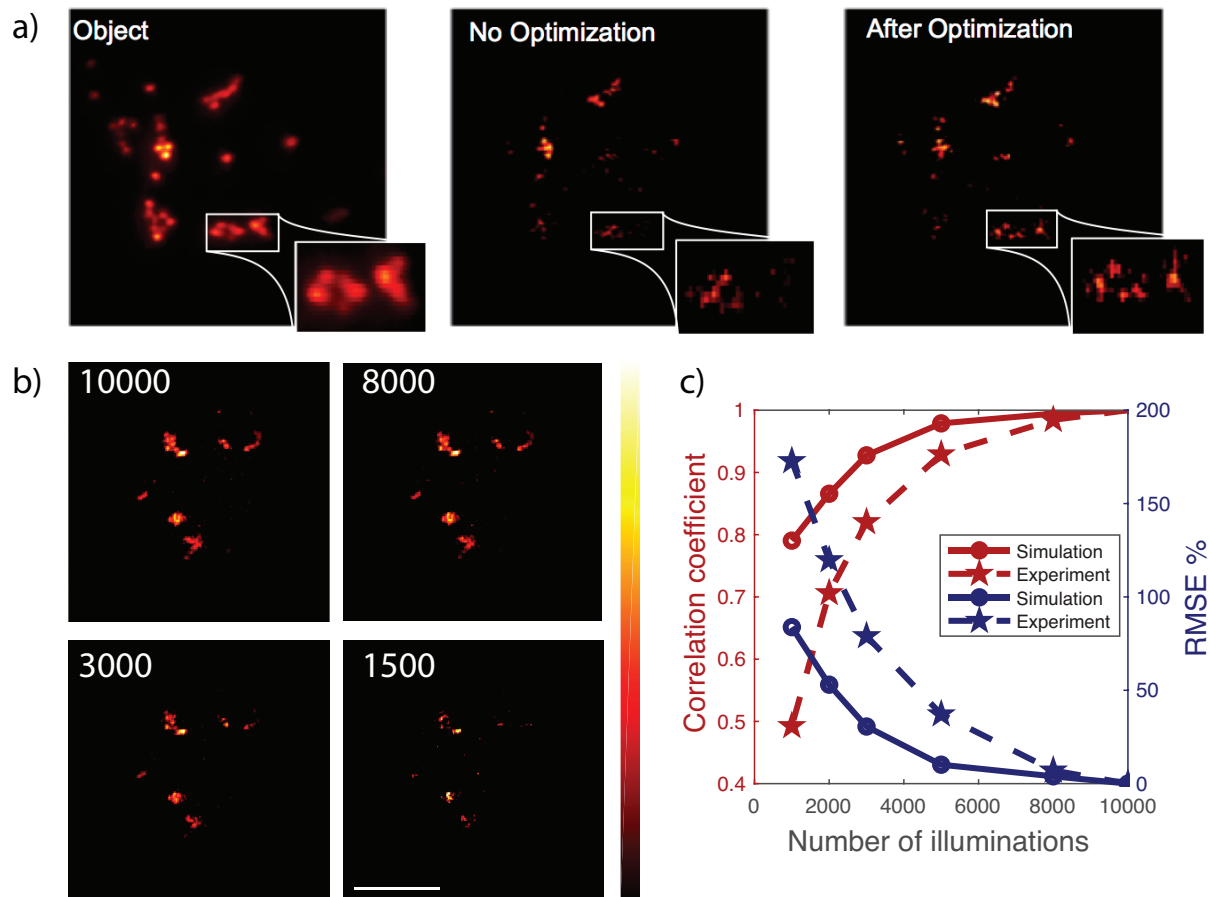


Figure 2.6: Effect of the set of speckle pattern optimization on the reconstructed images of $4 \mu\text{m}$ orange beads from TetraSpeck Fluorescent Microspheres Sampler kit using optimized patterns. (a) Left: widefield fluorescence image. Middle: image reconstructed with $M = 3000$ speckle patterns randomly chosen out of 10000 speckles patterns. Right: image reconstructed with $M = 3000$ speckle patterns chosen as to minimize cross-correlations between speckle patterns. The image obtained without optimizing the choice of speckle patterns misses some features of the original object. The image obtained after optimization illustrates the improved sampling efficiency for an optimized choice of the speckle patterns. (b) Reconstructed images using different number M of speckle patterns. The set of 8000, 3000 and 1500 speckle patterns were chosen optimally out of the 10000 available speckle patterns in order to minimize the cross-correlations inside each speckle set, as for (a). (c) Plots of correlation coefficient and relative mean square error (RMSE) between reconstructed images and the reference image ($M_{\text{max}} = 10,000$), as a function of the size M of the speckle set.

in reconstruction quality. In Fig.2.6 b, we begin with the full speckle pattern set of $M = 10,000$ and decrease the M value down to 1500 patterns. We observe that with M as low as $M = 3000$, a $N = 40,000$ pixel image remains recoverable while maintaining a good qualitative correlation coefficient with the reference image, whereas for $M = 1500$, significant features of the object are lost. Fig. 2.6 c provides a more quantitative insight into how the size of the speckle set influences the reconstruction in terms of the relative mean square error shown in blue and the correlation coefficient shown in red, of the reconstruction images with respect to the reference image. Simulation data for this plot are obtained by using signal values computed from equation 2.2 with A containing the chosen set of experimentally measured speckle patterns and the object O as the image 2.5 b with $M=10,000$. Both simulated and experimental curves show a decay in error and increase in the correlation coefficient with increasing number of patterns, as expected. The effect is more pronounced in the case of the experimental data, which is likely due to the influence of experimental noise.

2.7 Hybrid photoacoustic and fluorescence imaging

Note: The work presented in this section is part of a collaboration with Dr. Antonio Caravaca and Prof. Emanuel Bossy. The experimental results shown were obtained by Dr. Antonio Caravaca.

So far we demonstrated the use of the speckle imaging technique for fluorescence imaging. However, the technique is not limited to one modality. Fluorescent indicators offer good molecular specificity and a direct measure of the fast spatio-temporal calcium dynamics. However, they are insensitive to the vascular hemodynamics and blood oxygenation variations, which provide valuable complementary information about neurovascular coupling in health and disease. On the other hand, photoacoustic imaging is an emerging multi-wave imaging modality that couples light excitation to acoustic detection via the photoacoustic effect (sound generation via light absorption). It provides images of non-radiative optical absorption typically from endogenous contrast agents such as hemoglobin or melanin. While the capacity of photoacoustic imaging for resolving vascular hemodynamics is well-established [91], their lack of molecular specificity has allowed only indirect

and delayed measurement of neural activation.

Combining fluorescence and photoacoustic imaging is therefore attractive to obtain complementary information [185] and has proved effective for intracellular temperature mapping [71], superficial tumor detection [3, 101, 191] and surgical guidance [120]. Recently, photoacoustic imaging has also been employed for calcium imaging using the photoacoustic contrast of certain fluorescent calcium indicators [48] or using photoacoustic calcium indicators for combined photoacoustic and fluorescence imaging [153] with promising results. This combination can enable simultaneous monitoring of fast spatio-temporal neurodynamics and vascular hemodynamics, hence providing unprecedented capabilities for neural activity detection.

Combining the two modalities in a multimode fiber endoscope is possible [33] by employing a pulsed laser instead of a continuous wave laser to observe the photoacoustic signal and an additional commercial fiber optical hydrophone (FOH) attached to the MMF for the photoacoustic feedback. The hydrophone can measure the acoustic pressure optically using a Fabry-Pérot interferometer at the fiber tip [127]. It has a broadband detection from 1MHz to 30 MHz and is a bucket detector providing a voltage signal proportional to the total pressure detected. The FOH also has a diameter of $125\ \mu\text{m}$ and is attached next to the MMF, making the entire footprint of the endoscope $250\ \mu\text{m}$. Imaging of red blood cells along with fluorescent beads is demonstrated in figure 2.7.

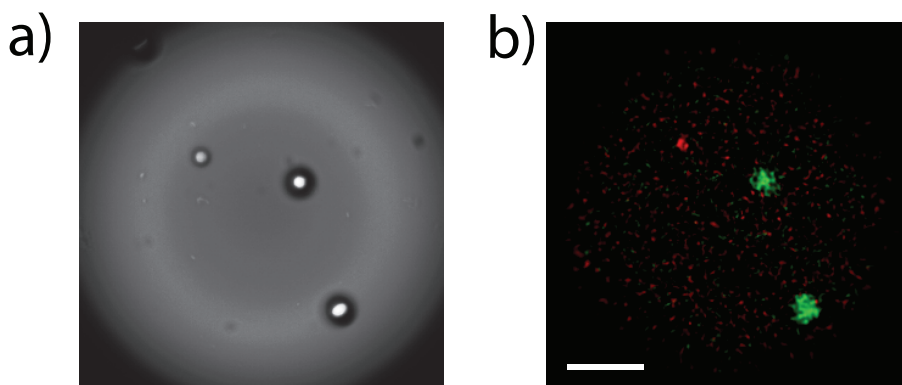


Figure 2.7: Hybrid imaging of red blood cells and $11\ \mu\text{m}$ diameter fluorescence particles dyed with Nile red. a) Bright-field microscope image of the sample at the distal tip using the calibration CMOS camera b) False color hybrid image reconstruction of the red blood cell (in red) and the fluorescence particles (in green). Scale bar is $30\ \mu\text{m}$.

2.8 Conclusion

We present a technique to simplify imaging through MMFs by employing their natural output illuminations i.e., speckle patterns for scanning the object of interest. We show that using speckle patterns is more efficient as it allows multiplexing our measurements by extracting information about the object from multiple points simultaneously. This eliminates the need for wavefront shaping to control the output illumination of the fiber and shifts the complexity of demultiplexing information from the experiment to a computer. Computational complexity is less of a problem since once the data is acquired, its reconstruction can be done offline and does not need active input from the imaging system.

Furthermore, this technique relies purely on intensity measurements, which can all be made in single-shot without needing interferometric stability. This makes the system simpler, more robust and useful in dynamically changing environments. Another limitation that we overcome is the presence of blind spots in images due to holes in the reference field used during TM calibration. Since the reference field in the TM method also propagates through the fiber and ends up being a speckle pattern, it has nulls where field information cannot be gathered and focal spots cannot be created. This leads to non-uniformity in the reconstructed images, which can be avoided altogether through speckle imaging.

We also presented a method to optimize the speckle pattern set for a stationary MMF system, such that maximum information about the object can be recovered using the smallest possible number of speckle patterns, hence improving the imaging speed. We showed good quality recovery of 40,000 pixel objects using as few as 3000 speckle patterns which leads to a compression ratio, N/M of 13, making the imaging frame rate 13 times faster. Furthermore, we demonstrate that the sparsity assumption helps achieve some degree of optical sectioning and resolution improvement. These improvements however come at the cost of reduced SNR due to use of fewer illumination patterns and their spread out nature.

Nevertheless, we show that the technique is not limited to fluorescence and combining it with

photoacoustic imaging in a single endoscope can allow extracting complementary information about the object. The combination of photoacoustic and fluorescence imaging - two prevalent imaging modalities for in-vivo imaging through biological tissue - put together in a 250 μm thin fiber system makes for a powerful tool that could have a range of biomedical applications, including deep brain neural activity detection.

2.9 Appendix

2.9.1 Fast iterative shrinkage-thresholding algorithm (FISTA) for sparsity constrained optimization problems

Gradient descent algorithms are effective for solving optimization problems with a differentiable cost function. For non-smooth functions like in Eq. 2.4, a class of iterative shrinkage thresholding algorithms are typically employed [45, 63, 38] which are rooted in the proximal forward-backward iterative schemes [26, 141] for solving convex problems with a non-smooth term in the cost function.

Let us consider the general minimization problem shown in Eq. 2.7.

$$\min_x F(x) = f(x) + g(x) : x \in \mathbb{R}^n \quad (2.7)$$

where $f(x)$ is a smooth convex function which is continuously differentiable with Lipschitz continuous gradient $L(f)$ and $g(x)$ is a continuous and non-smooth convex function.

We know that if $g(x) = 0$, the above problem can be solved using the iterative gradient algorithm with the k^{th} iterate given by Eq. 2.8.

$$x_k = x_{k-1} - t_k \nabla f(x_{k-1}) \quad (2.8)$$

where $t_k > 0$ is a suitable step size. The above gradient iteration can be rewritten as a proximal regularization [42] of the function f at x_{k-1} described in Eq. 2.9.

$$x_k = \operatorname{argmin}_x \left\{ f(x_{k-1}) + \langle x - x_{k-1}, \nabla f(x_{k-1}) \rangle + \frac{1}{2t_k} \|x - x_{k-1}\|^2 \right\} \quad (2.9)$$

In the equation above, the first two terms in the curly braces are the first order Taylor expansion of the function $f(x)$, and the third term corresponds to the maximum quadratic curvature of the function.

In our case, $g(x) = \lambda\|x\|_1$, so the corresponding iterate is given by Eq. 2.10.

$$x_k = \operatorname{argmin}_x \left\{ f(x_{k-1}) + \langle x - x_{k-1}, \nabla f(x_{k-1}) \rangle + \frac{1}{2t_k} \|x - x_{k-1}\|^2 + \lambda\|x\|_1 \right\} \quad (2.10)$$

We now choose $1/t_k = L$, which is ideally chosen to be the curvature of the function f at a given point. For any $L > 0$, let us now define the function in curly braces above at an arbitrary point y , instead of the last iterate, x_{k-1} and call it $Q_L(x, y)$ as shown in Eq. 2.11.

$$Q_L(x, y) = f(y) + \langle x - y, \nabla f(y) \rangle + \frac{L}{2} \|x - y\|^2 + \lambda\|x\|_1 \quad (2.11)$$

Further, we define the minimizer, $p_L(y) = \operatorname{argmin}\{Q_L(x, y) : x \in \mathbb{R}^n\}$. ISTA algorithms solve this problem by evaluating every new iterate $x_k = p_L(x_{k-1})$, hence resulting in a convergence in function values as $O(1/k)$, where k is the iteration number.

On the other hand, the FISTA algorithm evaluates the new iterate at a third point, y which is calculated with knowledge of the last two iterates instead of only the last one. The calculation of the iterates of x and y values are summarized in Eqs. 2.12, 2.13, 2.14.

$$x_k = p_L(y_k) \quad (2.12)$$

$$y_{k+1} = x_k + \left(\frac{t_k - 1}{t_k + 1} \right) (x_k - x_{k-1}) \quad (2.13)$$

$$t_{k+1} = \frac{1 + \sqrt{1 + 4t_k^2}}{2} \quad (2.14)$$

The initial value for t is chosen as 1 and the initial y value is chosen to be the same as the initial x value, x_0 . By evaluating every new iterate at y , which has memory of both the last two iterates, helps minimize overshooting outside the solution space and enables a much faster, non-asymptomatic convergence rate of $O(1/k^2)$.

Chapter 3

High speed focusing using a 350 kHz wavefront modulator

3.1 Introduction

In Chapter 2, we discussed that the use of speckle patterns for imaging through MMFs can help reduce the number of required measurements, hence improving imaging speed. The fundamental limit of the MMF imaging speed however is determined by the wavefront shaping rate. Wavefront shaping (WFS) is a key aspect in imaging through scattering media, be it biological tissue, a ground glass diffuser or a multimode fiber. Measuring the TM by shaping the incident wavefront allows controlling the field on the distal side of the medium, which is used to scan an object. Luckily, the WFS technology has seen rapid advances in the last couple decades and many options have become commercially available. Figure. 3.1 presents a summary of the state of the art devices used for WFS along with their speed and number of pixels they support.

The most widely used WFS devices are liquid crystal spatial light modulators (SLMs) which have millions of independent active pixels fitted in a few centimeter square area and are capable of phase modulation. These comprise of nematic liquid crystals on which a voltage can be applied to change their orientation, hence modulating the phase delay gathered by the light propagating through them. Modulation speed of these devices can go up to 100 Hz, limited by the switching speed of nematic crystals. SLMs can alternately also comprise of ferroelectric crystals [113], which are binary, but have faster switching speed leading to a wavefront modulation rate of up to a few kHz. Another type of SLM are based on micro-electromechanical system (MEMs) mirrors [22]. Each mirror can be actuated by applying a piston to it to achieve varying phase delays. These have

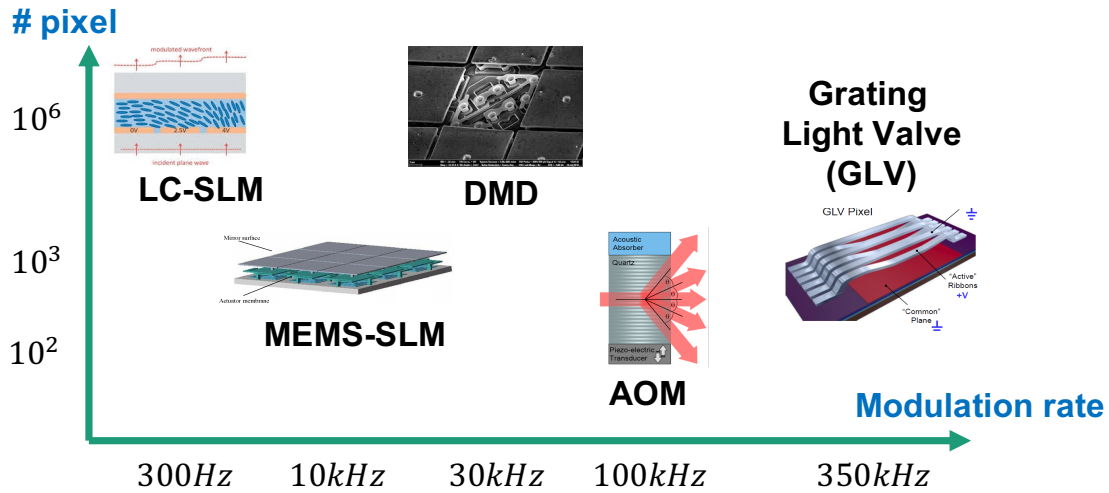


Figure 3.1: Map of different wavefront shaping devices in terms of modulation speed and number of modulating pixels.

thousands of pixels and can operate at about 10 kHz.

DMDs on the other hand are binary amplitude modulators which have mirrors that can be deflected at two angles to turn the pixel on or off. Although they are designed for amplitude only modulation, groups of pixels can be combined to project gratings on them, which can be shifted to achieve phase modulation in the Fourier plane of the DMD. One of the techniques to implement this is Lee holography [30] and was introduced in chapter 2. Since DMDs have millions of pixels, sufficient pixels are available even after grouping them into macropixels. Their fast modulation speed of 22 kHz combined with their independence to polarization and broadband operation makes them attractive candidates for imaging through scattering media.

Another type of WFS technology consists of programmable acousto-optic deflectors (AODs). These are comprised of an acousto-optic crystal through which an applied RF signal allows creating a refractive index grating. This grating can be programmed to deflect light into a desired order and modulate its phase. Experimental demonstration of focusing through scattering media [60] using AODs has been done with hundreds of independent pixels and impressive modulation speeds up to 155 kHz. Scaling of the number of pixels is possible by increasing the crystal size.

A faster yet solution is offered by 1-D devices called grating light valves (GLVs). These

are also MEMs based and consist of ultra-light aluminium coated ceramic ribbons that can be moved with the help of an applied voltage. GLVs stand out from the above technologies in their superior switching speed of a few 100 kHz and their one-dimensional geometry. Adapting them to our application of focusing through scattering media and implementing a system design that works around it will be the focus of this chapter.

We will also explore in this chapter, some of the interesting effects of using a 1-D modulator to control 2-D fields. When a wavefront incident on a weak scatterer is tilted within an angular range, the output wavefront is equally tilted in the near field, leading to a translation of the far-field speckle pattern. This phenomenon is known as the memory effect [68, 61, 95], and is illustrated in figure 3.2 a. In the presence of large memory effect, when the illumination on the scatterer is elongated along one of the spatial dimensions, the speckle pattern appears elongated in the perpendicular direction, thereby hindering full control over the field in both dimensions.

However, we will show that by reshaping the line illumination from the GLV into a square-shape by employing different magnifications along the horizontal and vertical directions, we are able to achieve speckle patterns with isotropic statistics after the scatterer, regardless of its scattering strength. We demonstrate this principle in simulation by modeling our system along with scatterers with varying degrees of memory effect. By employing the right illumination configuration, we enable full 2D control over the output field and perform a 1D to 2D transformation of light through the scatterer.

Furthermore, we perform focusing experiments using the TM method at a record speed of 2.4 ms. We show focusing through different scattering media such as a ground glass diffuser, chicken breast, TiO_2 and a multimode fiber. We also perform dynamic focusing while the speckle pattern incident on the detector is translated in real-time to present statistical analysis of the focusing performance. We also show the dependence of the focus quality on the number of modes used for TM calibration and the pixel binning factor. Finally, to demonstrate the fast wavefront shaping speed of the system, we perform continuous focusing through a rapidly changing dynamic sample. The decorrelation time, defined as the time duration within which the correlation of a changing

speckle field with its initial state remains above a certain threshold value, of the dynamic sample used in our experiment was about twice the focusing time.

3.2 2D control through scattering media using a 1D modulator

When a 1-D light beam is incident on a scattering medium, it scatters through its length and all the independent modes that were aligned along one dimension are spread out in a two dimensional space giving rise to a 2-D speckle field. If the scatterer is strong and allows complete spreading of modes in 2-D such that the resulting speckle field is fully developed and has no memory effect, the 1-D GLV can control the 2-D speckle field in a manner similar to that of a 2-D SLM with the same number of independent pixels. However, when the scatterer has memory effect, the resulting speckle fields can exhibit translational correlations that lead to speckle fields preserving some structure from the incident fields.

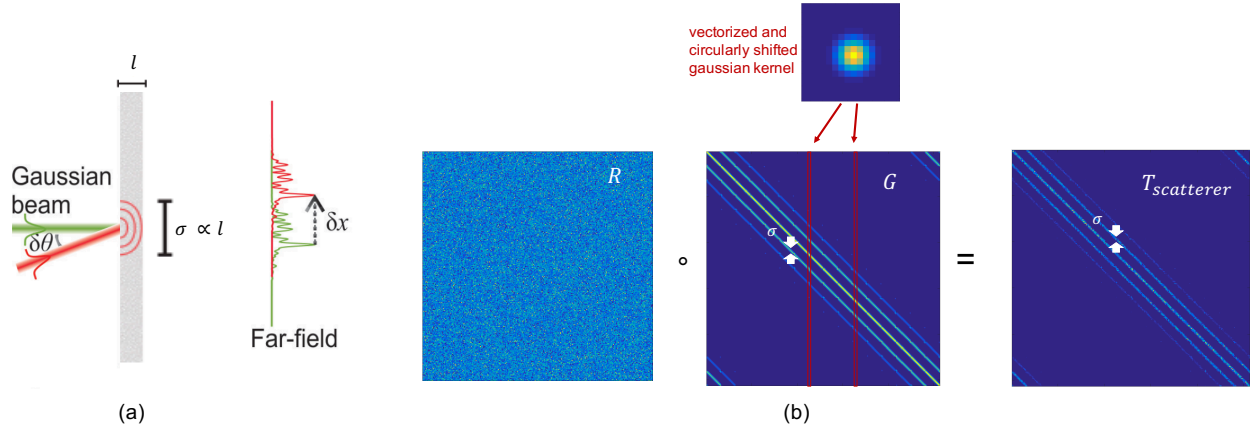


Figure 3.2: Model of a scatterer with memory effect. (a) A point source incident normally on a thin scatterer of thickness l spreads out with a Gaussian distribution and standard deviation, σ that increase in proportion to the thickness. When the point source is incident, tilted at an angle $\delta\theta$ to the normal, the near field distribution after the scatterer also experiences the same tilt, leading to a spatial shift, δx of the original speckle pattern in the far-field. (b) The TM of a scatterer with memory effect can be modeled as the Hadamard product of a random matrix and a convolution matrix with a circular Gaussian kernel whose standard deviation is σ . The TM for 2-D fields corresponding to a scatterer with $\sigma = 3$ is shown on the far right. The image represents the absolute value of the TM and shows a specific band-diagonal structure.

We analyze the effect of such correlations by building a model to mimic a scatterer with

varying degrees of memory effect similar to the one proposed by Judkewitz et al. [95], but instead extended from 1-D to 2-D fields. By propagating fields arriving from the GLV through the scatterer, we can predict the shape of the resulting speckle fields.

3.2.1 Model of a scattering medium with memory effect

A scattering medium with memory effect has two distinct properties namely random scattering and spatial correlations within a certain range. While the former can be modeled using a random TM, the latter is characterized by shift invariance in a certain region around the source which can be represented using a convolution matrix with a circular Gaussian kernel. The standard deviation of the Gaussian kernel here, σ corresponds to the spatial extent or spread of a point source after propagating through the scatterer.

It therefore follows that combining the two effects, the 2-D TM of a scatterer with memory effect, $T_{scatterer}$ can be mathematically described by eqn. 3.1 where R is a simulated random matrix, whose columns represent vectorized 2-D random speckle fields and G is a convolution matrix, whose columns contain vectorized and 2-D Gaussian fields with standard deviation σ , circularly shifted by a pixel every column, to cover the entire field of view (FOV). The symbol \circ denotes the Hadamard or element-wise product.

$$T_{scatterer} = R \circ G \quad (3.1)$$

The σ value above is directly proportional to the length of the scatterer and is a measure of the scattering strength of the medium. The matrix model is depicted in figure 3.2 b.

3.2.2 Speckle shape analysis

Once we have our model for the TM of the scatterer, we can propagate the incoming field from the GLV through it and simulate the speckle patterns in the far field. Here we consider two configurations for the illumination of the scatterer namely the 2-D image plane of the GLV in which each pixel is stretched horizontally such that the 1D line beam from the GLV is transformed to a

square using cylindrical lenses and a 4-F system, and the 2-D Fourier transform of the above image plane. We refer to them as image plane and Fourier plane illuminations respectively for conciseness.

Figure 3.3 (g) shows a plot of the evolving speckle shape for scatterers with increasing thickness. Elongation factor is defined here as the ratio of major and minor axes of the average speckle grain and the average speckle grain is computed here by the autocorrelation of the output speckle fields. It can be observed that the elongation factor drops at a rate $1/\sigma$ for the case of Fourier plane illumination, while it constantly remains near unity in the case of image plane illumination, even for a small σ value. Hence, the image plan illumination is more suitable for thin scatterers in order to allow full 2-D control on the output fields.

The results are summarized in figure 3.3. We can observe that in the case of Fourier plane illumination that consists of a 1-D array of spots, the far field speckles appear elongated in the orthogonal direction of the illuminating array. With increasing scatterer thickness, this elongation decreases and the speckle grains become more isotropic. The same effect will occur for a scatterer of a given thickness and decreasing mean free path.

On the other hand, during image plane illumination, where the two orthogonal axes have been magnified differently such that the GLV image illuminating the scatterer is square-shaped, round speckle patterns are always observed irrespective of the scatterer thickness, as depicted in figures 3.3 (d,e,f).

3.3 Experimental Setup

The experimental setup for focusing through scattering media using a GLV is depicted in figure 3.4. We used a continuous wave 532 nm laser for the majority of our experiments and a 460 nm laser for one of the experiments done in the Fourier plane illumination configuration. The laser beam is expanded and collimated using a 4-F system and focused down to a 1-D line on the GLV using a cylindrical lens. The GLV is tilted at a small angle of about 10° to deflect the reflected light to another cylindrical lens which collimates it into a square-shaped beam. It is critical to achieve a truly isotropic square-shaped illumination experimentally because breaking the isotropy

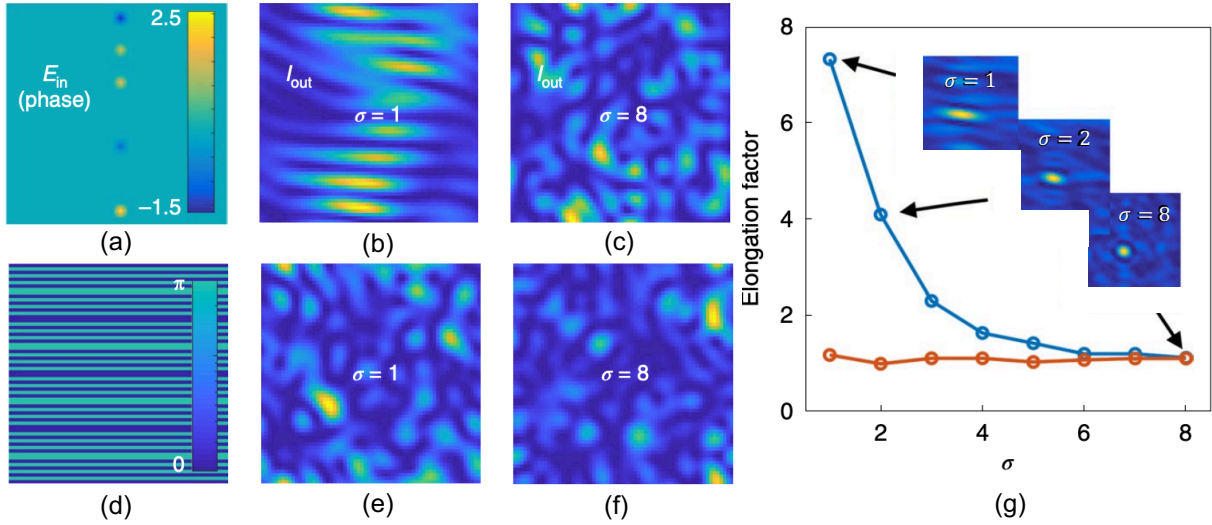


Figure 3.3: Speckle shape analysis for different illumination configurations and varying scatterer thickness. (a) Fourier plane of the GLV phase pattern. A zoomed in part of the phase map of 1D spots is depicted. The colour bar represents phase values. (b,c), Simulation of speckle fields after scatterers with $\sigma = 1$ and 8, respectively, when the GLV Fourier plane shown in (a) propagates through them. The images show speckles intensities in the scatterer far field. (d) Image plane of the GLV phase pattern. The 1D pixels with alternating phases and constant amplitude are expanded to horizontal stripes. The colour bar represents phase values. (e,f) Simulation of speckle fields after the scatterer with $\sigma = 1$ and 8, respectively when the GLV image plane shown in (d) propagates through them. (g) Speckle elongation as a function of scatterer thickness or σ for Fourier plane (blue) and image plane (orange) illumination. The plot shows that the elongation in speckle patterns reduces at a rate $1/\sigma$ of decreasing scatterer thickness for Fourier plane illumination, while it remains absent, with a unity elongation factor in the case of image plan illumination. Each data point in the plot is averaged over 100 random realizations of the scatterer. The insets within the plot illustrate the evolving characteristic shapes of speckle autocorrelation when $\sigma = 1$, 2 and 8, respectively, during Fourier plane illumination.

of the beam can cause recurrence of elongation in the output. This is done by carefully controlling the magnification of both the axes of the beam by a precise alignment of the cylindrical lenses to prevent any astigmatism. The lenses are mounted on tilt-controlled stages and their alignment is optimized to remove any residual elongation in the output speckle.

A 4-F system, with an aperture in the Fourier plane to block the reference beam during focusing, then images the square-shaped GLV plane onto the scatterer or the back focal plane of an 20x magnification objective, depending on whether the image plane or Fourier plane configuration is used.

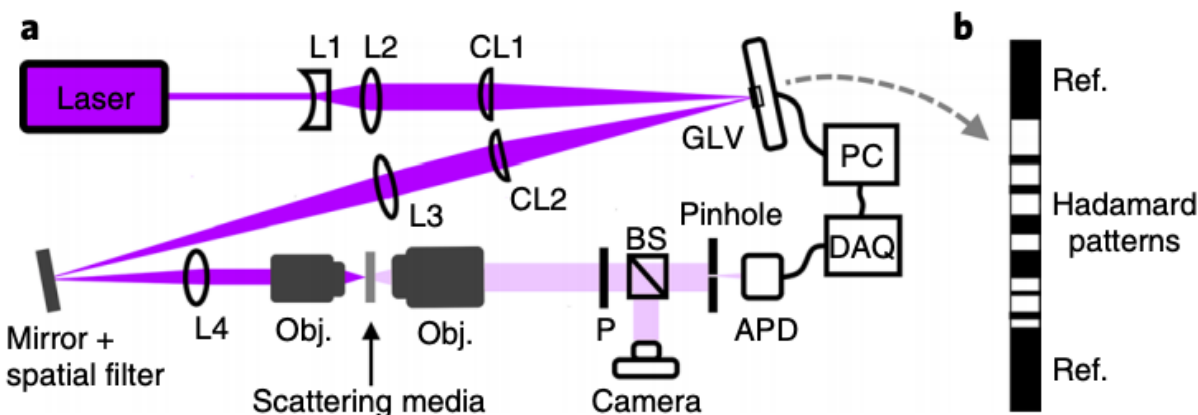


Figure 3.4: Experimental Setup for focusing through scattering media using a GLV. A laser beam illuminates the GLV, whose reshaped image or Fourier plane illuminates the scatterer. The output plane of the scatterer is then imaged using an objective lens, through a pinhole onto an APD. The same image is also relayed to a camera for monitoring the full speckle field. L1–L4: lenses with focal lengths 50 mm, 300 mm, 300 mm and 50 mm respectively; CL1–2: cylindrical lenses each with focal lengths 150 mm; Obj.: microscope objectives; P: polarizer. The set-up above shows the Fourier plane illumination configuration and can be switched to image plane illumination by removing the objective lens before the scattering medium. b, An example phase pattern showing one of the 1D Hadamard basis elements, surrounded by a reference during TM calibration.

A 10x magnification objective is used to image the output speckle field. A linear polarizer permits one of the linearly polarized components of the speckle field to be detected, which is then split into two arms using a beamsplitter. One arm goes to a pinhole followed by a fast avalanche photodiode (APD) that measures the intensity of the speckle grain to be optimized. The pinhole size is adjusted to match the speckle grain size and reject the remaining part of the speckle field.

The APD voltage is digitized using a fast data acquisition card (DAQ) and sent to the computer to calculate the optimized wavefront for focusing. The second arm goes to a camera that records the entire speckle field for reference. We use the TM method detailed in chapter 1 for focusing. 1-D binary Hadamard patterns are projected in the central part of the GLV active area along with a reference field on their either sides, as depicted in figure 3.4 b. The patterns are preloaded on the GLV to eliminate delay from data transfer between the PC and the GLV and perform wavefront update at maximum frame rate. Each field measurement is made using three phase measurements ($0, \pi/2, \pi$, as before. We used 64 to 1024 number of modes for different optimizations and the calibration time scaled in proportion to the number, between 2 ms to 10 ms respectively.

The optimized wavefront for focusing is displayed on the GLV immediately after calibration with a delay of less than $250 \mu\text{s}$. Since the reference pixels do not contribute to the focus intensity, a high frequency grating is projected on them that diffracts light into the higher orders, which can then be blocked using the aperture in the Fourier plane of the 4-F system after the GLV. A bright focal spot appearing in the speckle field whose intensity is proportional to the number of modes used for optimization, can be viewed on the reference camera.

3.4 Results

We performed focusing through different scattering media to demonstrate the real-time focusing performance of the GLV. While a C++ program, that controls all system computation and synchronization, handles the TM calibration and optimal wavefront projection for focusing, the camera monitors the speckle pattern evolution in real-time. The results are presented in detail in the sections below.

3.4.1 Focusing through a ground glass diffuser and dynamic media

We first performed focusing through a ground glass diffuser with a diffusion angle of $\sim 5^\circ$ (Thorlabs, DG05-1500) in the image plane configuration. Here we used either $N = 256$ or 512 modes for TM measurement, which needed $3N = 768$ or 1536 pattern updates on the GLV. Figure

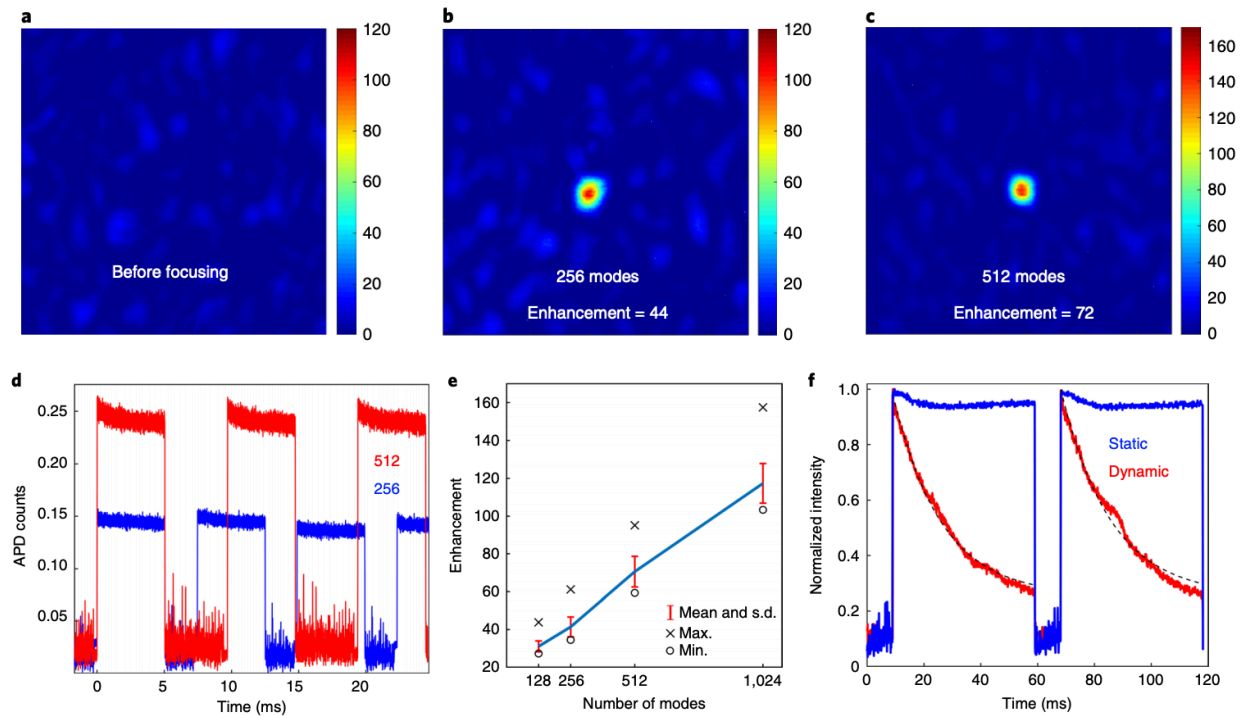


Figure 3.5: Focusing through a ground glass diffuser and dynamic scattering samples using the GLV. (a) Speckle field before optimization. (b) Focal spot created during the optimization program using 256 modes for TM measurement. (c) Focal spot created during the optimization program using 512 modes for TM measurement. Colour bars represent the intensity on the camera. (d) APD signal measuring the intensity of the speckle grain being optimized while the optimization program is running. The blue and red curves correspond to optimizations using 256 and 512 modes respectively. (e) Enhancement statistics while focusing through a ground glass diffuser. Each data point represents the mean enhancement measured from 500 frames captured during a different optimization. The errorbars show the standard deviation and the cross marks and circles represent the maximum and minimum enhancement values. (f) APD signals while continuous focusing through a static and a dynamic scatterer using 1024 modes for optimization. The blue curve corresponds to the static sample with gelatin and lipid concentrations of 2.5 mg ml^{-1} and 0.5% and the red curve corresponds to the dynamic sample made with a more dilute solution containing gelatin and lipid concentrations of $5 \mu\text{g l}^{-1}$ and 0.01% . By fitting an exponential to the curve for the dynamic sample (shown in dotted black), we find that its speckle decorrelation time is approximately 17 ms. All above experiments were done using an excitation wavelength of 532 nm.

3.5 (a) shows the speckle field before TM calibration and 3.5 (b,c) show snapshots from the camera while the focus optimization program is running, using $N = 256$ or 512 modes respectively for TM measurement. A single optimization cycle involves TM measurement for 2.4 ms or 4.7 ms when using $N = 256$ or 512 modes respectively, followed by optimal wavefront projection for focusing for another 5 ms. The frame rate of the camera was around 30 ms, which means the images obtained are averaged over multiple TM calibration and focus projection cycles.

We can observe that the focus enhancement, which we define as the ratio of the peak focal intensity and the average intensity of the optimized speckle field, increases with the number of modes, N . The signal recorded on the APD at any given time during the two optimizations is shown in figure 3.5 (d). The dips in the intensity signal correspond to the TM measurement time and the peaks correspond to focus projection time. It can be observed that the optimization using 512 modes takes about twice as long as the optimization using 256 modes as we expect.

We also performed a statistical analysis of the focusing performance of the GLV while the optimization program ran, by recording movies of the speckle field as it was translated with the help of an adjustable mirror. The moving speckle field resulted in a new speckle grain reaching the APD through the pinhole, hence representing different optimizations every cycle. Figure 3.5 (e) shows the errorbars of focal spot enhancements from 500 selected frames shown as a function of the number of modes used for TM measurement.

The plot shown is obtained by selection and post-processing of the raw image frames extracted from the recorded movies. This involved selecting 500 out of 2000 frames in each movie to report focusing optimizations of speckles with a measurable reference signal, based on the following criteria. First, we removed frames in which the focus was located at the edge of the speckle field because the negligible background beyond the speckle field led to amplified enhancement. For this, we calculated the deviation of the mean pixel value in all the frames and discarded the frames that had anomalously high deviations. Second, the images where the pre-optimization reference speckle was weak at the desired focus position, typically showed lower enhancement. The frames with enhancements lower than a threshold value were removed to this end. We also removed pixel noise

by median filtering to ensure correct calculation of the enhancement. Finally, we applied a duty cycle correction on the enhancement values to account for the fact that the recorded frames are integrated over both measurement and focusing time. Effectively the statistical analysis represents 500 focusing optimizations of speckle grains overlapping with a measurable reference field.

As expected we observe an almost linear increase in enhancement with the number of modes. Example images of focal spots created using $N = 128, 256, 512$ and 1024 modes are shown in figure 3.6 (a-d). Here as well, we observe the focal spot enhancement improving consistently with the number of modes.

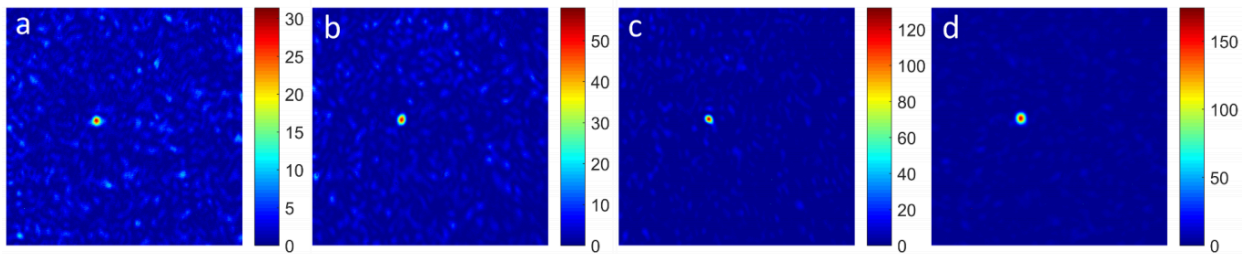


Figure 3.6: Evolution of focus enhancement as a function of number of modes used for TM measurement. Example images of focal spots created after a ground glass diffuser using (a) 128, (b) 256, (c) 512, and (d) 1024 modes show enhancement values of 30, 37, 62, 74 respectively.

Furthermore, to really take advantage of the optimization speed of the GLV we performed focusing through dynamic media in the image plane configuration. We created dynamic scattering solutions with different speckle decorrelation times by controlling their viscosities to mimic dynamic biological tissue using gelatin, water and intralipid. Towards this end, we heated 10 ml of water to 40° C and dissolved 50 mg of gelatin (ACROS gelatin type A) and 0.5 ml of intralipid (20% solution) to form a uniform solution. We then cooled down the prepared samples, diluted them further to shorten their decorrelation times and mounted them on a depression concave slide. The slides were positioned vertically on a slide holder after the microscope objective for focusing through them. This time we used 1024 modes for optimization that took 10 ms and projected the optimal wavefront for 50 ms.

Figure 3.5 (f) shows the APD signal during focus optimization through two of the samples

prepared in the above described manner. The less viscous sample whose focal intensity is shown in blue, is static in the 50 ms timescale hence retaining the focus intensity until the end of the cycle. On the other hand, for a more dilute sample indicated in red, that has a decorrelation time of about 17 ms, the created focus decays quickly because the sample medium is changing quickly. Nevertheless, thanks to the rapid focus optimization program, the focus can be recreated through the sample in another 10 ms and this process can keep repeating for as long as desired.

3.4.2 Focusing through multimode fibers

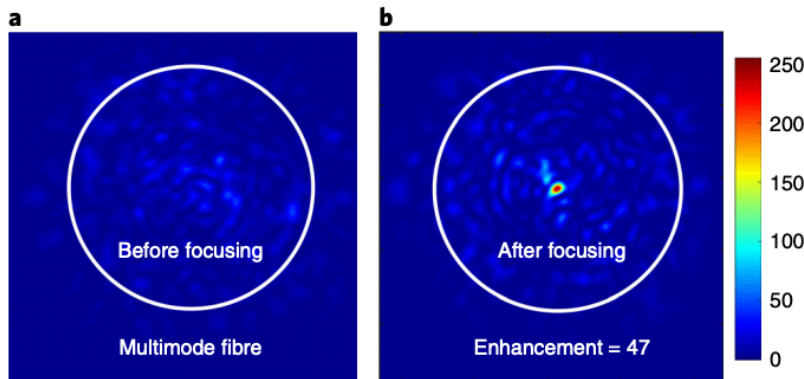


Figure 3.7: Focusing through a multimode fiber using the GLV. Speckle field (a) before and (b) after optimization. Colour bar represents the intensity on the camera. We employed the Fourier plane illumination configuration and 256 modes for TM measurement in the experiment and found enhancement values similar to that observed for other scattering media. The fibre used in the experiment is a graded-index MMF with a diameter of $50\ \mu\text{m}$ with 800 modes and has a length of 30 cm. The white circle demarcates the fibre core.

Having demonstrated the ability to focus through diffusers and dynamic media, we apply the technique to MMFs. Towards this end, we replace the diffuser with a 30 cm long MMF along with coupling optics that include a 20 x magnification microscope objective whose NA is matched to that of the fiber. The GLV image plane is incident on the back-focal plane of the fiber and another 20x microscope objective collects the light at its output and images it onto the APD and camera. Although the Fourier plane of the GLV is incident on the front facet of the fiber, we do not see any elongation due to the fact that MMFs do not exhibit translational memory effect. Light

propagating through the MMF is completely randomized leading to a random speckle field with round speckles, irrespective of the input illumination configuration. The optimization routine used with the MMF remained the same as described earlier. Figure 3.7 (a,b) show the output speckle fields before and after optimization.

3.4.3 Statistical analysis of enhancement

In this section we show the performance of our system as a function of several parameters namely number of modes, pixel ratio, and the type of scatterer. For all these experiments, we recorded movies of real time focusing through scattering samples while the output speckle field was manually translated with respect to the APD, using an adjustable mirror.

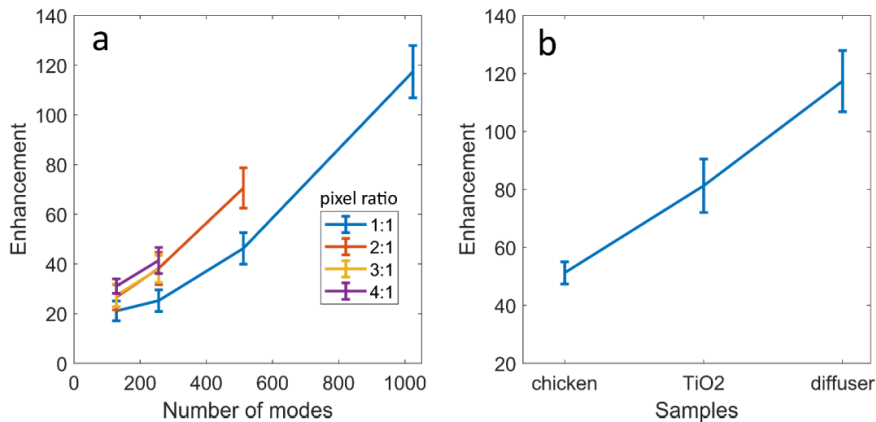


Figure 3.8: Statistics of GLV focusing performance as a function of pixel ratios and number of modes

In the first experiment we focus through a diffuser using different number of modes and pixel ratios. The term “pixel ratio” refers to the ratio of GLV pixels to Hadamard mode pixels or the binning size of individual GLV pixels. For example, a pixel ratio of 4:1 means that 4 GLV pixels were used to project each Hadamard mode pixel.

For the second experiment, we performed focusing through three samples - chicken breast, Titanium dioxide (TiO₂) nanoparticles solution, and a diffuser. The chicken breast was cut into a $\sim 500\mu\text{m}$ thick slice and mounted on a microscope slide and the TiO₂ sample was prepared

by diluting TiO_2 nanoparticles in water and drying it on a microscope slide. Figure 3.8 (a-b) summarize the statistics of the first and second experiment respectively.

The post-processing of all the movie frames in both experiments was performed exactly as detailed in section 3.4.1. We can observe from the plots that binning more pixels together and using more number of modes both contribute in improving enhancement. In the second experiment, focusing through a diffuser yields better results than a chicken breast and TiO_2 particles.

3.5 Discussion

We demonstrate the use of a 350 kHz phase modulator that enables imaging through scattering media at the millisecond timescale. The performance of the GLV as a wavefront shaper can be further improved by accounting for or modifying some of its non-ideal features.

The theoretically achievable focal intensity enhancement when focusing through a scattering medium using N number of independent phase control pixels, is $\pi(N-1)/4+1$ [181]. In experimental conditions, the enhancement can be lower due to the presence of noise [2]. The enhancement in our experiments was limited to 20% of the ideal case. This can be explained by a number of factors. Firstly, the common sources of noise in wavefront shaping resulting from wavefront distortions from dust or mechanical design imperfections in the optical system, diffraction effects due to the pixel pitch of the GLV, the unmodulated light in the zero order and measurement noise due to mechanical and thermal instabilities contribute in reducing the enhancement.

Besides these, some factors dependent on the GLV design also affect the enhancement significantly. One of these effects is caused due to the limited stroke size of the active ribbons on the GLV. While an ideal phase modulator allows a full range of 2π rad phase modulation, we could achieve a phase modulation range only slightly greater than $3\pi/2$ rad with the GLV, limited by the ribbon stroke size.

Another interesting effect arises due to the low fill factor of the GLV pixels, which results in a modulated background signal. Each independent GLV pixel is composed of six parallel active ribbons on which a voltage is applied to displace them along their surface normal for phase mod-

ulation. Some of the incident light misses the ribbons and is reflected back from the back-plane behind them. This light interferes coherently with the light reflected from the ribbons to generate a high-frequency diffraction grating, whose efficiency is modulated with the ribbon displacement. This modulated light component contributes to uncontrolled background in the optimized speckle, hence reducing the enhancement. This effect also explains the better performance of the TM measurement configurations which use a small number of pixels in the phase stepping reference relative to the number of fixed signal pixels. For example, when using 512 signal modes for TM measurement, the enhancement increases by $\sim 62\%$ when we double the signal to reference pixels ratio, as observed in Fig. 3.8.

We performed simulations to analyze the strength of a number of general and GLV-specific effects and the corresponding enhancement plot and further details are presented in the Appendix section 3. We find that the most significant effect is due to the modulated background signal.

Another source of error includes the non-uniformity of the incident beam, especially along the direction of the 1-D array of the GLV pixels. Although we overfill the GLV active area with the 1-D focused Gaussian beam, its intensity decreases away from the center. Hence the true TM modes deviate from the ideal modes that we assume for calculation of the optimal mask for focusing, leading to phase errors and reduced enhancement. This error can be corrected by using a beam with a larger waist or using a Powell lens for a flatter illumination.

Moreover, there are optical aberrations in the experimental setup. The use of cylindrical lenses makes the system susceptible to astigmatism. We carefully minimize the astigmatism in the system by using specialized mounts with tip/tilt and 3-D translation control and maximizing the symmetry of the beam in the far-field.

3.6 Conclusion

We present a fast wavefront shaping system using a grating light valve for focusing through scattering media at least more than an order of magnitude faster than other currently available wavefront modulators. Despite the 1-D design of the modulator, we show that it can be used to

control 2-D fields after the scatterer in a manner similar to a 2-D SLM does using an optimal optical configuration. We also present a statistical model for a scatterer with memory effect that helps us study the speckle shape as a function of the illumination condition and the strength of the scatterer.

Furthermore, we demonstrate record speed of focusing in 2.4 ms through various scattering media such a ground glass diffuser, chicken breast, TiO₂ particles and a multimode fiber. To take advantage of the real-time focus optimization, we also show continuous focusing through a dynamic scatterer. Finally, we present statistics of the focusing performance of the GLV by recording movies and measuring the focus enhancement, as different speckles are optimized in real time, demonstrating the robust and continuous system operation.

In the context of MMF imaging, the GLV can allow us to push the imaging speed from 2.2 frames/sec using DMDs to 35 frames/sec for a 100×100 pixel object. The fast calibration enables real-time adaptive correction of a rapidly bending fiber, when access to the distal side is possible.

3.7 Appendix

Note: The work presented in the appendix was a collaborative effort and is included for the sake of completeness of the description of this project. The results presented in section 3.7.1 were obtained by Dr. Omer Tzang and the results in section 3.7.3 were obtained by Dr. Simon Labouesse and Dr. Omer Tzang.

3.7.1 Phase calibration of the GLV

The displacement of the GLV ribbons with increasing applied voltage is highly nonlinear and depends on the wavelength and angle of incidence of the incident light as well as the optical alignment. Hence, the GLV voltage-to-phase curve has to be calibrated to ensure accurate phase modulation. Towards this end, we display square phase gratings on the GLV with the even pixels set to the minimum voltage, while the odd pixels are stepped up in voltage over the full voltage range and the zero order diffraction efficiency is recorded during this process. If we assume a perfect

square phase grating with period L , its amplitude transmission function is given by Eq. 5.11.

$$t(x) = 1 - [(1 - e^{j\phi}) \sum_{n=-\infty}^{\infty} c_n e^{\frac{j2\pi nx}{L}}] \quad (3.2)$$

c_n in the above equation correspond to the Fourier coefficients of the square phase wave defined as, $c_n = 1/2 \text{sinc}(n/2)$. The expression in the far field is the Fourier transform of the expression in Eq. 5.11, which is shown in Eq. 3.3.

$$F[t(x)] = \delta(f_x) - (1 - e^{j\phi}) \sum_{n=-\infty}^{\infty} \frac{1}{2} \text{sinc}\left(\frac{n}{2}\right) \delta\left(f_x - \frac{n}{L}\right) \quad (3.3)$$

Integrating the above expression around the zeroth diffraction order yields a cosine signal which provides a direct measure of the phase modulation. In our experimental calibration, this signal around the zero order of the GLV Fourier plane is selected by a pinhole and detected by a photodetector as the GLV voltage of is cycled through its full range. A similar measurement around the first order is also made and the zeroth and 1st order diffraction efficiencies are plotted in Fig. 3.9 (a) in blue and red curves respectively.

The simulated cosine curve (blue) differs from the experimental response (black) measured by the photodetector as shown in Fig. 3.9 (b). In order to accurately predict the GLV voltages required to implement different phase values, we perform a least square fit between the simulated and experimental curves in Fig. 3.9. Hence, for each phase value between 0 to 2π we noted the corresponding intensity on the y-axis of the simulated curve and found its closest numerical value in the experimental curve to generate a phase to GLV voltage look-up table. This curve relating the phase to the GLV voltage bits in our experiments is shown in Fig. 3.9 (c).

We note in Fig. 3.9 (b) that the modulation depth is limited to a little over $3\pi/2$. We therefore manually set the first half of the rest of the phase values to the GLV voltage corresponding to the maximum attained phase value and the second half to the zero-phase GLV voltage in Fig. 3.9 (c).

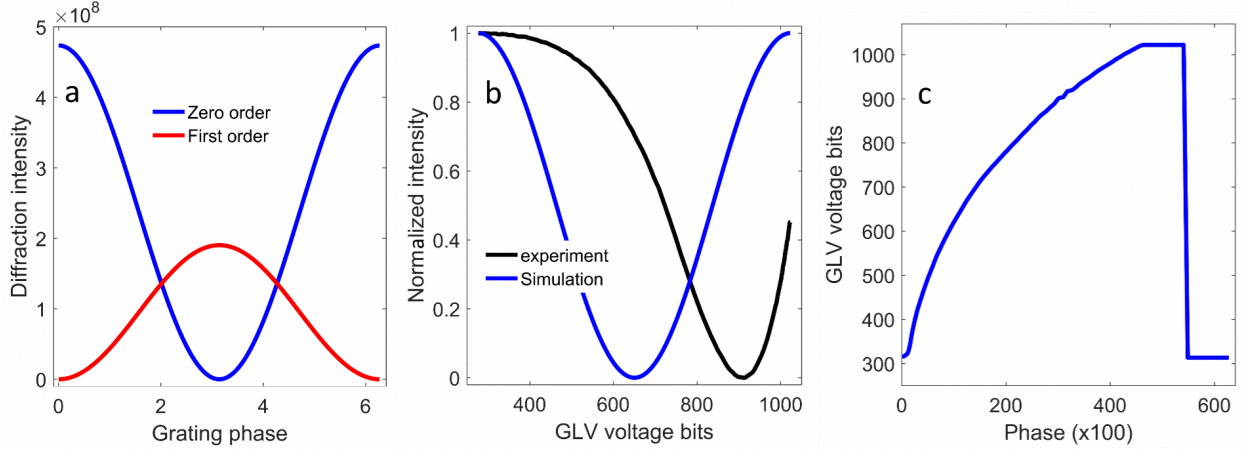


Figure 3.9: Experimental calibration of the GLV phase-to-voltage curve. (a) Simulated diffraction efficiencies of the zeroth and first orders in the GLV Fourier plane in blue and red respectively. (b) Normalized simulated (blue) and experimental (black) diffraction efficiencies of the the zero order of the GLV Fourier plane when a square phase grating with increasing contrast is projected on the GLV. (c) Calibrated look-up table defining the phase value to GLV-voltage transformation to implement phase modulation in the 0 to 2π range. This calibration was performed using a 460 nm laser. Separate calibration procedures were carries out for different wavelength and optical configurations.

3.7.2 Experimental speckle shape and enhancement for different illumination configurations

As described in section 3.2, certain scatterers with memory effect, such as diffusers can give rise to elongated speckle patterns in their far-field when illuminated with anisotropic beams that are more spread in one spatial dimension than the other. In our system, we can eliminate this elongation by choosing the image plane illumination configuration of the GLV where the beam is magnified differently along its two spatial axes, such that it transforms into a square-shaped beam. Here we show a comparison of focal spots produced in the case of both image and Fourier plane illuminations in our experiment to highlight their differences. Interestingly, while the shape of the two focal spots are quite different, their enhancement values are similar. This indicates that memory effect does not limit the number of degrees of freedom on the scatterer.

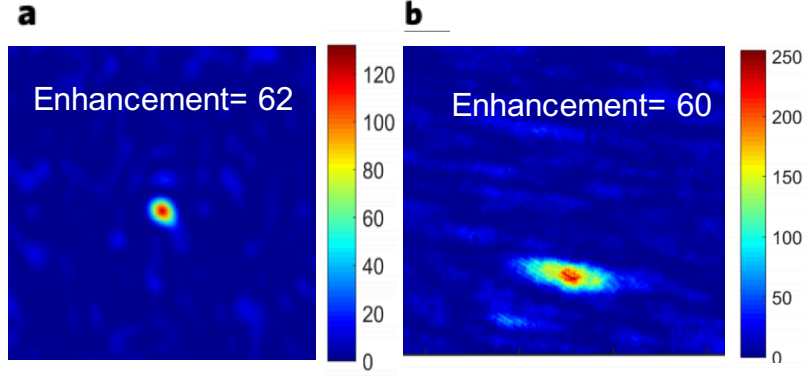


Figure 3.10: Speckle shape and enhancement comparison for focal spots produced using (a) image plane and (b) Fourier plane illumination configurations. The enhancement for the two focal spots are similar despite the different shapes of the speckle grains. The elongation factor measured for the speckle produced by Fourier plane illumination is found to be 2.76, corresponding to a thin diffuser with $\sigma = 2.7$. The experiment with image plane illumination was done using a 532 nm laser, while that with the Fourier plane illumination was done with a 460 nm laser.

3.7.3 Analysis of factors affecting focus enhancement

We performed simulations for focusing through scattering media by accounting for various imperfections in the GLV design using the TM approach and study their effect on the focus enhancement. We simulated 2-D fields and assumed 200 independent GLV pixels, of which 8 were used for a phase stepping reference. The number of Hadamard modes was the same as the number of independent signal pixels, i.e., 192. The resulting enhancement as a function of the number of modes being used for TM measurement is plotted in Fig. 3.11, for a number of effects dependent on the GLV design.

The theoretical enhancement, assuming phase only modulation using N number of independent phase control pixels, is $\pi(N - 1)/4 + 1$ [181]. The blue circles indicate the theoretical enhancement, which matches well with the ideal case where we employ phase-only modulation for TM calibration, but assume complex modulation capability for projecting the optimal wavefront for focusing. The TM approach corresponds to the case where we assume phase-only modulation for focusing as well.

Further, using the TM approach, we simulated four more effects arising due to the particular

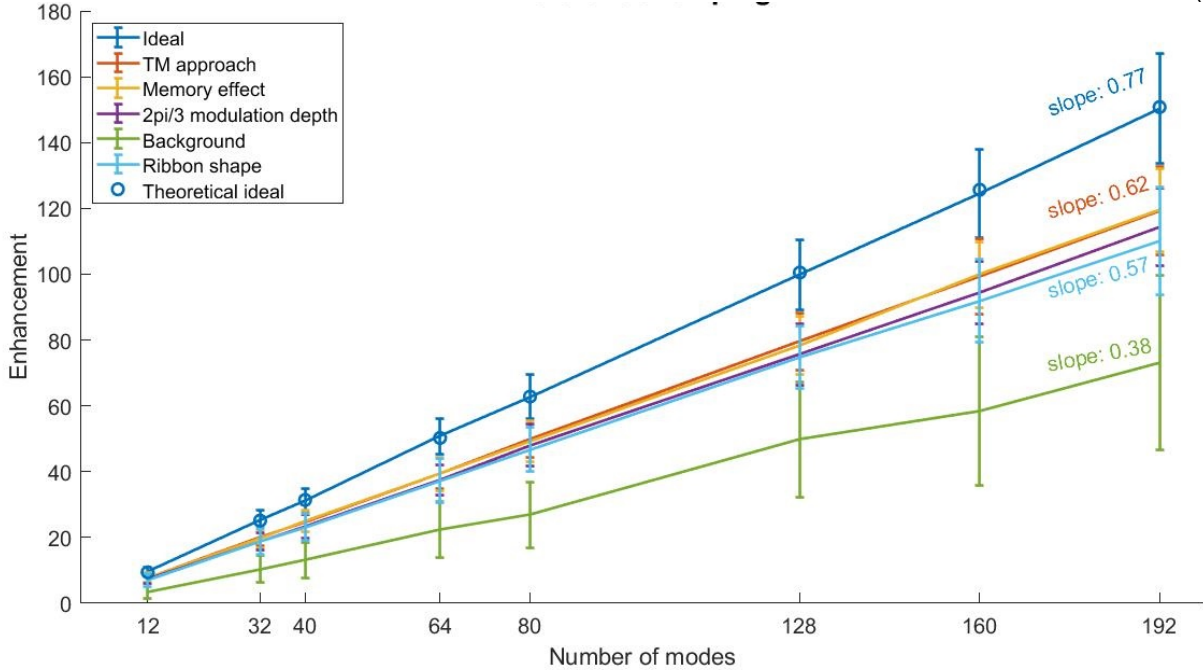


Figure 3.11: Simulation of enhancement as a function of the number of optimized modes for various GLV imperfections. The plots are averaged over 200 different scattering media realizations and the errorbars indicate the standard deviation.

design of the GLV, namely, the memory effect, insufficient modulation depth, modulated background signal and the shape of the GLV ribbons. The memory effect was incorporated using the TM model detailed in section 3.2.1. We employed the Fourier plane illumination in this model to study the effect of speckle elongation on enhancement. We find that the enhancement is unaffected by memory effect. Although against intuition, the shape of the speckle does not affect the intensity of the focus because the intensity scales with the number of phase control pixels, irrespective of their arrangement.

Next we model the effect of incomplete modulation depth of the GLV, resulting from the insufficient stroke size of the ribbons. We found a modulation depth close to $\sim 3\pi/2$ when using the 460 nm laser. To simulate this effect, we set all the phase values in the optimal phase mask for focusing between $3\pi/2$ and $7\pi/4$ to $3\pi/2$ and the remaining phase values between $7\pi/4$ and 2π to 2π . The enhancement curve incorporating this effect is plotted in purple and shows that this effect affects the enhancement only marginally.

We also study the diffraction effects due to a finite pixel pitch of the GLV. Each GLV pixel consists of six ~ 3.75 wide ribbons with ~ 0.5 gaps between each of them. As explained in the discussion section, a high frequency grating can result from a coherent interference of the light reflected from the GLV pixels and from the back-plane behind them. When the pixels are phase-stepped, the diffraction efficiency of this grating varies, leading to a background modulated signal which interferes with the TM mode measurements, especially for the modes with smaller transmission efficiency.

We simulate the background signal as we cycle all the GLV pixels through the full phase modulation range ($0-2\pi$) as illustrated in Fig. 3.12 (a). We numerically calculate the zero order diffraction efficiency as a function of the GLV voltage which is plotted in black in Fig. 3.12 (b). We also show the corresponding zero order intensity measured from our experimental setup, while all the GLV pixels are phase stepped, in black in Fig. 3.12 (c) for a comparison. We assume the GLV pixels-to- back-plane distance to be an equivalent of a π phase shift in the simulation to match the experimental trend. We also show for comparison the first order and zero order diffraction efficiency in red and blue curves respectively in Fig. 3.12 (c). These curves were measured while a high frequency grating with the even pixels fixed to zero phase and the odd pixels increasingly stepped up in phase, were projected on the GLV.

We observe that the experimental background signal has additional features compared to the simulated curve. This is because the true distance between the GLV pixels and its back-plane is unknown and could be different than the equivalent of a π phase shift, as we assumed. Moreover, the oscillations in the experimental curve could be a result of multiple reflections between the two planes due to an angular incidence of light. These complex effects are difficult to model because of too many free parameters. However, their fundamental cause is the interference of light from the pixels and the GLV back plane and we proceed with our simple model for simulating the modulated background signal as described above.

To analyze the effect of the background signal on the focus enhancement, we simulate each pixel using 3 ribbons, of which one is fixed to emulate the GLV back-plane, while the other two

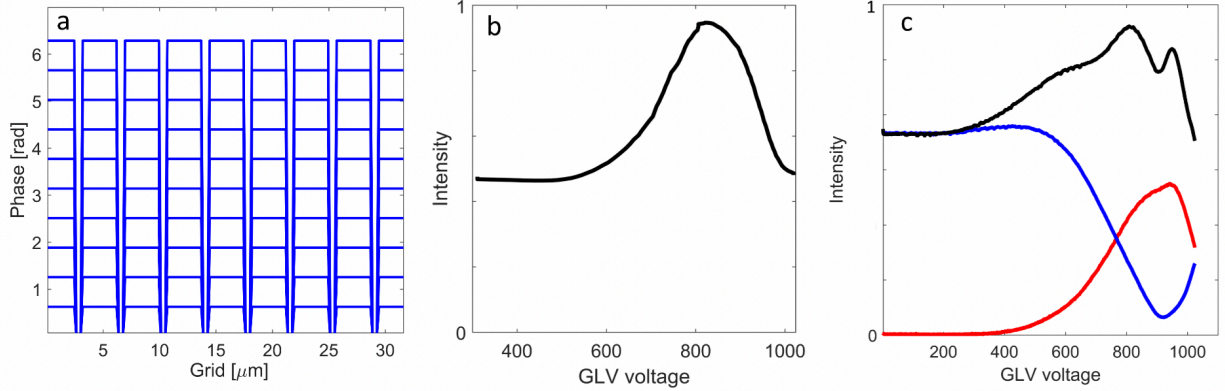


Figure 3.12: Background signal due to inter-pixel gaps in the GLV. (a) Illustration of a GLV grating created when all the pixels are collectively used to project phase values from 0 to 2π . (b). Simulation of the background signal calculated from the zero order diffraction efficiency, as the GLV pixels are cycled between 0 to 2π phase values. (c). Experimental characterization of the background signal (black and the zero and first order diffraction efficiency when a high-frequency grating with even pixels fixed to zero phase and odd pixels modulated between 0 to 2π are projected on the GLV

can phase step according to the applied voltage. The light green curve in Fig. 3.11 shows the enhancement trend in the presence of a background signal. We find a significant drop of 40% in the enhancement, which shows that the background signal can affect the enhancement strongly.

Finally, we investigate the effect of non-uniform bending of the ribbons of the GLV. The phase modulation mechanism of the GLV involves ribbons suspended above a substrate, on which a voltage is applied to bend the ribbons towards the back-surface. Since the ribbons are many times longer than wider, the bending geometry of the ribbons can be non-uniform. We investigated this issue by placing a detector in the magnified image plane of the GLV and translating it across the length of the ribbons. The image of the GLV shows horizontal stripes, since we stretch out the GLV line into a square shape, as explained earlier. We plot the diffraction efficiency curves measured by the photodetector in Fig. 3.13 at two locations a and b in blue and red respectively. The locations a and b are as indicated in the inset of Fig. 3.13.

We observe that the modulation depth at b is slightly reduced. This effect can be minimized by forming a tight focus on the ribbons. The length of the ribbons is 220 and we calculated the width of the incident Gaussian beam in the GLV plane to be only 10 , hence ensuring that this

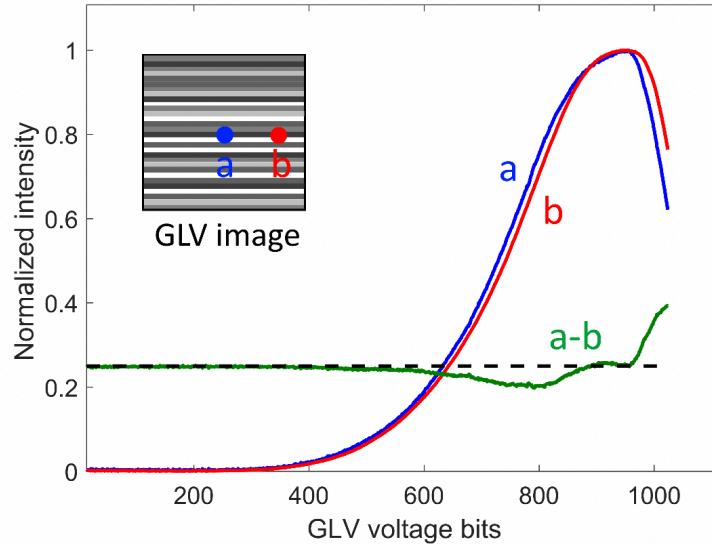


Figure 3.13: First order diffraction efficiency for different horizontal locations (a and b) of the GLV pixel array. The red and blue curves correspond to the first order diffraction efficiency measured by a photodetector placed at two locations (a) and (b) respectively in the image plane of the GLV. The difference of the two curves, (a-b) is shown by the green curve and demonstrates that the modulation depth can vary along the length of the pixels due to their non-uniform bending. The inset shows a cropped region in the GLV image plane and marks the locations (a) and (b) where the photodetector was placed.

effect remains small.

We modelled this effect by assuming that 2 of the three ribbons in our GLV simulation produce the desired phase shift, while the third one produces a phase shift only $7/8^{\text{th}}$ of the desired phase shift, hence introducing a small phase error. The particular fraction was chosen based on the experimental observation shown in Fig. 3.13. The enhancement curve representing this effect is shown in light blue in Fig. 3.8. We find a decrease in enhancement of 7.7%, which is much smaller compared to the effect of the background signal. Hence, the background signal is found to be the most prominent factors affecting the focus enhancement.

Chapter 4

Tunable mode control through multimode fibers

4.1 Introduction

Multimode fibers (MMFs) have found application in classical [67, 173, 90, 92] and quantum communication [94], high dimensional quantum key establishment [7, 124, 121], transport of spatially entangled qubits [115], conservation of orbital angular momentum [81], sensing [15, 114, 159], energy delivery [97, 125, 1], computation [49, 109], phase conjugation [138, 169, 79, 189] and imaging [139, 123, 40]. Particularly interesting is the recent demonstration of ultrathin imaging endoscopes via wavefront shaping control to compensate for the effects of dispersion and mode coupling [133, 177, 33].

All these applications are enabled by some form of control over the modes of the fiber. Recently, spatial light modulators (SLMs) have been used for controlling all the modes in the fiber mode basis of typical multimode fibers with $\sim > 200$ modes [34, 35, ?]. However the method requires precise alignment, polarization control, and a number of SLM pixels much greater than the number of modes in the fiber. On the other hand, large-core MMFs with thousands of modes, which we refer to as myriad-mode fibers (MyF) here, are better suited for imaging due to their efficient light collection and high-resolution imaging capability. Mode control in MyFs remains a major challenge due to the large number of degrees of freedom and the detrimental effects of inter-modal and polarization coupling [178].

Specifically, in the field of fiber-optic communication, MMFs hold significant interest due to their large information carrying capacity. The achievable data rates through MMF transmission

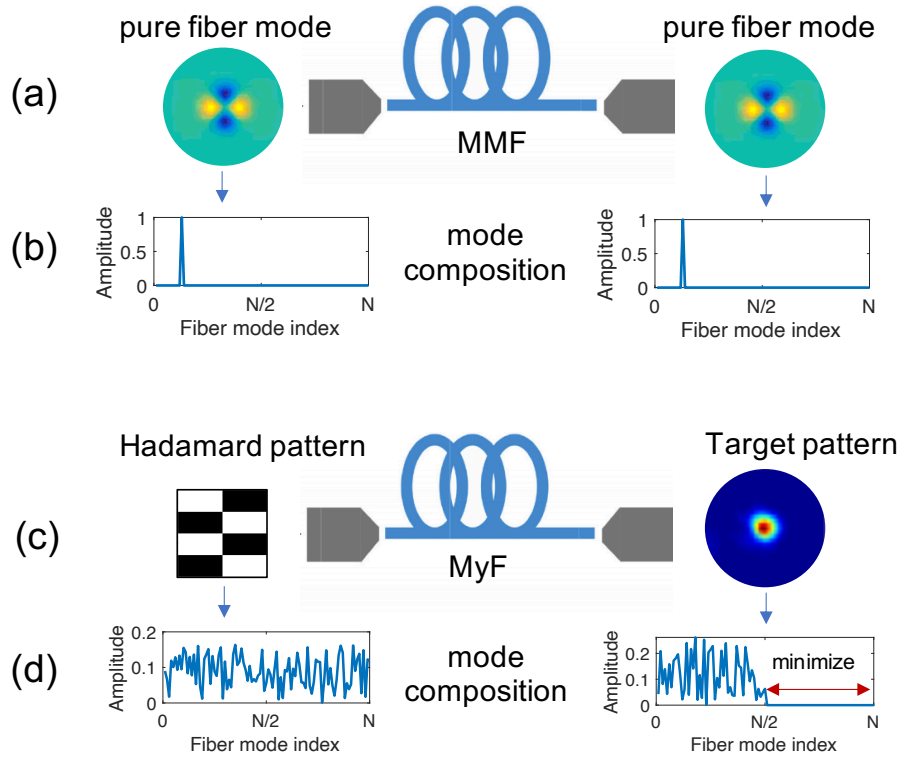


Figure 4.1: Illustration of methods for mode control in the fiber mode basis. (a) Mode control via excitation and generation of pure fiber modes. (b) Fiber mode composition of the input and output fields in (a). Since individual pure modes are excited and detected, their corresponding mode compositions are identical delta functions. (c) Proposed method for mode control in the fiber mode basis via excitation of Hadamard functions and detection of focal spots. (d) Fiber mode composition of the input and output fields in (c). Since Hadamard functions and focal spots are complex combinations of the individual fiber modes, their mode compositions are distinct complex signals. By performing a change of basis we can select the fiber modes that we control at the output and minimize the other mode coefficients. Here, as an example we minimize the second half higher order mode coefficients in order to generate a target output pattern using only the first half lower order modes.

systems however are still severely limited by modal dispersion, coupling and nonlinearities. Mode division multiplexing is a promising technique which allows using different modes of the MMF as separate information channels to enhance the fiber capacity. It has been demonstrated by offset launching [147], using phase plates or gratings [157, 62], photonic crystal fibers [144] or multicore fibers [192] by phase and amplitude modulation using spatial light modulators [36, 155] and multi-plane light conversion devices [?]. These techniques aim for precise control of individual fiber modes and are hence not easily scalable to MMFs supporting thousands of modes.

In this report, we present a method to select specific groups of fiber modes at the output of an MyF using a phase-only spatial light modulator at its input. As an application example, the selected modes are constructively interfered at a predefined location in the fiber output, hence forming a focal spot. While we use the Hadamard basis at the input and generate focal spots at the output, we achieve mode control in the fiber mode basis via a digitally implemented basis transformation. Figure 4.1 illustrates the difference in methodology between the currently used techniques for fiber mode control through multimode fibers and our technique for fiber mode control through myriad mode fibers.

As a result, one can take advantage of the different properties of mode groups and their interactions. The fiber mode composition of the focal spot can be tuned by modifying the input pattern. Furthermore, we perform experiments to compare the sensitivity of focal spots to fiber bending when created using two different complementary mode sets. Towards a quantitative evaluation of the quality of mode control, we define specific efficiency and fidelity metrics that help understand the possibilities and limitations of mode control.

4.2 Mode control in the fiber mode basis

Wavefront shaping is becoming a key technique in imaging and energy delivery through scattering media and MMFs. One of the preferred approaches involves characterization of the medium, in our case the fiber, through the transmission matrix (TM) [145, 34]. The measured TM, can be used to generate target field distributions at the fiber distal end such as focal spots. Here, we employ the phase-shifting interferometric approach for TM calibration using an internal reference frame [145, 32] and recover the output field using three intensity measurements. The calibration method is detailed in SI section 1.

Let us consider the problem of generating a physically feasible output field, E_{target} , at the distal end of the fiber. E_{target} can be written as a superposition of all the fiber modes. Assuming a radially symmetric parabolic refractive index profile, the linearly polarized (LP) modes of a GRIN (graded-index) MyF can be represented using the Laguerre-Gauss (LG) field solutions [18, 85]. We

note that the actual modes of the fiber will deviate from the LG mode profiles, depending on the true refractive index profile, imperfections and bend configuration of the fiber. Notwithstanding, to demonstrate the method here, we implement mode control in the LG mode basis as they are a very good approximation of the actual modes.

For an MyF with N_m number of modes per polarization, stored in the columns of a matrix, F , which we call the mode matrix, we can represent an N_{out} - pixel E_{target} field in the modal basis by taking its product with the inverse of the F matrix. However, F can only be invertible when it is a square matrix, which is true only when the number of samples in E_{target} is equal to the number of fiber modes. In the experiments described below, we over-sample each speckle grain appearing at the output to maintain a good SNR, which leads to a highly rectangular and non-invertible F matrix. Hence, for the general case, we find the modal representation of E_{target} using the Moore-Penrose pseudo-inverse of F , F^+ as described in Eq. 4.1.

$$M_{target} = F^+ E_{target} \quad (4.1)$$

Here, M_{target} is an $N_m \times 1$ vector of mode coefficients corresponding to the vectorized 2D field E_{target} , F is the $N_{out} \times N_m$ mode matrix and F^+ denotes its pseudo-inverse. In order to tune the mode composition of the target field, we find the orthogonal projection of E_{target} , E'_{target} onto a selected subset of $N'_m < N_m$ modes stored in an $N_{out} \times N'_m$ mode matrix, F' as shown in Eq. 4.2.

$$E'_{target} = F' F'^+ E_{target} \quad (4.2)$$

where F'^+ denotes the pseudoinverse of F' defined as $F'^+ = (F'^\dagger F')^{-1} F'^\dagger$ and \dagger denotes the conjugate transpose. In physical terms, E'_{target} is the closest output field (least norm solution of the least squares problem) to E_{target} that can be generated with the selected Nm' modes.

The measured complex-valued TM of the fiber, K_{obs} is then used to generate the mode tailored field E'_{target} at the fiber distal end by projecting an optimal phase mask on the fiber proximal end, E_{in} calculated using Eq. 4.6.

$$E_{in} = K_{obs}^\dagger E'_{target} \quad (4.3)$$

Fig. 4.2 depicts the entire process with all the columns reshaped to 2D only for visualization.

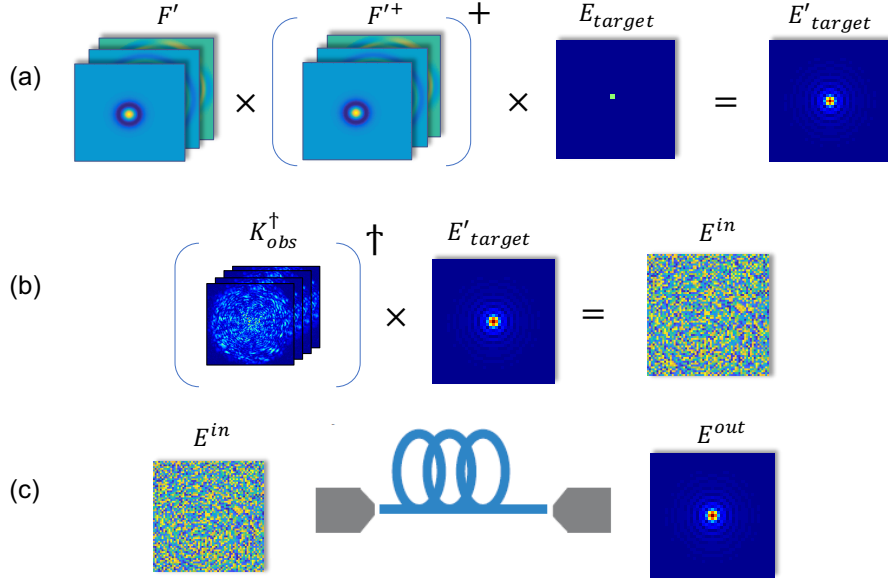


Figure 4.2: Illustration of mode control for focusing through a fiber using its transmission matrix. (a) The projection of the target field onto the selected mode subset yields its mode-tailored approximation, E'_{target} . (b) The optimal input phase mask, E^{in} required to produce the target field at the fiber distal end is found using the conjugate transpose of the transmission matrix. (c) The optimal mask is projected on the fiber proximal end, to produce the output field $E_{out} = E'_{target}$ after propagation through the fiber. The space dimension in all variables is extended from 1D to 2D for visualization.

We define two metrics to evaluate the mode control performance at the output fields, efficiency and fidelity. The efficiency, denoted by η , is defined as the ratio of total energy in the selected fiber modes and the sum total energy in all the modes as shown in Eq. 4.7.

$$\eta(E_{out}) = \frac{\|E'_{out}\|^2}{\|E'_{out}\|^2 + \|E''_{out}\|^2} \quad (4.4)$$

In the equation above, the single and double primes denote the selected and non-selected mode components of the experimental output field E_{out} , which were calculated by back-projecting the output field, E_{out} on the fiber modes basis, as before, by multiplying it with $F'F'^+$ and $F''F''^+$ respectively. The fidelity on the other hand, denoted by C , is defined as the Pearson correlation

coefficient between the target and experimentally obtained intensities as defined in Eq. 4.5.

$$C(I_{out}, I_{target}) = \frac{COV(I_{out}, I_{target})}{\sigma_{I_{out}} \sigma_{I_{target}}} \quad (4.5)$$

Here, COV denotes the covariance function and σ denoted the standard deviation of the variable in the subscript. While the efficiency characterizes the confinement of energy in the selected modes, the fidelity characterizes the spatial control ability.

4.3 Experimental setup

The experimental setup used in our experiments is illustrated in Fig. 4.3. It consists of a 532 nm, CW laser and a DMD that can be used for phase modulation of the incident beam using computer-generated holography [32].

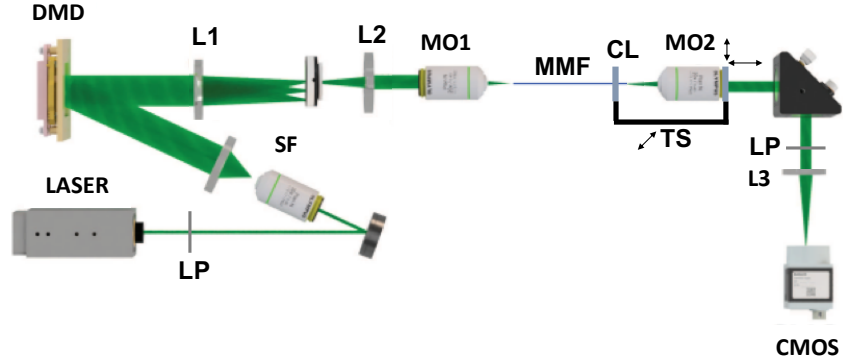


Figure 4.3: Experimental setup for mode control and focusing through an MyF. L1, L2, L3: lenses, MO1, MO2: Microscope objectives for coupling light in and out of the fiber, LP: Linear polarizer. SF: Spatial Filter, CL: Clamp to hold to fiber distal end, TS: 1D translation stage used for bending the fiber, CMOS: Camera to measure the distal end intensity.

Because the DMD provides only binary-amplitude modulation, the effective number of phase pixels (4096 in our case) is significantly lower than the number of binary pixels (262144). A microscope objective couples the Fourier transform of the modulated wavefront into the MyF and another microscope objective and lens L3 are used to image the MyF distal tip onto a CMOS camera. We use a ~ 40 cm long graded index MyF with a diameter of $100 \mu\text{m}$ (Newport F-MLD)

for all experiments. We place a linear polarizer at the distal tip to limit the TM measurement to a single polarization. In the absence of polarization coupling, this would mean that the 4096 independent phase pixels of the DMD control 3570 single polarization modes of the MyF. However graded index fibers show significant polarization coupling [166] which leads to loss of some light to the unoptimized orthogonal polarization and in turn reduces the focus enhancement, defined as the ratio of the peak focal intensity and the average output intensity. In any case, extension of the approach to two polarizations in the TM is relatively straightforward [176, 47].

Different sets of basis functions can be chosen to measure the TM, including canonical plane waves or focal spots at the input facet of the fiber. For this study, we chose the Hadamard phase basis because of its ease of implementation with the DMD. The calibration required 12288 measurements which were made in about three minutes. The calculation of the pseudoinverse of the mode matrix has a complexity of $O(N_{in}N_{out}^2)$ and is made in advance to determine the mode selected E'_{target} fields. After calibration, we used the TM to generate phase conjugated focal spots at the output. We choose focal spots because of their importance in imaging. In addition, they are easily generated using the conjugate transpose approximation of the inverse of the TM. Generation of more complex patterns is also possible, although it requires a regularized TM inversion which is computationally more demanding [146]. The optimal phase masks to project each focal spot are determined using Eq. 4.6 with a computational complexity of $O(N_{in}N_{out})$. Each generated focal spot fields, E_{out} was measured using three phase measurements, just as done during calibration and their corresponding mode coefficient vectors, M_{out} are determined using Eq. 4.1, but for E_{out} instead of E_{target} .

4.4 Results

To demonstrate mode tunability, we created focal spots using two subsets of modes in the mode group-ordered mode matrix F . A first set of scanning spots was created with the half lowest order modes (LOMs) in F and the second set of spots was created using the half highest order modes (HOMs). Figure 4.4 illustrates two examples of focal spots, one using each of the above two

mode sets. Figure 4.4 (a-d) show the absolute value of the target and experimental output fields, E'_{target} and E_{out} for the two focal spots and figure 4.4 (e,f) show their corresponding targeted and experimental mode compositions, M'_{target} and M_{out} . We can observe that while the mode coefficients of the non-selected modes cannot be completely suppressed in the experiment, the mode coefficients of the selected modes are in good agreement with their targeted values.

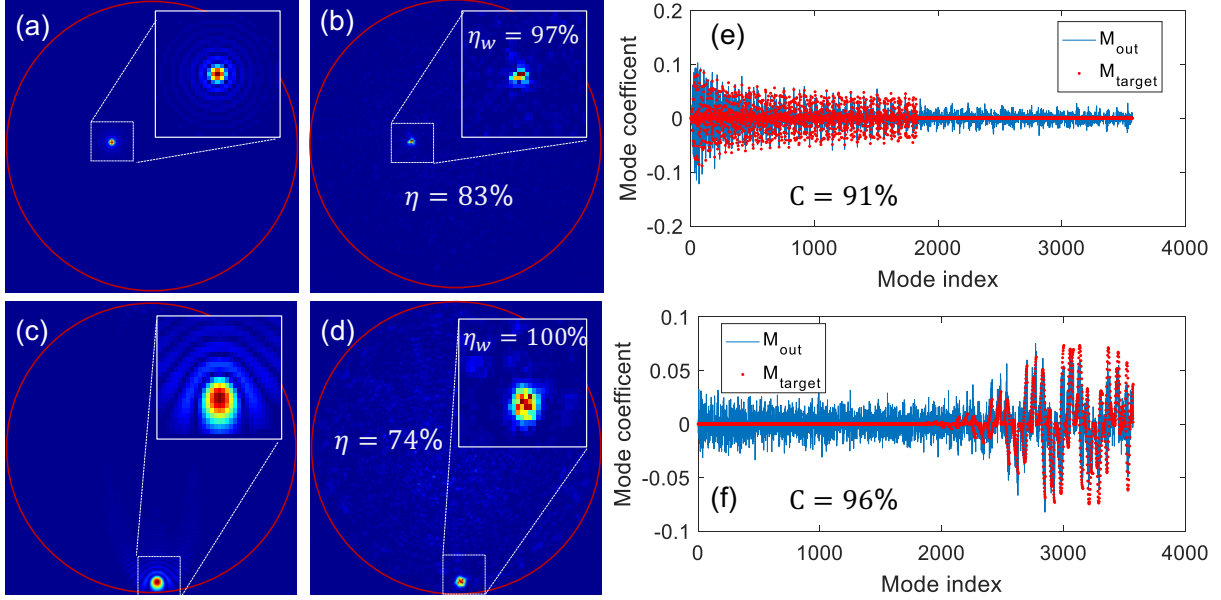


Figure 4.4: Experimental demonstration of focusing with mode control. (a,b) Absolute value of the expected and experimental electric fields respectively when focusing using LOMs. (c,d) Absolute value of the expected and experimental electric fields respectively, when focusing using HOMs. (e) Modal composition of fields in (a) and (b). (f) Modal composition of fields in (c) and (d). Insets display a zoom-in on the focus profile. Experimental efficiencies of full fields, η , and of cropped windows, η_w , are indicated in respective figures and the fidelities, C , are indicated within their mode coefficient plots.

The high efficiency and fidelity values obtained for the focal spots generated with selected modes are indicated in Fig. 4.4. We also analyzed a circular window of radius 8 pixel wide around the focal spot for both fields and the corresponding efficiency values are shown in the top-right zoom-in insets. The increase in efficiency indicates that although some energy remains in the unselected modes within the full field, the focal spot is primarily a result of the interaction of the selected modes.

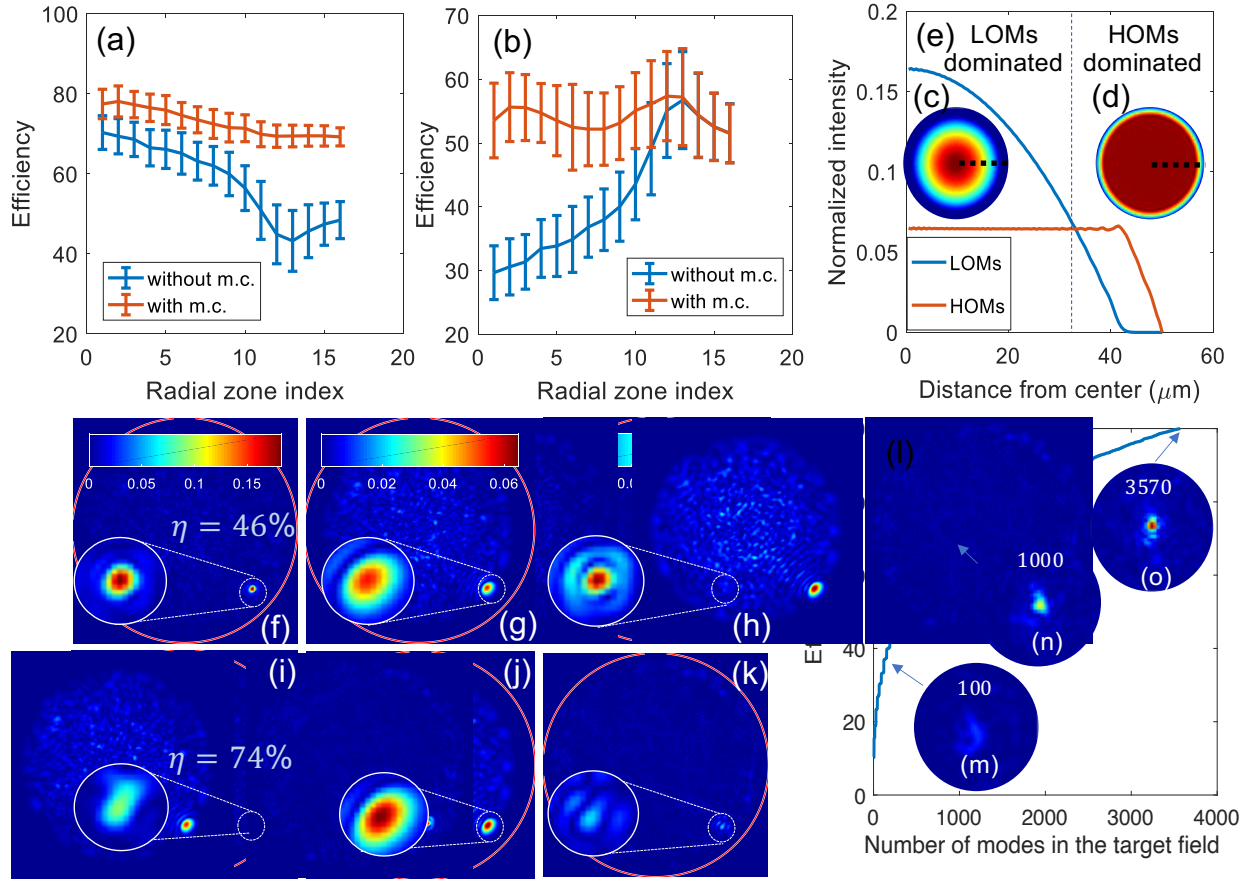


Figure 4.5: Statistics of mode control through MyFs as a function of radial location of the focal spots and the number of modes selected for optimization. All sub-figures show data simulated using the experimentally measured TM. (a,b) Average efficiency with standard deviation errorbars of focal spots as a function of their radial location (1965 focal spots). The focal spots are evenly spaced across the entire fiber cross section and split into 16 radial zones for the plot. We define radial zones as equal area annuli/circle with increasing inner and outer radii. The number of focal spots in each radial zone is 121 ± 7 . (a) Comparison of LOM efficiencies for focal spots created with mode control using only LOMs (red curve) and without mode control or using all the fiber modes (blue curve). (b) Comparison of HOM efficiencies for focal spots created with mode control using only HOMs (red curve) and without mode control or using all the fiber modes (blue curve). (c, d) Net radial intensity profile of (c) LOMs and (d) HOMs mode sets. (e) Cross section of the LOMs and HOMs profiles corresponding to the thick dotted lines marked in (c) and (d). A thin dotted line divides the fiber cross section into “LOMs dominated” and “HOMs dominated” regions, depending on which mode set has a higher intensity profile in the region. (f-k) Example of a digitally computed focal spot (f,i) and their corresponding LOMs (g,j) and HOMs (h,k) components created using all the fiber modes or without mode control (f-h) and using LOMs or with mode control(i-k). (f) Digitally computed focal spot created without mode control. (g) LOMs component of the focal spot field in (f) computed by back projecting the field on the fiber mode basis as described in the main text. (h) HOMs component of the focal spot field in (f). (i) Focal spot field at the same location as in (f) but digitally computed using only LOMs outside its optimal region. (j) LOMs component of focal spot field in (i). (k) HOMs component of focal spot field in (i). The proportion of energy in the LOMs in the spot fields shown in (f) and (i) are indicated inside the figures. (l) Efficiency of the focal spot shown in Fig. 4.4 (b), digitally computed using, different number of mode coefficients from its full mode coefficient set, M_{target} . (m-o) Zoom-ins of the evolving focal spot when 100, 1000 and all the 3570 modes are considered in the target field.

Interestingly, when focusing in the near field of the distal end of the fiber, the mode efficiency varies with the radial location of the focal spot when a given HOM or LOM set is selected. This is because different modes have different spatial support and are more or less suitable for the target output. To demonstrate this, we show plots of efficiency of mode-controlled focal spots created at increasing distance from the center of the fiber using LOMs and HOMs respectively [Fig. 4.5 (a) and (b) (red curves)]. The plots represent the statistics of 1965 focal spots spread evenly across the fiber cross section. All focal spot fields are digitally computed using the experimentally measured TM and the optimal phase mask calculated in Eq. 4.6. We observe that when focusing with LOMs, the efficiency decreases away from the center of the fiber and flattens at the boundary, while for the HOMs, the efficiency decreases between radial zones 5 - 10, increases near the boundary and then decreases again. Both these trends roughly follow the net intensity profiles of the LOMs and HOMs mode sets respectively, which are shown in the circular insets of Fig. 4.5 (e) [Fig. 4.5 (c) and (d)]. The intensity profiles are calculated as the sum total intensity of all the modes in a mode set. The cross sections of the intensity profiles of the two mode sets are plotted in Fig. 4.5 (e) and show that the LOMs dominate the central fiber region and do not extend all the way to the boundary, where the HOMs start to dominate. Hence, focusing in the central region is optimal for mode control using LOMs, while focusing in the outer boundary region is better done with HOMs. Even without mode control, these choices intrinsically yield the highest efficiency values.

To compare the optimized mode compositions of focal spots with their corresponding intrinsic ones, we also show in Fig. 4.5 (a) and (b), the efficiency of LOMs and HOMs respectively for the focal spots created without mode control or using all the fiber mode (blue curves). When we do not employ mode control, we calculate the efficiency as the intrinsic proportion of energy in the particular mode subsets chosen in Fig. 4.5 (a) and (b). It can be noted that even as the focus moves away from the regions where the selected mode sets dominate, which we refer to as their corresponding optimal regions, mode control enables creating focal spots with up to 66% and 73% more energy in the selected modes. The only exception is observed at the boundary of the fiber when HOMs are selected. For this special case, the mode control makes no difference in the

efficiency, which makes sense since LOMs do not extend till the fiber boundary and hence cannot contribute to focal spots at the boundary.

In general, although the efficiency and fidelity values can be lower outside the optimal region of mode sets, the proportion of energy in the selected modes improves significantly due to mode control. To visualize this improvement, we show the digitally computed output fields and their LOM and HOM components for a focal spot created without and with mode control i.e., using all the fiber modes and using LOMs [Fig. 4.5 (f-h) and (i-k) respectively]. Mathematically, the output fields, E_{out} [5 (f) and (i)] were computed as the product of the input fields E_{in} found in Eq. 3 with K_{obs} . The E'_{target} used to calculate the input fields were calculated using all the fiber modes i.e., $E'_{target} = E_{target}$ for 5 (f) (without mode control) and using Eq. 4.2 with F' containing only LOMs for 5 (i) (with mode control). The LOMs and HOMs mode components of each of the above output fields [5(g,h) and 5(j,k)] were found by back-projecting the output fields, E_{out} on the fiber modes basis by multiplying them with $F'F'^+$, where F' is the fiber mode matrix with the LOMs or HOMs in its columns. The HOMs component is non-zero even when LOMs are chosen to create the spot field because the mode control efficiency is not 100 %.

The particular spot shown is created near, but not quite at the fiber boundary. We find that even for LOM selection, mode control allows improving the proportion of LOM energy from 46% to 74% and suppresses the energy in the HOMs. Furthermore, the contribution from LOMs to the focal spot alone is also enhanced from 28% to 78%, while the contribution from HOMs is diminished to 22%. It should be noted, that although mode control succeeds in putting more energy in LOMs even when the focal spot is created outside their optimal regions, the enhancement decreases. This is explained by the fact that the non-selected HOMs, which dominate the region, no longer participate in forming the focal spot when mode control is employed. Appendix B, Fig. 4.7 shows experimental examples of two focal spot fields, and their corresponding mode coefficients, created outside their optimal regions.

Another interesting aspect of this method is that it is more efficient in generating mode-controlled fields that involve interaction of many modes rather than few modes or just a pure

mode. This can be explained by the fact that as the number of modes interacting in the target field increases, the higher the number of optimized modes is and the weaker the unoptimized speckle background becomes. Fig. 4.5(1) illustrates this phenomenon. Each data point represents a unique mode control optimization and as the number of modes in the target field increases, we observe an increase in the efficiency of the mode-controlled output field. The output fields at all points are digitally computed from the TM and the target field as before. For this plot, we chose the mode coefficients of the focal spot shown in Fig. 4.4 b, and performed different optimizations using its 1st, 1st and 2nd, 1st 2nd and 3rd, and so on with the following cumulative mode coefficients. We normalized all the target fields by their Euclidean norm for calculating the efficiency. The insets in the plot in Fig. 4.5 (1) labelled 4.5 (m-o) show zoom-ins of the evolving output focal spot when the first 100, 1000 and all the 3570 mode coefficients respectively are considered in the target field. We can observe that as more modes are selected, the unoptimized background due to the unselected modes decreases, leading to better efficiency as well as focus enhancement.

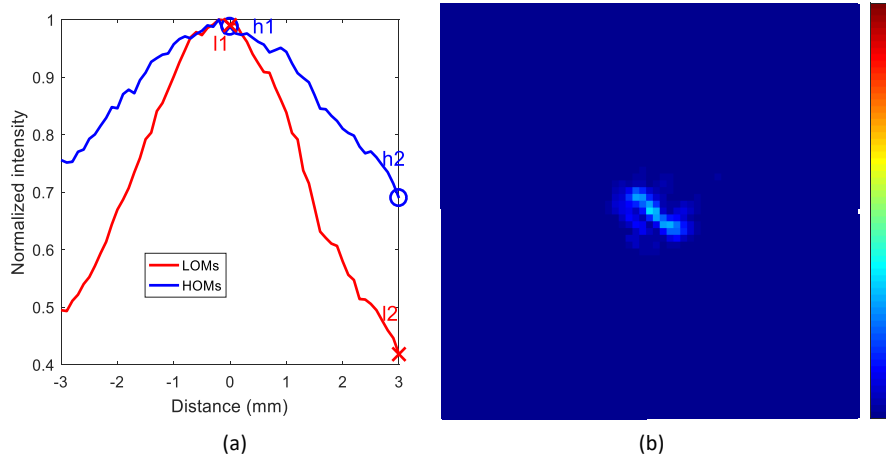


Figure 4.6: Experimental demonstration of bending resilience of focal spots created using different mode sets. (a) Plot of normalized peak focal intensity of 200 near-axis focal spots created using LOMs (red) and 200 near-boundary focal spots created using HOMs (blue) with translation of the fiber distal tip. (b) Evolution of example focal spots l1 and h1 created using LOMs and HOMs respectively at the initial fiber position into l2 and h2 after a 3mm translation of the distal tip. The positions of the spots are marked in (a).

Finally, using inferences from Fig. 4.5 about the mode efficiencies of focal spots at various

locations, we studied the robustness of different mode-controlled focal spots to fiber bending. Towards this end, we generated 200 focal spots, each using either LOMs or HOMs in their optimal regions (near fiber axis and at the boundary respectively). To test the robustness, we mount together the fiber clamp, CL and the objective MO1 shown in Fig. 4.3 on a translation stage in order to introduce controlled movements to the fiber distal tip along the horizontal axis. The intensities of the focal spots are recorded in displacement steps of $100\ \mu\text{m}$, upto 3 mm. Fig. 5.8 (a) shows the change in the peak intensity averaged over 200 focal spots with translation and Fig. 5.8(b) shows the evolution of two example focal spots from each of the two mode sets over the motion range. It can be observed that the spots formed with HOMs retain a 30% higher focal intensity than those formed with LOMs after a translation of 3 mm. This indicates that focal spots created using HOMs in the boundary are more robust under these experimental perturbations. This improved robustness could be a result of reduced intermodal coupling and the better stability of high orbital angular momentum modes [81, 65, 64]. Interestingly, the insight from Fig. 4.5 (a-e) about the lack of participation of LOMs in focal spots created at the fiber boundary supports this explanation.

4.5 Discussion and conclusion

We have demonstrated a method to select the mode composition at the output of a myriad-mode fiber (MyF). While we create focal spots at the fiber output, the technique can be extended to generate any desired complex output fields within the limits of the physical mode content of the fiber. We have shown that mode selection with considerable accuracy is possible when the focal spot is created at a proper output position in the fiber cross-section. A key aspect in our experiments is that the number of independent fiber modes per polarization was comparable to the number of controllable phase pixels (87%) unlike in prior SLM-based mode control methods that use thousands of pixels for fibers with relatively fewer modes.

The efficiency and fidelity figures demonstrated here could be improved, for example, by enabling simultaneous amplitude and phase modulation, including full polarization control, and by employing adaptive alignment techniques to enhance mode overlap and coupling efficiency [34, 37].

Furthermore, we did not take any special measures for thermal or mechanical stabilization in our experiment, so our results could be affected by any perturbations to the fiber after the TM calibration. Moreover, we used a 40 cm long fiber prone to misalignment, bends and intermodal and polarization coupling. Using shorter fibers can greatly reduce the magnitude of all these effects and lead to closer to LG-like mode profiles [142]. Additionally, while the LG modes are a good model for graded index fiber, it is well known that commercial fibers have less than perfect index profiles. More precise estimates of the true modes can be attained by a singular value decomposition of the fiber's TM or using other mode characterization techniques [37, 142, 171]. Mode control performance is also limited by imperfections arising from the wavefront shaper. Phase errors can occur from the imperfect phase encoding of the binary amplitude holograms employed for phase modulation with the DMD. Another source of phase error is the 8-level discretization of the phase patterns projected on the DMD. The coupling efficiency of the phase pattern projected from the DMD into the fiber is also a critical factor in mode controllability. For instance, the coupling efficiency of the higher order Hadamard modes to the fiber is poor and can restrict the controllable fiber modes, suggesting other bases might provide even better performance.

As opposed to prior work, efficient mode control in MyF is much more challenging due to the limited number of degrees of freedom provided by the DMD and the inherent complexity of the system. However, the approach ensures that maximum energy is confined to the selected modes at the output and although all the fiber modes still propagate to the distal end of the fiber, the focal spot itself, which is many times brighter than the background, is primarily a result of the interaction of the selected modes. It should also be emphasized, that the technique controls the mode composition at the output of the fiber, which is not necessarily the same as the mode composition throughout propagation due to mode coupling resulting from perturbations of the fiber (bending, imperfections, etc). Because the mode composition throughout the fiber is complex, our technique is more suitable for generating complex mode combinations rather than a combination of fewer modes or a pure mode, unlike other traditional mode control techniques.

The proposed method also provides an avenue for combining the advantage of large core MyFs

for a larger bandwidth, higher NA and bigger field of view, with the bend resilience of an MMF with fewer modes. The extent of intermodal coupling or bend sensitivity of an MMF is inversely proportional to the difference between the propagation constants of the modes [134]. Hence, a fiber of a given NA with a small number of modes exhibits better resilience to bending than one with a larger number of modes. By only selecting a subset of modes while shaping the output wavefront of an MyF, we can ensure reduced intermodal coupling and hence improve the fiber's robustness. Here, we performed an experiment to observe the bend resilience of different mode sets and found that focal spots created using HOMs in the boundary of the fiber show improved resilience. Interestingly, better robustness of HOMs, high frequency speckles composed of HOMs, and/or near-boundary spots has also been reported in other types of robustness experiments with MMFs involving translation of s-bends [119] or bending the central part of the MMF [40, 82, 58]. Although we observed better robustness only in the boundary, we can generate arbitrary fields in the far field of the fiber using these bend resilient modes to achieve better robustness overall [165]. These insights could prove helpful in controlling the bend resilience of an MyF for both imaging and communication applications.

The idea of mode selection through few-mode MMFs is already a topic of wide interest in the field of fiber-optic communication. Mode selection in MyF combined with MIMO processing, could allow the use of groups of modes with similar dispersion and delay profiles as different channels, where the number of channels can be much smaller than the total number of modes in the fiber. Other possible applications of mode selection in MyF include control of individual mode groups for spatio-temporal focusing, quantum communication, and energy delivery.

4.6 Appendix

4.6.1 Focusing with mode control outside the optimal region of a mode set

As shown in Fig. 4 of the main text, if we create a mode controlled focal spot in the non-optimal region of the selected mode set (HOM or LOM), we can direct significant energy from the

dominant modes in the region to the non-dominant selected modes. We have defined the optimal region for a mode set as the spatial region where the selected mode set contains more net energy relative to its complementary mode set and vice versa for the non-optimal region. Here we show the experimental version of the digitally computed focal spot shown in Fig. 4 (i), where we focus near the fiber boundary using lower order modes (LOMs) [Fig. 4.7 (a, b)]. We also show a second focal spot created near the fiber center using HOMs in Fig. 4.7 (c, d). The corresponding target and experimental mode coefficients are also shown in Fig. 4.7 (e, f). We observe that the efficiencies and fidelities are lower for these examples, however the proportion of energy in the selected modes due to the mode control optimization is still significant.

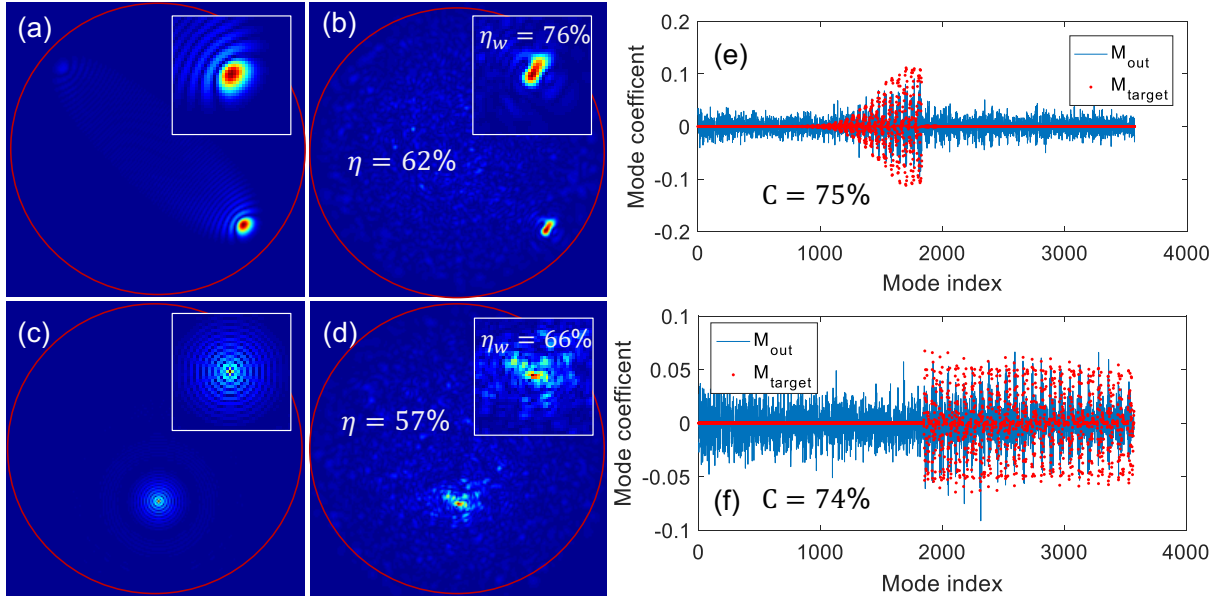


Figure 4.7: Experimental demonstration of focusing with mode control outside the optimal regions of the respective mode sets. (a,b) Absolute value of the expected and experimental fields respectively when focusing using LOMs. (c,d) Absolute value of the expected and experimental fields respectively, when focusing using HOMs. (e) Modal composition of fields in (a) and (b). (f) Modal composition of fields in (c) and (d). Insets display a zoom-in on the focus profile. Experimental efficiencies of full fields, η , and of cropped windows, η_w , are indicated in respective figures and the fidelities are indicated along with their mode coefficient plots.

4.6.2 Comparison of efficiency statistics of experimental and digitally computed mode-controlled output fields

Here we compare the mode control efficiencies of experimentally generated focal spots with those computed digitally using the measured TM. The efficiency plots when focusing using LOMs and HOMs are shown in Fig. 4.8 (a) and (b) respectively. We observe that the trend of the two curves matches quite well. The experimental values are in general lower, most likely due to measurement noise, perturbations to the fiber and phase errors from the DMD.

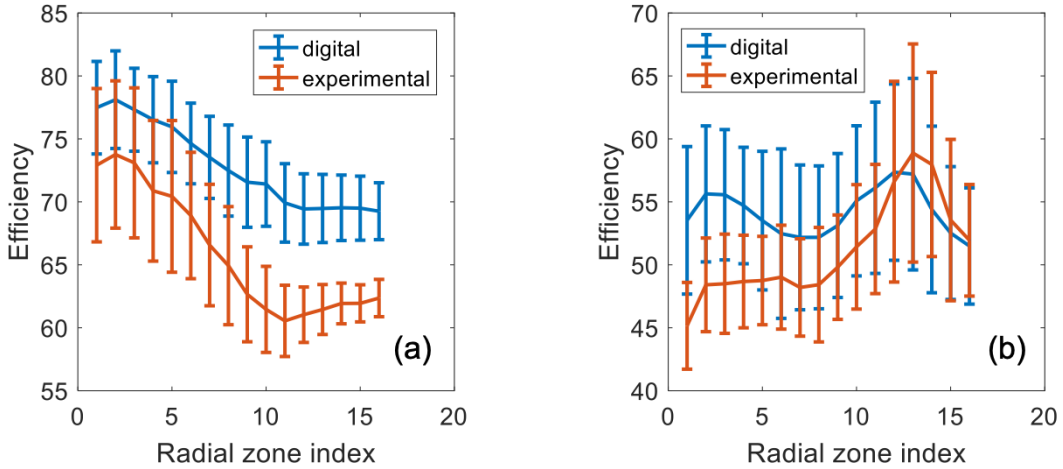


Figure 4.8: Average efficiency of focal spots as a function of their radial location (1965 focal spots). The error bars denote standard deviation values. Radial zones are equal area annular/circle across the fiber section, as defined in Figure. 4 of the main text, each containing 121 ± 7 focal spots. (a) Comparison of efficiencies w.r.t LOMs for mode-controlled focal spots created digitally (red curve) and experimentally (blue curve). (b) Comparison of efficiencies w.r.t HOMs for mode-controlled focal spots created digitally (red curve) and experimentally (blue curve).

4.6.3 Enhancement statistics of experimental and digitally computed mode-controlled output fields

The enhancement of a focal spot, defined as the ratio of peak focal intensity and the average image intensity, also varies with the radial position. In Fig. 4.9 we show two focal spots- one near the fiber axis and another near its boundary, each created using all the fiber modes (AMs), LOMs or HOMs. The all-mode data corresponds to focal spots created without mode control. We

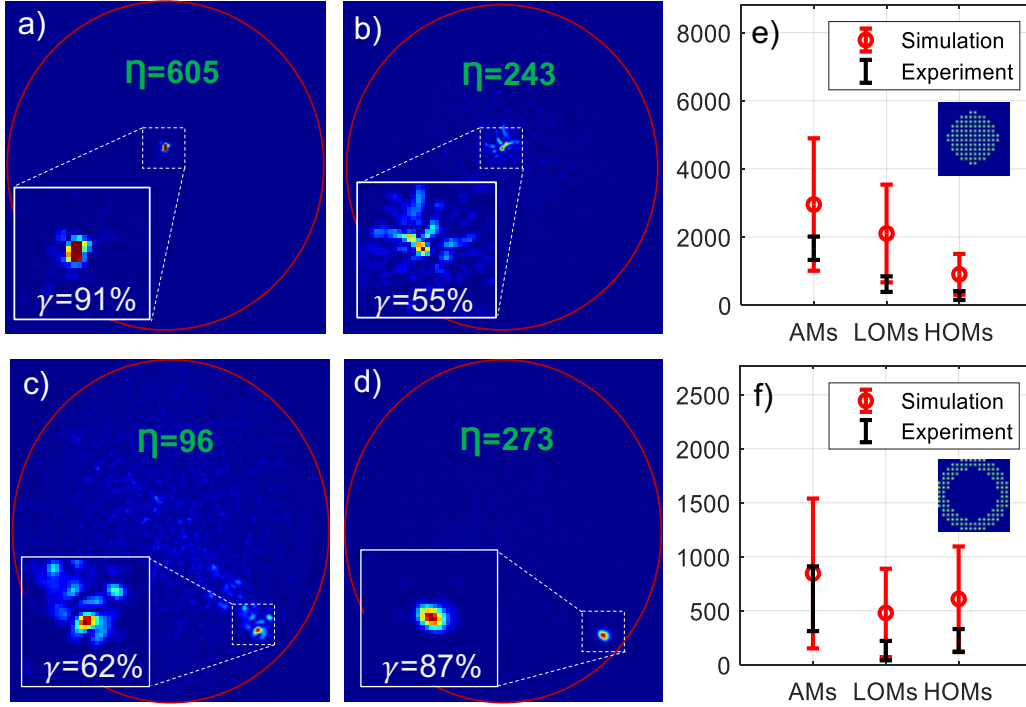


Figure 4.9: Enhancement as a function of radial position and mode selection. (a) Example of a near-axis focal spot intensity image created without mode control, (b) the same spot created using LOMs, and (c) using HOMs. (d) Example of a near- boundary focal spot intensity image created without mode control, (e) created using LOMs, and (f) using HOMs. The enhancements, E are indicated in green in the respective intensity images and the insets show a zoom-in on the focus profile. The experimental mode efficiency, η measured from their respective fields are also shown for the focal spot fields created with mode control. (g) Enhancement statistics of near- axis spots and (h) near-boundary spots. The spots in (g) and (h) belong to a circular inner region and an equal area annular outer region respectively in the fiber cross-section. Their exact locations are indicated in the respective figure insets. The x-axis indicates the set of modes chosen to generate the focal spots, AMs or all modes and LOMs and HOMs respectively. The y-axis shows the focus intensity enhancement. The red error bars correspond to experimental data, while the black error bars denote digitally computed focal spots using the experimental TM.

observe for both spots, as expected, that the best enhancement is achieved when all the modes are optimized and least is achieved when we use the non-dominant modes to create the focus. Focal spots created in the optimal regions of the selected mode sets yield intermediate enhancement, but the best mode efficiencies.

The error bars for the enhancement statistics also confirm the above observation, and the trend of the enhancement with varying mode compositions matches well for the digitally computed

or simulated focal spots and experimental focal spots. Also, the maximum achievable enhancement for near-boundary spots are smaller but remain steadier with varying mode compositions than the near-axis spots. Again, this indicates that fewer modes exist at the fiber boundary, as inferred in Fig. 4 of the main text.

4.6.4 Influence of mode selection on robustness

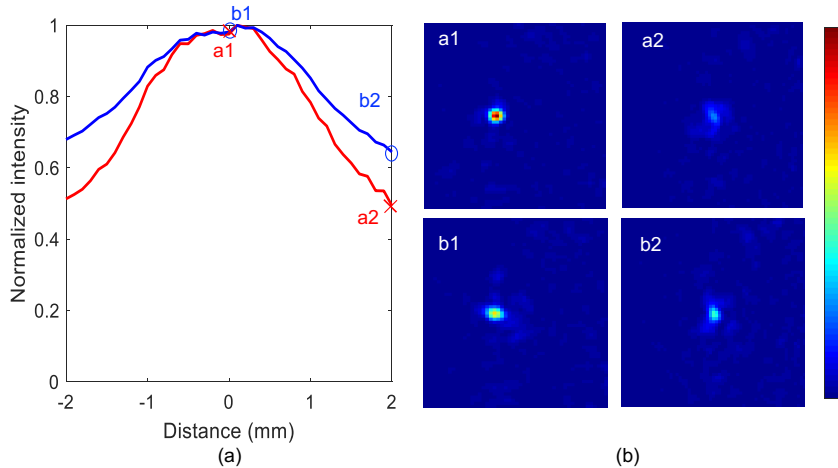


Figure 4.10: Experimental demonstration of bending resilience of focal spots created with and without mode selection. (a) Plot of normalized peak focal intensity of 150 near-boundary focal spots created using AMs (red) and the same focal spots created using HOMs (blue) with translation of the fiber distal tip. (b) Evolution of representative focal spots a1 and b1 created using AMs and HOMs respectively at the initial fiber position into a2 and b2 after a 2 mm translation of the distal tip. The displacement positions of the spots are marked in (a).

We compared focal spots created with and without mode selection to observe the effect of using fewer modes and mode selection on robustness. We generated 150 focal spots, each with all the modes (no mode selection, AM) and with HOM selection. The focal spots were created in the same positions for both mode selections unlike in the comparison shown in Fig. 5 of the main text. We moved the MyF distal tip along the horizontal axis in steps of $100 \mu\text{m}$, up to 2 mm. Fig. 4.10 (a) shows the change in the peak intensity averaged over 150 focal spots with translation while Fig. 4.10(b) shows the evolution of two focal spots over the motion range in both cases.

We observe that the spots created using fewer HOMs are $\sim 10\%$ more robust than those

created using all the modes. This is explained by the fact that when all the fiber modes are used for focusing, the change in the focal spot intensity due to fiber motion is larger as a result of all the modes contributing to the spot. On the other hand, when only the HOMs are used for focusing, the change in the focal spot intensity is smaller because it is a result of fewer mode interactions and lower probability of mode coupling. Although the total change in the output field is the same in both cases, the unselected LOMs in the second case primarily contribute and lead to change in the background intensity.

4.6.5 Mode control metrics

We introduced the efficiency and fidelity metrics in the main text of this paper to evaluate the mode control performance. Various other metrics have been considered. For instance, the same calculations can be done for the digitally computed fields. Furthermore, we can also compare the same focal spots generated digitally and experimentally. In this section, we present additional calculations to make all the above comparisons. All calculations are made for the focal spots in Fig. 3 (b) and (d) of the main text, which are named Spot 1 and Spot 2 respectively.

We generalize the efficiency and fidelity definitions from the main text and denote the efficiency for any given quantity, E as $\eta(E)$ and the Pearson correlation between two quantities A and B as $C(A,B)$, which is mathematically expressed in Eq. 4.6. We also measure the relative mean square error between two given intensity images, defined in Eq. 4.7.

$$C(A, B) = \frac{COV(A, B)}{\sigma_A \sigma_B} = \frac{\sum_{i=1}^N (A^i - \bar{A})(B^i - \bar{B})}{\sqrt{\sum_{i=1}^N (A^i - \bar{A})^2} \sqrt{\sum_{i=1}^N (B^i - \bar{B})^2}} \quad (4.6)$$

$$RMSE(I_2/I_1) = \frac{\sum_{i=1}^{N_{out}} (I_2^i - I_1^i)^2}{\|I_1\|^2} \quad (4.7)$$

4.6.5.1 Comparison of experimental with target fields and intensities

The efficiency, $\eta_{expt} = \eta(E_{out})$ for the experimental fields, E_{out} w.r.t. the target field, E_{target} , and the fidelity, $C_{expt} = C(I_{out}, I_{target})$ and $RMSE_{expt} = RMSE(I_{out}/I_{target})$ for the experimental

intensities, I_{out} w.r.t the target intensities, I_{target} , are summarized in Table S1. The high root mean square errors can be attributed to the background speckle intensity from the unselected modes.

Table S1: Efficiency calculations for the experimental fields w.r.t to the target fields and fidelity and RMSE calculations for experimental intensities w.r.t the target intensities.

Focal spot	η_{expt} (%)	C_{expt} (%)	$RMSE_{expt}$ (%)
Spot 1 (LOMs)	82.98	91.01	19.14
Spot 2 (HOMs)	74.22	96.45	21.19

4.6.5.2 Comparison of digitally computed and target fields and intensities

The efficiency, $\eta_{dig} = \eta(E_{dig})$ for digitally computed output fields w.r.t the target fields, and the fidelity, $C_{dig} = C(I_{dig}, I_{target})$ and $RMSE_{dig} = RMSE(I_{dig}/I_{target})$ calculations for the digitally computed output intensities, E_{dig} or I_{dig} w.r.t the target intensities are summarized in Table S2.

Table S2: Efficiency calculations for the digitally computed fields w.r.t to the target fields and fidelity and RMSE calculations for digitally computed intensities w.r.t the target intensities.

Focal spot	η_{dig} (%)	C_{dig} (%)	$RMSE_{dig}$ (%)
Spot 1 (AMs)	66.98	90.02	35.87
Spot 1 (LOMs)	75.93	84.69	44.58
Spot 2 (AMs)	64.54	95.96	38.29
Spot 2 (HOMs)	64.55	96.02	38.27

We observe from the table above that the efficiency marginally improves by selecting LOMs for the near axis focal spot while it barely changes for the focal spot at the boundary. This is an expected observation as we have created focal spots with mode control in their optimal regions. The efficiency curves in Figure 4 (a, b) also demonstrate this effect. On the other hand, the fidelity decreases, and the root mean square error increases as a result of mode selection. These observations are also explained by the increase in the background speckle intensity due to the unselected modes.

4.6.5.3 Comparison of experimental and digital field and intensities

We can compare the digitally computed and experimental intensities using their cross fidelity, $C_{dig-expt} = C(I_{dig}, I_{out})$ and $RMSE_{dig-expt} = RMSE(I_{dig}/I_{out})$. These calculations are summarized in Table S3. We observe very high, albeit not perfect correlation between the digitally computed and the experimentally obtained mode-controlled field.

Table S3: Cross-fidelity and RMSE calculations between digitally computed and experimental output intensities.

Focal spot	$C_{dig-expt}$ (%)	$RMSE_{dig-expt}$ (%)
Spot 1 (LOMs)	96.45	22.06
Spot 2 (HOMs)	99.4	10.12

Chapter 5

Multiview Scattering Scanning Imaging Confocal Microscopy through a Multimode Fiber

5.1 Introduction

In chapter 1, we saw that using prior knowledge about the object of interest, such as sparsity, can enable some degree of optical sectioning and resolution improvement. However the limited SNR in speckle imaging makes these improvements difficult to achieve. Confocal microscopy [186, 137] is a widely used technique that enables optical sectioning for imaging with high contrast from within scattering tissue volumes. It employs a scanning focal spot to sequentially sample small segments of the object followed by filtering of the backscattered light using a small pinhole in the scanning spot's conjugate plane, which blocks the out-of-focus light. In practice, the pinhole diameter is chosen to be large enough to achieve a desired tradeoff between optical sectioning and signal integrity. The technique has been widely successful, enabling for instance, clinical studies for imaging of the cornea [93, 187], imaging in body cavities using fiber-optic catheters [100, 89] and skin cancer detection [151, 77]. However, up to date, confocal imaging in the deep tissue regime remains infeasible due to the highly scattering nature of tissue and insufficient signal-to-noise ratio (SNR) levels.

Multiphoton microscopy is another effective approach to achieve optical sectioning with improved penetration depth. It provides intrinsic optical sectioning without needing to filter the backscattered light through a pinhole due to the two-photon [51] or multi-photon effect [88]. Unlike confocal microscopy, which utilizes only ballistic photons, multiphoton microscopy allows detecting

both ballistic and scattered photons [17], hence allowing imaging with better SNR. Furthermore, the use of long excitation wavelengths helps achieve penetration depths up to 2 mm using long excitation wavelengths [103, 88] or by employing optical clearing [135, 28]. However, the technique requires an expensive pulsed laser, the long wavelength excitation compromises the lateral resolution, and the penetration depth is still limited to a few millimeters.

Alternatively, several endoscopic solutions have been proposed to image deep inside the tissue using single-mode fibers [66, 136, 27], fiber bundles [172, 86], GRIN lenses [108, 13], multicore fibers [170, 168] and multimode fibers [139, 41, 40, 123, 32, 133, 177, 33]. Among these, multimode fibers (MMFs) make the most minimally invasive and efficient endoscopes that can relay the most amount of information in a given cross section. Proof-of concept demonstration of confocal imaging through multimode fibers have been made by digitally backpropagating from the detector to the object plane and filtering the signal through a virtual pinhole [117, 107] or by means of optical correlation [118]. These demonstrations showed imaging of 2-D samples through MMFs with optical sectioning and improved contrast. However, their application in imaging thick tissue samples still remains infeasible due to SNR limitations.

Here, we present Multiview Scattering Scanning Imaging Confocal (MUSSIC) microscopy through MMFs, an approach to overcome the SNR limitation in confocal microscopy through complex media by employing multiple coplanar virtual pinholes to collect multiple perspectives of the object and appropriately processing and combining them to retrieve a high-SNR confocal image. Our method builds on the principle of image scanning microscopy (ISM) [160, 130, 163, 154], which is used to boost the SNR in confocal microscopy for shift invariant systems. However, in contrast with ISM, MUSSIC does not require a direct measurement of the images of the scanning focal spots. Moreover, we demonstrate that given the transmission matrix [145] of the system, MUSSIC microscopy can be employed for a more general, shift-variant system such as a complex medium.

Our method is also key in unlocking the potential of confocal imaging for achieving super-resolution [160, 19]. Theoretically, confocal microscopy has the capability to gain a factor of two in the lateral resolution with respect to the diffraction limited resolution based on the Rayleigh

criteria [19, 20]. However, achieving this gain in resolution is impractical as it requires using a detection pinhole much smaller than the size of the scanning focal spot, which brings down the signal strength below acceptable levels. MUSSIC microscopy, on the other hand can practically achieve improved resolution by employing multiple small pinholes whose respective signals can be combined to obtain a reconstruction with a higher SNR.

Improvement in imaging resolution through multimode fibers has been demonstrated using two photon imaging [126, 166], saturated excitation [106], and by employing a multiple scatterer before the fiber [39, 140]. These approaches however come at the cost of expensive short pulse excitation sources, infeasibly high peak power or loss in transmitted light. Another approach used a parabolic tip design [21] to increase the effective NA however the design reduces the field of view and requires a non-zero working distance, which makes the endoscope susceptible to tissue induced light distortions due to index mismatch. Recently, resolution beyond the diffraction limit [6] has also been demonstrated using MMFs by assuming sparsity in samples however, it requires SNR levels of the sample higher than those feasible with bio-compatible markers.

In this work, we present a generalized framework to demonstrate the principle of MUSSIC microscopy through complex media and the theory for SNR and resolution gain. Further, we verify the theory experimentally by performing MUSSIC microscopy through an MMF by measuring its transmission matrix (TM). Using the TM, we generate focal spots on the far (distal) end of the MMF. As the focal spots scan the object, we collect the reflected speckle patterns on the MMF's near (proximal) end. Using the MMF's TM, we then back-propagate the collected speckle patterns to the object plane [117, 107] to virtually access the scanning focal spot fields and implement MUSSIC microscopy using the weighted pixel reassignment method [130, 163]. We evaluate the SNR and resolution of the reconstructed images and compare our approach with the conventional confocal and single pixel imaging approaches. Our experimental approach is quite general and is also applicable to endoscopic imaging systems with separate excitation and detection paths [27, 190, 131, 58].

5.2 Principle of image scanning microscopy

Consider a scanning microscope shown in Fig. 5.1 (left) with Gaussian excitation and detection point spread functions (PSFs) h_{ex} and h_{det} respectively and let the object's transmission function be $t(u, s)$ where u and s are the object plane coordinates and the object scan position respectively. If v denotes the detector plane coordinates and $o(s, v)$ denotes the output field in the detector plane, then the microscope can be described with the help of a convolution integral shown in Eq. 5.1.

$$o(s, v) = \int h_{ex}(v - u)h_{det}(u)t(u + s)du \quad (5.1)$$

In a type II confocal scanning microscope [161] a pinhole is placed on the optical axis, i.e., $v = 0$. Assuming that the detection wavelength is identical to the excitation wavelength, the detector plane field observed by the confocal pinhole is given by Eq. 5.2.

$$o(s, 0) = \int h_{ex}^2(s - u)t(u + s)du \quad (5.2)$$

The product of the excitation and detection PSFs (assumed identical) in the above equation yield a net PSF with a $\sqrt{2}$ times smaller full width at half maximum (FWHM). This gain in resolution however is difficult to achieve in practice as it requires a point-sized pinhole that rejects most of the signal. In practice, the pinhole size is chosen to be large enough to allow a feasible SNR.

One approach to preserve the resolution gain in the above system is to employ multiple small pinholes instead of a single large one. When $v \neq 0$ in Eq. 5.1, the net PSF is a product of the original excitation PSF with a shifted version of the on-axis detection PSF as depicted in Fig. 5.1 (right). This net PSF still has a $\sqrt{2}$ times smaller FWHM, albeit it is shifted with respect to the net PSF of the on-axis pinhole. Hence, each of the off-axis pinholes can provide separate image information with improved resolution, which can be combined together if the distance between the pinholes is known. For example, when the detection and excitation wavelengths are identical, the

image from a pinhole at a distance of d from the optical axis needs to be shifted by a distance $d/2$ towards the optical axis.

A readily available array of pinholes is a camera detector whose pixels can serve as individual pinholes for implementing the above technique. Since the camera records images of the scanning focal spots, this technique is known as image scanning microscopy [160, 130, 163, 154]. The process of re-shifting and combining the images from different pinholes is known as pixel reassignment.

To date, ISM has enabled confocal microscopy with high resolution and SNR in various shift-invariant microscopic systems that can be described using a convolution integral. However, its applicability in the case of complex media such as MMFs has remained unclear. In the following section, we present a generalized matrix formalism to describe the most general systems including MMFs. We use the model to predict how principles similar to ISM can be applied to shift variant systems.

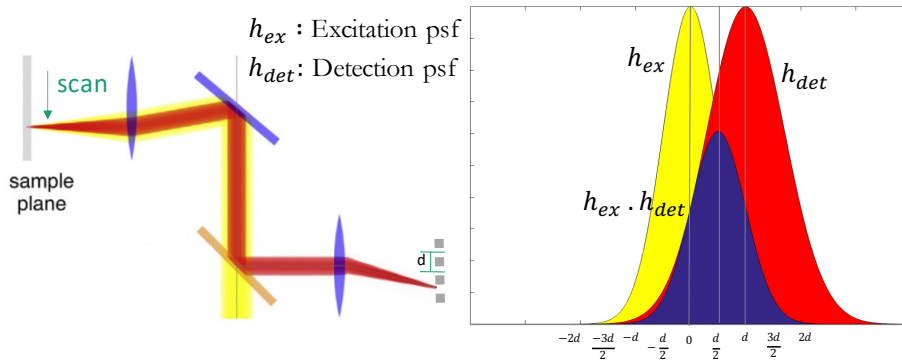


Figure 5.1: Principle of resolution and SNR gain in image scanning microscopy. Left: A laser scanning confocal microscope consisting of a 4-f system. The incident light (yellow) reaches the sample plane to scan the sample as it is translated. The reflected light (red) is detected in the conjugate image plane where it is filtered through an array of pinholes or a camera detector. Right: Illustration of the excitation (yellow) and detection (red) PSFs of an off-axis pinhole and their product or the net PSF (blue), which is shifted from the optical axis. The image obtained from this pinhole can be re-shifted and combined with the on-axis image to boost the SNR of the image reconstruction.

5.3 Generalized Matrix Formalism

Consider a general imaging system whose input to output transformation is described by a transmission matrix, T . Let the object's reflectance be modeled using a diagonal matrix, O and let the fields entering and leaving the systems be stored in a vectorized form in the columns of 2D matrices. Let these field matrices be denoted by the letter E followed by their corresponding superscripts - "in" for incident fields, "p" for proximal fields and "d" for distal fields. The proximal fields reflected back through the system are then obtained using Eq. 5.3.

$$E^p = T^t O T E^{in} \quad (5.3)$$

For a shift invariant system, the T matrix is a convolution matrix whose columns contain the vectorized and circularly shifted PSF of the system as illustrated in the top row of Fig. 5.2. Assuming reciprocity, the distal plane to the proximal plane propagation is represented by the T^t matrix. For a raster scan approach the incident field matrix, E^{in} is an identity matrix whose k^{th} column contains the vectorized focal spot at the k^{th} input pixel. The k^{th} column and row of the E^{in} and E^p matrices respectively are expanded to 2D and also illustrated in the top row of Fig. 5.2 using arrows. The E^p matrix serves as the raw data whose on-axis and off-axis pixel values yield the raw images needed to perform image scanning microscopy.

On the other hand, for a shift variant system, such as a complex media, the forward transmission matrix, T is a complex-valued random matrix as shown in the second row of Fig. 5.2. Using the TM approach described in chapter 1, we can shape the k^{th} incident field E_{in} to create a focal spot at the k^{th} pixel in the distal plane. However, since we propagate back through the same medium, the spatial information is lost again and the obtained proximal fields are random speckle patterns.

To regain access to the scanning focal spots, as required for performing confocal microscopy, we propose a method to virtually backpropagate from the proximal to the distal plane. This is achieved by inverting the the T^t matrix in Eq. 5.3 by multiplying the left and right side of Eq. 5.3 with the psuedoinverse of the T^t matrix. The resultant fields are the virtual distal fields which

can then be used to extract the on-axis and off-axis confocal images in a process similar to image scanning microscopy.

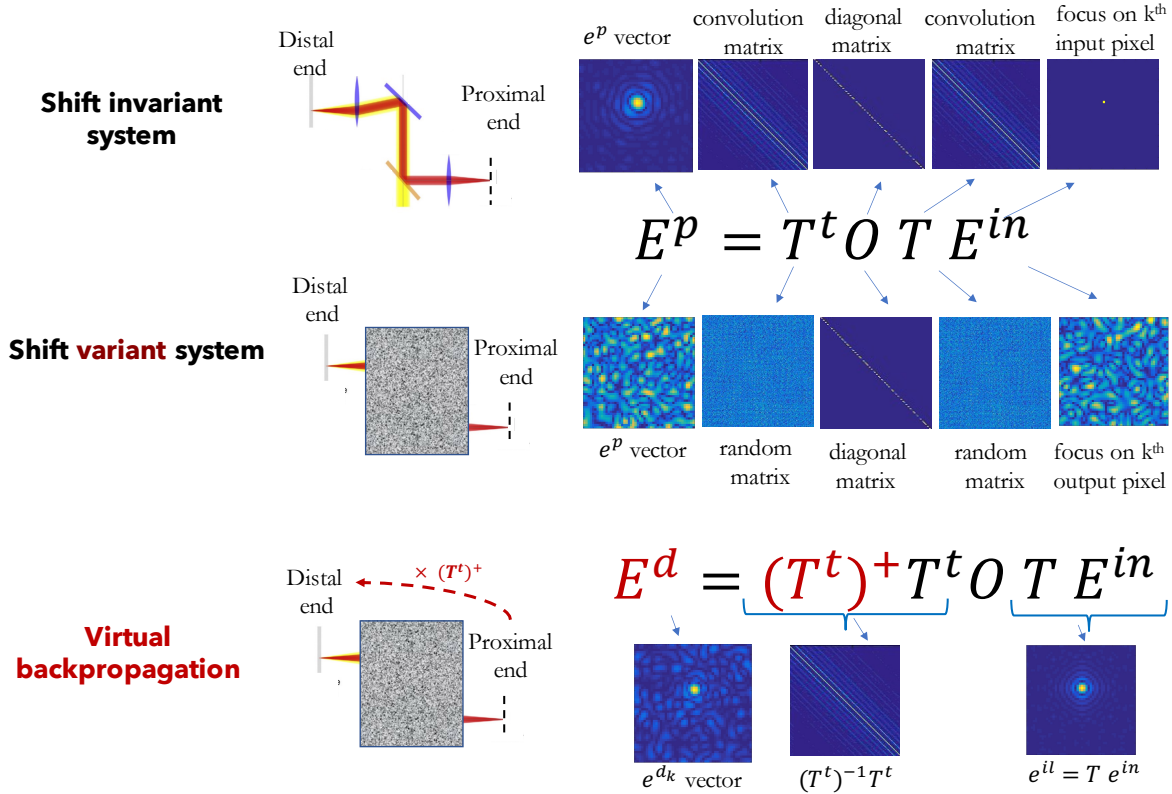


Figure 5.2: Generalized matrix formalism for imaging through complex media. Top row: Illustration of a shift invariant microscope consisting of a 4-F system. The visualizations of the different matrices corresponding to each term in the system equation, Eq. 5.3 are displayed using arrows. Examples of the vectorized input and proximal fields are shown after being expanded to 2D for visualization. The transmission matrix of the shift invariant system is a convolution matrix with an Airy disk kernel. Middle row: illustration of a shift variant complex medium. The visualizations of the different matrices corresponding to each term in the system equation, Eq. 5.3 are displayed using arrows. The input field is chosen such that it transforms into a focal spot at the k^{th} pixel after propagating through the system. The transmission matrix of the system is a complex random matrix leading to a random speckle field in the proximal plane. Bottom row: Illustration of the virtual backpropagation method. By multiplying the left and right hand sides of Eq. 5.3 with the pseudo-inverse of the T^t matrix, we can backpropagate to the distal plane and access the scanning focal spots. This raw data is similar to that obtained in ISM for shift invariant systems.

5.4 Principle of MUSSIC microscopy through a multimode fiber

Imaging through an MMF is performed by calibrating the relationship between the input and output fields through the system, described by its TM. The TM can be measured empirically with both phase and amplitude information by sending an orthogonal set of input fields into the system accompanied with a phase-stepping reference field [145, 32] and measuring the corresponding complex-valued output fields. A spatial light modulator (SLM) is employed to generate different input fields. This system can also be described using Eq. 5.3. Here, we relax the reciprocity constraint previously assumed and assume that the MMF has a forward TM, T , and a different distal plane-to-proximal plane TM, T^b . This generalization allows us to decouple the excitation and detection paths, hence eliminating the need for precise matching of the excitation and detection optics.

Let the subscripts denote the row and column indices of the matrices respectively. If we denote the field illuminating the object, as $E^{il} = TE^{in}$, then for the k^{th} incident field, E_{*k}^{in} , where the asterisk denotes the full set of indices along the particular dimension, the l^{th} pixel of the proximal field, E_{lk}^p is calculated using Eq. 5.4.

$$E_{lk}^p = \sum_{i=1}^{N_{out}} T_{li}^b O_{ii} E_{ik}^{il} \quad (5.4)$$

Eq. 5.4 shows an overlap function between the excitation and detection point spread functions (PSFs), T_{l*}^b and E_{*k}^{il} weighted by the object reflection function O , analogous to the overlap integral used to calculate the resultant field at a confocal pinhole in a conventional confocal microscopy system [19].

Unlike shift invariant confocal imaging systems, the excitation and detection PSFs for an MMF follow a complex random distribution. Hence, to adopt the raster scan approach for MMF imaging [139, 41, 32], an input field, $E_{*k}^{in} = T_{*k}^\dagger$ must be projected on the SLM to create a diffraction limited focal spot on the k^{th} pixel on the distal side of the MMF. The dagger denotes the conjugate transpose operation above. Since the detection path is also through the MMF, the focal spot

scanning the object transforms to a speckle pattern after reflecting back to the proximal end of the MMF, hence destroying all spatial information. To reverse the effect of the detection path, we can digitally back-propagate the detected proximal speckle fields to the distal plane [117, 107] using the MMF's backward TM, as depicted in the schematic in Fig. 5.3 (a). The virtual distal field denoted as E^d , is calculated by taking the product of the proximal fields with the inverse of the backward TM. The TM is however a poorly conditioned matrix and its inverse does not exist. If we approximate its inverse as its conjugate transpose, as we did earlier for creating phase conjugated focal spots on the distal end, then the back-propagated fields, E^d can be calculated using Eq. 5.5.

$$E^d = (T^b)^\dagger E^p = (T^b)^\dagger T^b O E^{il} \quad (5.5)$$

A zoom-in on an example virtual distal field is shown in Fig. 5.3 (b) along with the discrete grid on which it is sampled. Each intersection point on the grid indicates a data point and can be viewed as a virtual pinhole. We define $D_{T^b} = (T^b)^\dagger T^b$ as the virtual detection PSF of the system. Similarly, we define, the SLM-to distal plane excitation PSF, $D_T = T T^\dagger$, which is also the illumination field matrix, E^{il} , assuming that a plane wave is incident on the SLM. The matrices D_T and D_{T^b} have a structure similar to a convolution matrix used to represent the TMs of shift invariant systems [179, 46]. Their Hadamard product yields the net PSF of the system which is narrower than the individual PSFs as depicted in Figure 5.3 (c). This narrower net PSF is the source of resolution gain in MUSSIC microscopy and the resolution enhancement is determined by the size of each virtual pinhole relative to the size of the virtual detection Airy disk.

Once we obtain the full virtual distal field matrix, E^d , the on-axis confocal image is obtained from its main diagonal, E_{kk}^d where $k \in (1, N_{il})$ denotes all distal scan positions. This main diagonal comprises the measurements from the central virtual pinhole, p2 indicated in Fig. 1(b). Similar mutually shifted confocal images are also obtained from the diagonals, E_{lk}^d , corresponding to the neighboring pixels of k (such as p1 and p3 shown in Fig. 5.3 (b)) where l takes $N^2 - 1$ values other than k in the $N \times N$ - pixel neighborhood of each scan position k . All the N^2 confocal images can then be re-shifted to a common axis, weighted according to their signal strength and combined to

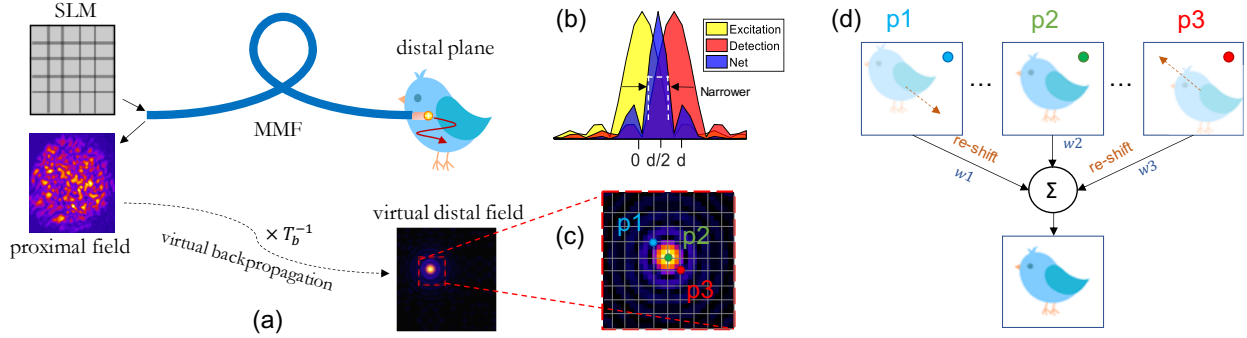


Figure 5.3: Principle of MUSSIC microscopy through a multimode fiber. (a) Illustration of the principle of MUSSIC microscopy through a multimode fiber. An SLM projects the phase patterns to generate scanning focal spots on the distal end, where the object is located. Light reflected from the object couples back into the fiber and reaches the proximal end as a speckle field. The proximal speckle field is recorded and virtually backpropagated to the distal end using the backward TM. This virtual distal field matrix comprises the MUSSIC raw data. (b) **Resolution improvement in MUSSIC microscopy.** The excitation PSF, D_T , the virtual detection PSF, D_{T^b} , and the net PSF, calculated as the product of the former two are shown in yellow, red and blue respectively for an example confocal image obtained from a virtual pinhole p_i at a distance d from the on-axis pinhole. Although the net PSF is shifted from the axis by a distance, $d/2$, it is narrower than the former two PSFs, hence leading to an improved resolution. The excitation and detection wavelengths are assumed to be identical here. (c) Zoom-in on the focal spot in the virtual distal field shown in 1 (a), as demarcated by the red dotted line. Each intersection point of the grid corresponds to a data point or pixel, that acts as a virtual pinhole. While the central pixel, p_2 measures the on-axis confocal image, the pinholes p_1 and p_3 also measure similar confocal images from different perspectives. (d) **SNR improvement in MUSSIC microscopy.** Illustration of the process of retrieving a high SNR MUSSIC image from multiple confocal images obtained from different virtual pinholes. Confocal images from the pinholes p_1 , p_2 and p_3 , as marked in 1(b), identified by their corresponding colored- blue, green and red dots are shown on the top as an example. Besides the image obtained from the on-axis pinhole, p_2 , all confocal images have parallax errors determined by the location of their corresponding virtual pinholes. By applying appropriate shifts and weights to them and combining them together, a single high-contrast MUSSIC image is obtained.

yield a high-SNR MUSSIC image reconstruction as illustrated in Fig. 5.3 (d).

5.5 Methods

5.5.1 Calibration of forward TM, T

The forward TM, T is measured with both phase and amplitude information, by sending a complete basis of orthogonal input fields into the fiber accompanied with a phase-stepping reference

field. We choose the plane waves basis which transforms to focal spots in the Fourier plane, which is then coupled into the MMF. These patterns are constant in amplitude and their phases are modulated using a spatial light modulator (SLM). The SLM's active area is divided into two sections each for the changing grating pattern and a phase-stepping reference frame that surrounds it. The intensity measurements at the fiber output for each projected pattern, as the reference field is phase stepped, allows recovering the output fields [32, 145]. These output fields are vectorized and used to build all the rows of the matrix T .

5.5.2 Calibration of backward TM, T^b

The TM of an MMF obeys the reciprocity rule i.e., $T^b = T'$. However, since the TM is recorded between the SLM and the distal plane, the above assumption only holds true if the detection plane perfectly matches the SLM plane in scale and orientation. This is a practically challenging task and requires a sensitive and time-consuming alignment procedure [117]. It also does not account for coupling losses from the sample to the fiber distal end. Moreover, oftentimes, it is desirable to separate the collection and detection pathways in endoscopes to improve throughput or to gain some feedback from the distal end in which case $T^b \neq T'$. For other modalities like fluorescence imaging, the excitation and detection PSFs are different by default due to difference in the excitation and fluorescence wavelengths. With these considerations, here we propose a separate calibration of the matrix T^b from the distal plane to the detector plane. Towards this end, we place a mirror at the distal end of the fiber and scan focal spots on it, while measuring the reflected fields on the proximal end, denoted as $E^{p-mirror}$. These measurements give us an estimate of T^b , which we denote as T_{obs}^b as described in Eq. 5.6.

$$T_{obs}^b = E^{p-mirror} = T^b I E^{il} \quad (5.6)$$

The matrix I in the above equation represents the mirror reflection matrix, which we assume to be an identity matrix. The distal fields are then given by Eq. 5.7.

$$E^d = (T_{obs}^b)^\dagger E^p = (E^{il})^\dagger D_{T^b} O E^{il} \quad (5.7)$$

The additional rightmost term $(E^{il})^\dagger$ on the right-hand side of the above equation occurs because of our double pass approach for calibration of T^b . Since we use a raster scan approach, both the E^{il} and $(E^{il})^\dagger$ matrices have the structure of a convolution matrix with a diffraction limited Gaussian kernel and E^d still gives a measure of the confocal images of the object. Moreover, the theoretical resolution gain is also preserved as the bandwidth of the terms on the left and right of the object, O , in the above equation remain unchanged. Appendix section 1 provides a more detailed derivation of Eq. 5.7.

5.5.3 Optimal inversion of backward TM and band-pass filtering

As mentioned earlier, we can use the conjugate transpose operator when the inverse of a matrix does not exist. This method works well for generating perfect phase conjugated focal spots, as required when raster scanning on the distal side of the fiber. However, when calculating the backpropagated distal fields, the conjugate transpose is not the best inversion method. We can optimize the inversion of the backward TM using a Tikhonov regularization technique [117, 146]. This involves computing the singular value decomposition of the backward TM, $T_{obs}^b = USV^\dagger$ and finding its inverse using Eq. 5.8.

$$(T_{obs}^b)^{RI} = VS^{RI}U^\dagger \quad (5.8)$$

S^{RI} is the regularized inverse of the diagonal matrix of singular values, S , calculated by replacing the singular values σ_i in the diagonal of S with $\sigma_i/(\sigma_i^2 + \beta^2)$, where β is the regularization parameter. We find that by calculating the back-propagated distal fields using Tikhonov regularized inverse of the T_{obs}^b instead of $(T_{obs}^b)^\dagger$ in Eq. 5.7 yields image reconstructions with improved contrast. For our results, we chose a β value equal to 6% of the highest singular value of the backward TM.

5.5.4 Bandpass filtering, normalization and mean subtraction

We perform digital filtering to bandlimit all acquired data. This eliminates the noise in the high frequencies and ensures that all acquired images have speckles with a minimum grain size

limited by diffraction. The frequency cutoff is found by setting a minimum threshold to the total energy in the frequency space averaged over all acquired images.

We also normalize the reconstructed confocal and MUSSIC images of the object w.r.t to their “blank” counterparts or the confocal and MUSSIC images obtained when a mirror is placed at the distal end. This helps account for the non-uniformity and intensity variations in the focal spots used to scan the object and significantly improves the image quality. The effect is particularly strong since we employ a non-uniform internal reference for phase measurements. Supplementary figure 1 shows a comparison of the reconstruction images before and after normalization. Furthermore, we subtract the mean of all the columns of the backward TM from its every column. This ensures that any unmodulated light that leads to a common background in all the measured speckle patterns are eliminated.

5.5.5 Imaging without full field back-propagation

Calculating the full matrix E^d , is a computationally challenging feat, with complexity $O(N_{il}^2 N_{in})$. However, in fact access to the full back-propagated distal fields is not necessary to calculate the confocal or MUSSIC images. The only data points required in each distal field are in the neighborhood of the scanning focal spot, for every scan position. This number, which we define as $N_{pinholes}$ is chosen to be roughly equal to the number of pixels that sample a focal spot and is much lower than the number of illuminations used for imaging. Hence, if we compute only the desired diagonals from the matrix E^d corresponding to the $N_{pinholes}$ neighboring pixels, the complexity of the calculation drops down only to $O(N_{pinholes} N_{in} N_{il})$ for the MUSSIC image and only $O(N_{in} N_{il})$ for a single confocal image. When assuming the inverse of the backward TM to be its conjugate transpose, this method for obtaining the confocal image has been termed the correlation method [117]. This is because the complex correlation between the proximal fields in the absence and presence of the object, denoted here as T_{obs}^b or $E^{p-mirror}$ and E^p respectively, is calculated by taking the product of the conjugate transpose of the former with the latter and normalizing the result w.r.t. the Euclidean norm of the former. The normalization here is identical to the normalization we

describe in section 4. Imaging using the correlation method, enables MUSSIC reconstruction of a 20,000-pixel image in 4 minutes. A comparison of this reconstruction with the reconstruction after Tikhonov regularization of the backward TM reveals that although the regularization considerably improves the image quality, the faster reconstruction also provides a pretty good estimate of the object. This comparison is shown in Appendix figure 2.

5.6 Experimental Setup

The experimental setup for MUSSIC microscopy through an MMF is illustrated in Fig 5.4. We use a 785 nm CW Crystal laser and a Meadowlark optics liquid crystal SLM (HSPDM 512) for phase modulation. The laser beam goes through a half waveplate and polarizer for polarization control, followed by a 4-F system to match the beam diameter to the active area of the SLM. The SLM plane is then imaged onto the back-aperture of a microscope objective, OBJ 1, which couples the light into the MMF. We used a step-index fiber of diameter 50 μm and 0.22 numerical aperture (NA) for all our experiments. A polarizing beam-splitter (PBS) between the SLM and OBJ 1 is used to direct the back-reflected light from the fiber onto a camera, CAM 2. A half waveplate before the PBS allows controlling the polarization axis of the incident beam and a quarter waveplate along with the PBS act as an optical isolator to prevent back-reflections from the proximal facet of the fiber from reaching the camera. The distal facet of the MMF is imaged onto a camera, CAM 1 using another lens during the forward TM calibration. A polarizer before the camera allows detection of only one polarization component.

After the forward TM calibration, a mirror is placed near the fiber distal tip for calibration of the backward TM. The backward TM is calibrated using back-reflected fields on the proximal side of the fiber, while focal spots are projected on the distal side. A phase shifting reference frame is simultaneously projected on the SLM along with the phase conjugated patterns for distal raster scan, for measuring both the phase and amplitude of the back-reflected fields. The back-reflected light from the mirror couples back into the fiber and is detected on the proximal side using another camera, CAM 2. This camera images the back-aperture of the microscope objective OBJ 1 using

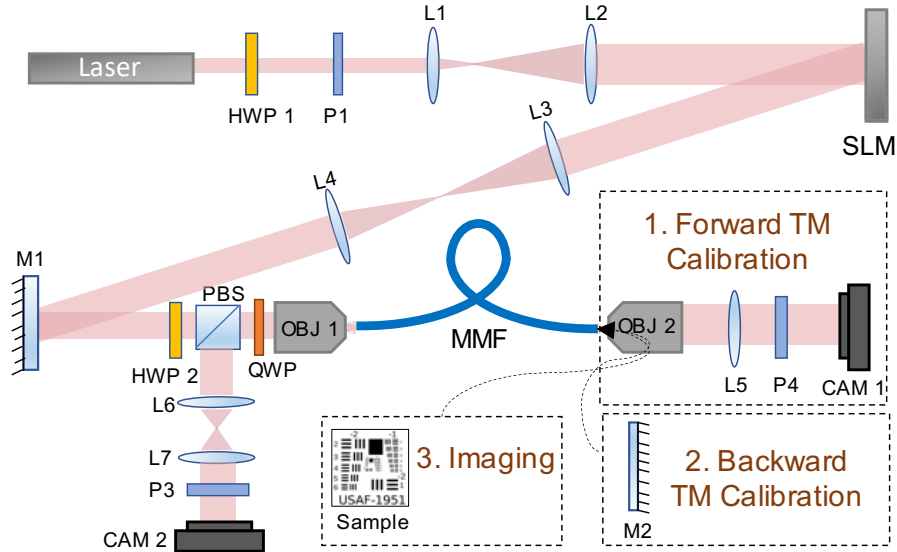


Figure 5.4: Experimental setup for image scanning microscopy through an MMF. HWP 1-2: Half waveplates, P1-3: linear polarizers, L1-7: lenses, MMF: 10 cm long step-index fiber from Thorlabs (FG050LGA), PBS: polarizing beam-splitter, M1-2: mirrors, QWP: quarter waveplate, OBJ 1-2: microscope objectives, CAM 1-2: cameras to measure distal and proximal intensities.

another 4-F system and is placed in a plane equivalent to the SLM plane. A polarizer before the camera allows detection of a single polarization component.

After both calibrations, the sample to be imaged replaces the mirror at the distal facet of the MMF, and the back-reflected fields from the object are recorded as it is raster scanned.

5.7 Results

5.7.1 SNR and resolution analysis

We perform confocal MUSSIC microscopy in simulation and compare the SNR and resolution of the reconstructed images. We model the MMF TM as a complex random matrix and reconstruct the image of a quadrant of the binary Siemens star using the simulated proximal speckle fields, following the backpropagation process described earlier. We added Gaussian noise with 5% variance to the simulated proximal fields before the image reconstruction. Each virtual pinhole in our simulation has a radius of 0.11 Airy unit (a.u.), where we have defined 1 Airy unit as the radius of

the Airy disk scanning the object. Hence one Airy disk spans across 9×9 individual pinholes.

The ground truth object and its confocal and MUSSIC reconstructions are shown in Figs. 5.5 (a-d). Figs. 5.5 (b,c) show the confocal reconstructions using a 3×3 macro-pinhole and a 9×9 macro-pinhole respectively. Fig. 5.5 (d) uses the same group of 9×9 pinholes as 5.5 (c) but employs the MUSSIC approach to process the data. We find that although the SNR improves significantly between the confocal image reconstructions as the size of the macro-pinhole increases, the resolution of the image degrades. On the other hand, the MUSSIC reconstruction, which uses the same group of pinholes as the second confocal image retains the high-SNR, while also preserving the resolution. The difference in resolution can be more clearly visualized in Fig. 5.5 (e) that shows the normalized cross sections in the image reconstructions corresponding to the green solid lines in Figs. 5.5 (a-d). We find that confocal reconstruction with the 1 a.u. pinhole fails to resolve the image features, while the MUSSIC reconstruction using the same raw data resolves them just as well as the confocal reconstruction with the 0.33 a.u. pinhole.

We also compare the root mean square error of different normalized reconstructions as a function of the annular radius measured from the center of the Seimens star or the bottom right corner. For this comparison, no noise was added to the reconstructions to analyze the effect of using increasing number of pinholes on resolution. We divide the image quadrant into 15 radial zones and plot the error w.r.t. the ground truth image in each zone for the different reconstruction methods. We find that while the error for the confocal reconstruction images increases with the radius of the macro-pinhole, the error in the MUSSIC reconstruction remains almost unchanged as the number of used pinholes increases from 3×3 to 13×13 . The inset images in the figure show the radial zones 1, 5 and 15 from left to right. Next, we analyze the reconstruction error and correlation as a function of the number of pinholes used, for the green line cross-sections marked in Fig. 5.5 (a-d) in the absence of noise. We find that the error and correlation w.r.t. the ground truth cross-section increases and decreases respectively as the number of pinholes constituting the macro-pinhole increases for the confocal reconstruction. On the other hand, both metrics for the MUSSIC reconstructions remain unaffected, indicating that the image quality is preserved.

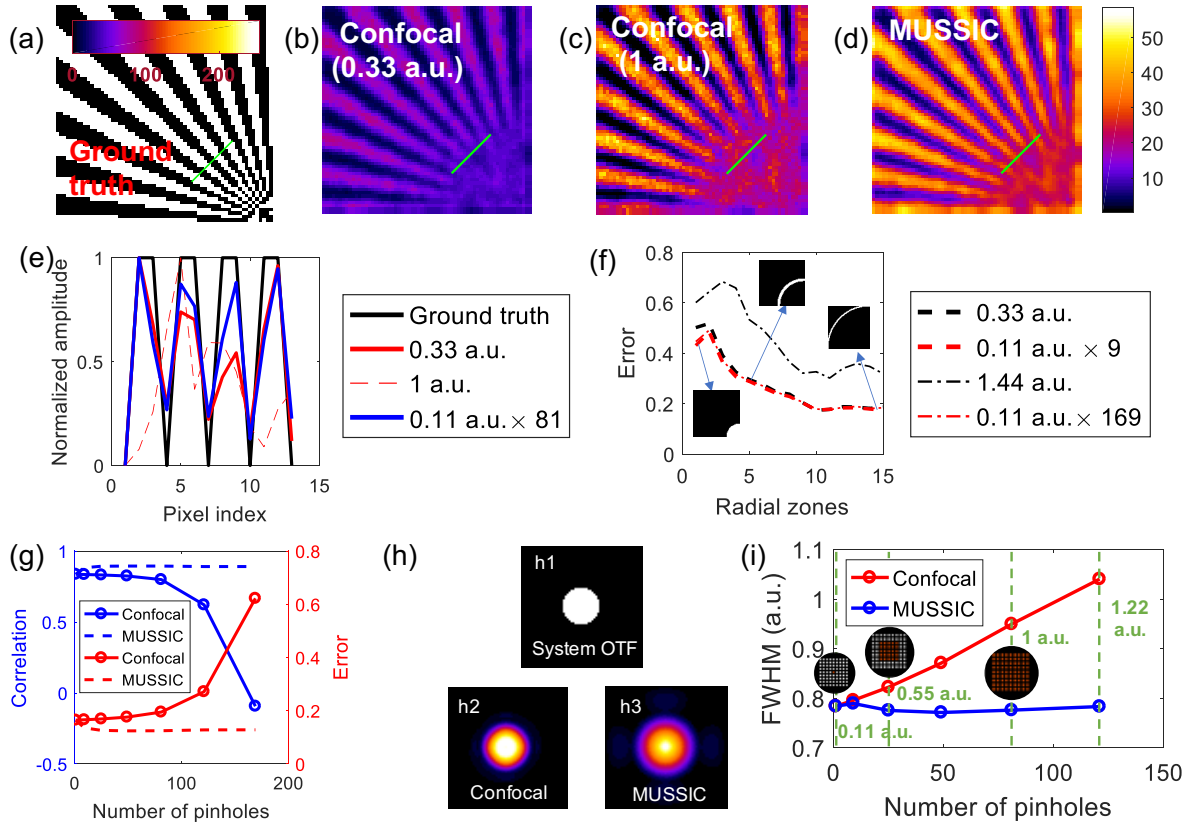


Figure 5.5: Comparison of confocal and MUSSIC image reconstructions. a) Binary object (ground truth), (b) Confocal image obtained from a 3×3 macro-pinhole of size 0.33 a.u. and (c) a 9×9 macro-pinhole of size 1 a.u. (d) MUSSIC image obtained using 81 pinholes, each of radius 0.11 a.u. (e) Plot of the normalized cross sections indicated by the solid green lines in (a-d). (f) Root mean square error for 15 annular regions of increasing radii starting from the bottom right, for normalized confocal images (black) and MUSSIC images (red) using 9 and 169 pinholes. The insets illustrate the annular regions 1, 5 and 15 respectively. (g) Error and correlation of confocal and MUSSIC images as a function of the number of pinholes used, as measured for the cross section marked by the green solid lines shown in (a-d). (h) Optical transfer function of the system (h1) and the average frequency response of the system for a point object obtained by performing virtual confocal microscopy (h2) and MUSSIC (h3) using 81 pinholes. (i) Full width half maxima of the net PSFs obtained from confocal and MUSSIC reconstructions as a function of the number of pinholes used. The net confocal pinhole size in Airy units is indicated at various points in green font. The black circular insets illustrate a 1 a.u. pinhole array in white with the red pinholes indicating the pinholes used.

Furthermore, we compare the average frequency response for the confocal and MUSSIC methods obtained for a point object using 81 pinholes. We find that the frequency cutoff of the MUSSIC reconstruction is almost the double that of the OTF of the system, which is the

theoretically claimed gain in resolution according to Rayleigh’s criteria [20, 19]. On the other hand, the confocal reconstruction obtained from the 1 a.u. pinhole has a frequency cutoff 1.4 times higher than that of the system OTF. Finally, we computed the PSFs for the confocal and MUSSIC methods and plotted the full width half maxima (FWHM) of the PSFs as a function of the number of pinholes used. We find that the FWHM for the confocal reconstruction increases with the number of pinholes constituting a macro-pinhole, while the FWHM for the MUSSIC reconstruction remains unchanged.

5.7.2 Experimental results

We experimentally demonstrate MUSSIC microscopy through a multimode fiber and compare the reconstruction SNR as the number of pinholes increases in Fig. 5.6 (a-c). We also show the single pixel image (SPI) reconstruction obtained by integrating the absolute values measured by all the pinholes or pixels in Fig. 5.6 (d). The field of view (FOV) consists of the fourth and fifth elements of the 7th group in the USAF 1951 resolution target, which have a resolution of 181– and 203-line pairs/mm respectively. We observe a consistent improvement in image contrast as the number of pinholes increases. The SPI image obtained from a much larger number of pinholes has a higher-SNR but lower contrast as can be seen from the plot of the normalized average cross section along the horizontal direction for the reconstructions in Fig 5.6 (a-d). The cross-sections correspond to a cropped region indicated by dotted lines in Figure 5.6 (c). Moreover, we find a factor of 6.2 improvement in the root mean square contrast in the MUSSIC reconstruction using 25 pinholes with respect to the SPI reconstruction.

Next, we demonstrate the optical sectioning capability of the MUSSIC technique. The FOV shows the first element of the 7th group in the resolution target. We move the 2D target in steps of 20 μ m in the axial direction and away from the fiber distal facet and capture the back-reflected fields from the object at three z-positions. We compare the SPI reconstructions with the MUSSIC reconstructions at the three positions in Fig. 5.7. We can observe that the object almost disappears in the background already after a movement of 20 μ m in the case of the MUSSIC images, while

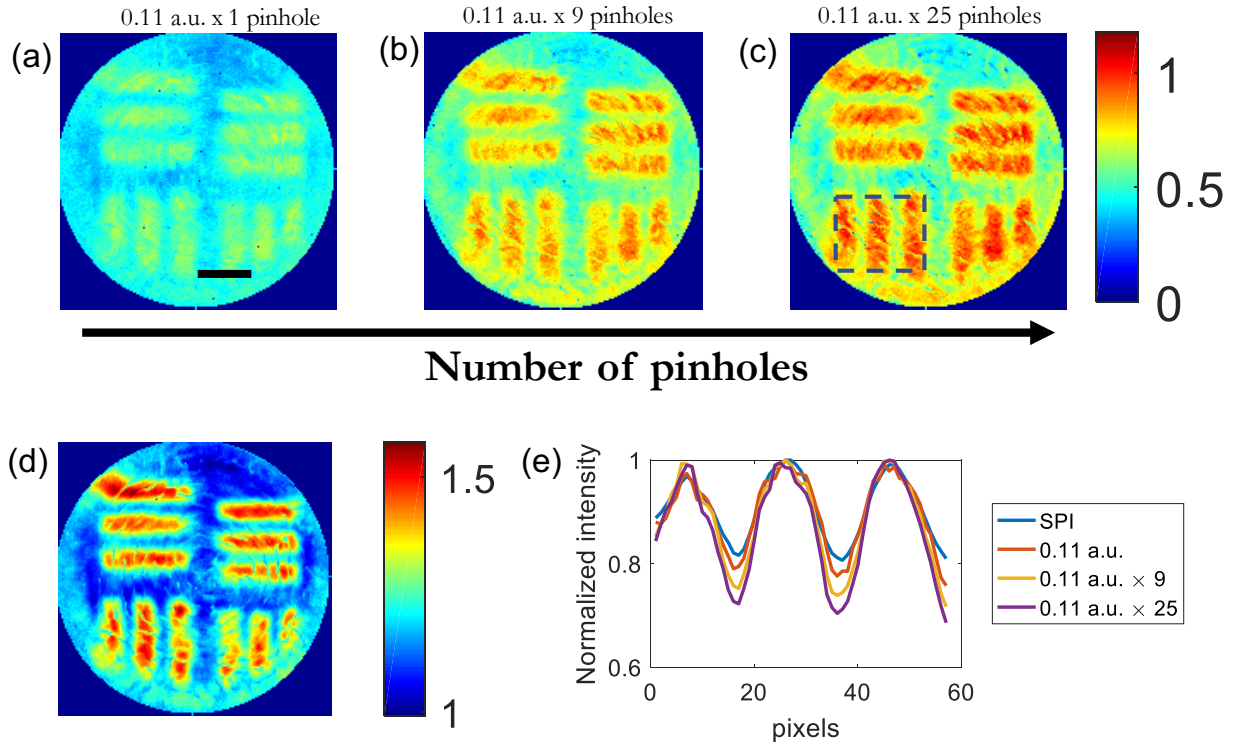


Figure 5.6: SNR comparison in MUSSIC microscopy. (a-d) Comparison of SPI, confocal and MUSSIC reconstructions of a window in the USAF 1951 resolution target. The FOV is a 50 microns wide- 160×160 -pixel window. (a) digital confocal reconstruction using a 0.11 a.u. pinhole, (b) MUSSIC reconstruction using 9×0.11 a.u. pinholes and (c) MUSSIC reconstruction using 25×0.11 a.u. pinholes. (d) Single pixel image obtained by integrating the absolute value of the entire proximal field. (e) Average cross section along the horizontal direction from the reconstructions in (a-d) for a cropped region indicated by dotted lines in 3 (d). Scale bar is $10 \mu\text{m}$.

the SPI reconstructions carry a significant amount of energy from the sample even after a z-displacement of $40 \mu\text{m}$. Hence the MUSSIC approach performs better in rejecting the light out of the image plane.

5.8 Discussion and conclusions

We have demonstrated MUSSIC microscopy through a multimode fiber to enable imaging with optical sectioning, high contrast and improved resolution. Here we limit our experiments to the coherent imaging modality, but the high SNR capability of MUSSIC microscopy paves a feasible path to fluorescence imaging. Calibration of the multispectral TM of scattering media has

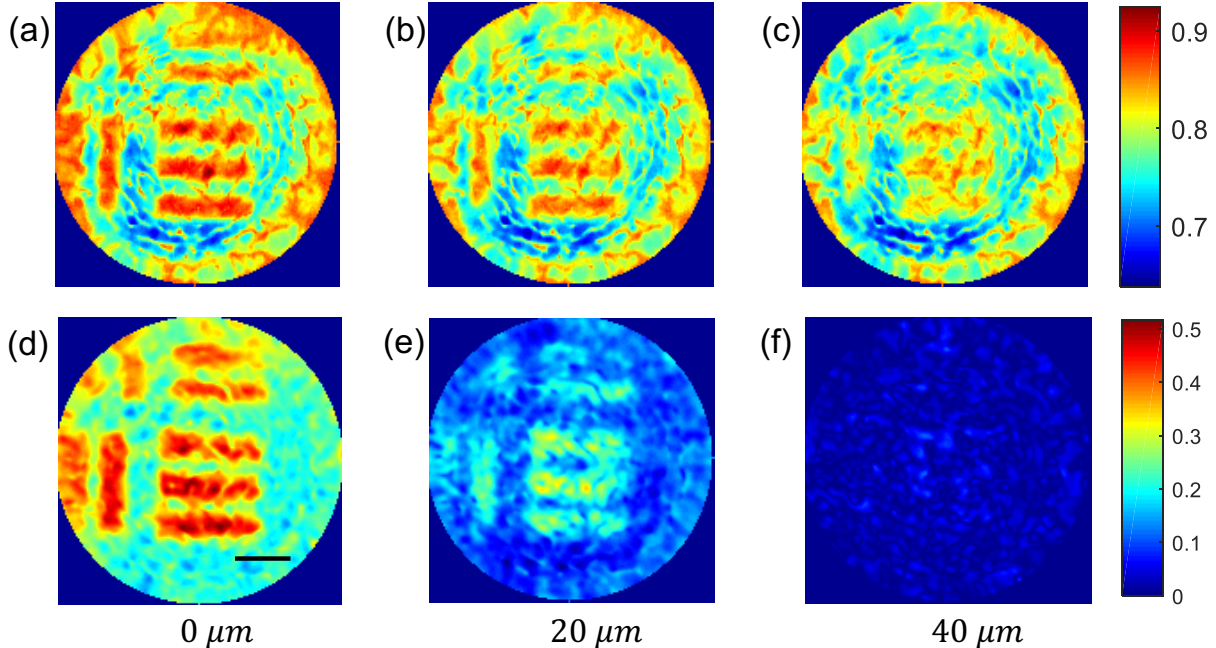


Figure 5.7: Comparison of optical sectioning in MUSSIC microscopy and SPI through multimode fibers. (a, b, c) SPI reconstruction at $z=0, 20$ and $40 \mu\text{m}$ respectively. (d, e, f) MUSSIC reconstruction from 25 pinholes at $z=0, 20$ and $40 \mu\text{m}$ respectively. Postprocessing for the MUSSIC images involved regularized TM inversion, bandpass filtering and normalization, as explained in the methods section. Scale bar is $10 \mu\text{m}$.

been demonstrated in multiple reports [24, 128, 129]. With the help of the multispectral TM, one could for instance, scan multi-spectral focal spots on the proximal side while speckle patterns are projected on the object at the distal end. With knowledge of the distal intensity patterns, the object can be recovered [33, 107]. An advantage of scanning focal spots on the proximal side is that it would eliminate the need for coherent backpropagation and enable imaging by solving a simpler intensity-only inverse problem. We show a factor of 6.2 improvement in the root mean square contrast in MUSSIC images with respect to the raster scan images and a factor of 3.8 improvement with respect to the confocal images. This is however not a fundamental limit and further improvement is possible by increasing the number of confocal images being integrated for the MUSSIC reconstruction and increasing the sampling rate of the distal fields. The cost to pay in exchange is the computational complexity which grows linearly with the number of confocal

images, $N_{pinholes}$.

Besides the challenge of computational complexity, the quality of image reconstruction is limited by several experimental factors. To keep our experimental setup simple and robust to thermal and mechanical fluctuations, we used an internal reference for phase measurements which transform to a non-uniform speckle in the plane of interest with many nulls, also known as blind spots. We are unable to recover the field from these blind spots, which degrade the image reconstruction quality. Using complementary reference speckles [73, 87] or an external plane wave reference are possible ways to eliminate the blind spots, although they either require increased measurement time or a more complex setup with phase tracking to account for phase drifts. Bending sensitivity of the fiber is another challenge and in our experiments the fiber was kept stationary after the forward TM calibration to minimize this effect. Any perturbations after calibration lead to noise in the image reconstruction. Despite these imperfections however, we demonstrate confocal microscopy with improved SNR through a multimode fiber which could be of practical significance for various microscopy applications in scattering media. A further generalization of the technique can be made by choosing distal illuminations that are not focal spots, but arbitrary speckle patterns [107]. In this case, we could calculate the back-propagated distal fields E^d by left multiplying the right-hand side of Eq. 5.7 with the illumination matrix, E^{il} and right multiplying it with the conjugate transpose or Tikhonov regularized inverse of the illumination matrix, E^{il} . The equations are explicitly shown in the Appendix section 2. Speckle illumination is ideal for compressive sampling and can enable imaging with fewer illumination patterns and shorter data acquisition times [33]. Furthermore, it can also eliminate the need for wavefront shaping if a scanning focal spot field is chosen as input, which only requires a focused beam and a steering mechanism.

Overall, our results successfully demonstrate the power of MUSSIC microscopy in enabling high SNR and high-resolution imaging through an endoscope for investigating the deep tissue regime. Given the generalized principle of the technique, its application is not limited to the raster scan approach or to multimode fibers and can easily be adapted to other endoscopic probes that might require different excitation and detection paths such as double-clad fibers.

5.9 Appendix

5.9.1 MUSSIC reconstruction from a system with different excitation and detection PSFs

We described in the main text that when the detection and excitation paths are different, the back-propagated distal fields can be calculated using equation 5. We rewrite the equation here after expanding each term using the definition of calibrated backward TM, T_{obs}^b and the proximal field matrix, E^p in equation 5.9.

$$E^d = (T^b I E^{il})^{RI} T^b O E^{il} \quad (5.9)$$

We have replaced the conjugate transpose of the backward TM above with the Tikhonov regularized inverse. If we define the product, $D_{T^b}^{RI} = (T^b)^{RI} T^b$, as the new diffraction operator, which is similar in structure to the D_T operator defined in the main text, equation 5.9 can be further simplified as shown in equation 5.10.

$$E^d = (E^{il})^{RI} (T^b)^{RI} T^b O E^{il} = (E^{il})^{RI} D_{T^b}^{RI} O E^{il} \quad (5.10)$$

In order to preserve the resolution gain in MUSSIC microscopy, the terms on the left and right of the object should retain the bandwidths of the excitation and detection systems. The right-hand term is the same as in the earlier case of identical excitation and detection PSFs. The left-hand term is the matrix product of the inverse of the illumination matrix and the diffraction operator for the backward transmission matrix, which also has the bandwidth of the detection or the excitation system, whichever is smaller. When the two systems have the same bandwidth, the resolution gain and sectioning properties of MUSSIC microscopy are preserved.

5.9.2 Generalized MUSSIC microscopy using speckle illumination

When the fields illuminating the object are not focal spots, but a set of random speckle patterns, the matrices E^{il} and $(E^{il})^{RI}$ no longer have the structure of the convolution matrix and

their effect has to be reversed digitally by multiplying them with their respective inverse matrices. Eq. 5.11 shows how we can obtain the focal spot equivalent, E^{foc} of the backpropagated distal fields in this case.

$$E^{foc} = E^{il} E^d (E^{il})^{RI} = D_{il}^{RI} D_T^{RI} O D_{il}^{RI} \quad (5.11)$$

where we define $D_{il}^{RI} = E^{il} (E^{il})^{RI}$, as the diffraction operator corresponding the illumination fields. This added computational complexity of $O(N_{out}^2 N_{il})$ can enable imaging with arbitrary speckle illuminations with reduced number of illuminations, when the chosen patterns have small correlations [33, 107]. Even when focused illumination is employed, there is inevitably some energy in the background due to imperfect control over all the fiber modes due to insufficient overlap between the fiber modes and modes of the spatial light modulator (SLM), and thermal and mechanical perturbations. This background is a source of noise in the reconstruction. By measuring the fields corresponding to the distal illuminations, and using the above generalized approach, we can convert the energy in the background into signal and improve the quality of image reconstruction.

5.9.3 Effect of Normalization in image reconstruction

Here we compare the MUSSIC reconstruction made from 25 confocal images before and after normalization with respect to the MUSSIC reconstruction from the proximal fields reflected from the mirror. Figure 1 shows this comparison. We can observe that much of the non-uniformity arising from the speckle reference used for phase measurement, is eliminated as a result of the normalization, yielding a cleaner reconstruction.

5.9.4 MUSSIC Reconstructions using different inversion strategies

Figure 1 (a) and (b) show the MUSSIC reconstructions from 25 confocal images when the conjugate transpose of the backward TM, and its Tikhonov regularized inverse are respectively used to backpropagate to the distal plane. The latter requires computation of the backward TM's singular value decomposition and tuning of the regularization parameter, which is a time-consuming process. On the other hand, the conjugate transpose is computed almost instantaneously and

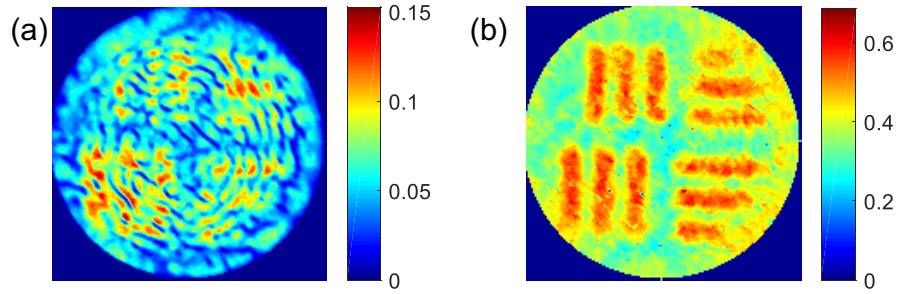


Figure 5.8: Effect of normalization on image reconstruction. (a) MUSEC reconstruction from 25 confocal images without normalization. (b) MUSEC reconstruction in (a) normalized by the MUSEC reconstruction corresponding to the proximal fields reflected from the mirror during the backward TM calibration.

allows MUSEC reconstruction (with normalization) within 2.6 minutes using 9 confocal images and within 5 minutes using 25 confocal images. Although the result from Tikhonov regularization is significantly better, the conjugate transpose also provides a good estimate of the object.

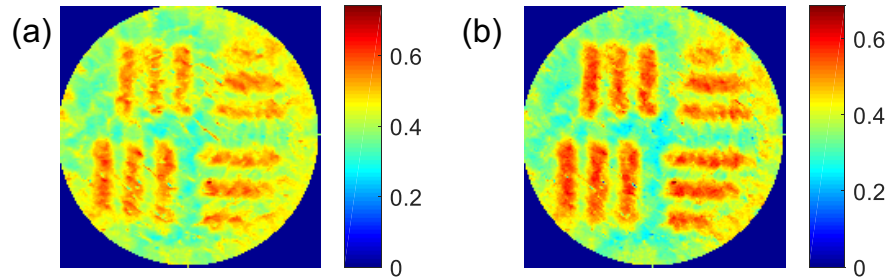


Figure 5.9: Comparison of MUSEC reconstructions using different inverse estimates of the backward TM. (a) MUSEC recovery from 25 confocal images by assuming the inverse of the backward TM to be its conjugate transpose matrix. (b) MUSEC recovery from 25 confocal images using the Tikhonov regularized inverse of the backward TM with $\beta = 10\%$ of its highest singular value.

Chapter 6

Summary, future work and outlook

6.1 Summary

This Thesis demonstrates key methodologies for advancing the multimode fiber imaging technology and applying it for minimally invasive endoscopy. With the highest bandwidth in the smallest possible footprint, MMF make ideal candidates for endoscopy and have the potential to achieve the same functionality as a bulky microscope objective. Here, we take a few steps closer to this goal by improving the speed, robustness, resolution and optical sectioning in MMF imaging.

In Chapter 2, we demonstrated speckle imaging through MMFs, which eliminates the need for coherent control and enables imaging through MMFs, using the naturally occurring random speckle patterns at the distal end. The technique requires a simpler, intensity-only calibration hence overcoming the issue of blind spots due to the speckle reference and requires a fewer number of measurements than that required for a raster scan approach. We show a 13 times compression in the number of measurements while minimally compromising the image quantity with the help of an optimization algorithm that minimizes the correlations between the speckle pattern used for the reconstruction. We demonstrate imaging of $4\mu\text{m}$ fluorescent beads as well as retrobeads embedded in the brain slice of a mouse. Finally, we also demonstrate hybrid photo-acoustic and fluorescence microscopy using a multimode fiber by adding an adjacent single mode fiber to collect the photoacoustic signal.

In Chapter 3, we propose the use of a 1D wavefront modulator called a grating light valve for wavefront shaping at 350 kHz. We demonstrate real-time and continuous calibration and focusing

through scattering media such as ground glass diffusers and multimode fibers, within 2.4 ms. We also demonstrate the fast refocusing capability of the GLV by focusing through rapidly changing dynamic media. Moreover, we analyze the dependence of the scatterer thickness and different illumination configurations on the far field speckle shape by modelling a thin scatterer exhibiting memory effect. With the help of this model, we determine the suitable illumination configuration on the scatterer to achieve full 2D control over the field after the scattering media, using the 1D GLV.

In Chapter 4, we demonstrate mode control in the fiber mode basis by exciting Hadamard functions at the input and generating focal spots at the output as an example. As opposed to conventional mode control techniques which excite and generate pure modes and are feasible only for few-mode fibers, our technique is scalable to myriad mode fibers and allows generation of complex fiber mode combinations via a digital basis transformation. We define various metrics to evaluate the mode control and demonstrate their dependence on the spatial location of the focal spots across the fiber cross-section. We also compare the bend resilience of different mode groups in the fiber by creating mode controlled focal spots and find that modes with higher orbital angular momentum are more resilient to bends.

Finally, in Chapter 5, we demonstrated a technique to achieve optical sectioning and improved resolution through multimode fibers while maintaining a good signal to noise ratio. We present the theory for the gain in resolution and optical sectioning when imaging through a multimode fiber and demonstrate proof-of concept imaging of the USAF test target. We also show that the technique is feasible when the detection and excitation paths are separate and when the scanning illuminations are arbitrary speckle patterns instead of focal spots.

6.2 Future Work

6.2.1 Improving speed and SNR in speckle imaging through Multimode fibers

In our work on imaging using random speckle patterns, the imaging speed of the system was limited by the wavefront shaping modulator. This technique however does not necessarily require a wavefront shaping modulator and faster alternatives such as galvanometric mirrors and acousto-optic deflectors can be employed to generate random speckle patterns at relatively faster speeds.

Although using speckle patterns enables imaging with fewer measurements and eliminates the need for wavefront shaping, these benefits come at the cost of a lower signal-to-noise ratio (SNR). A desired trade-off between the SNR and the compression can be achieved by employing focal spots with some background speckle to scan the object. The ratio of the focal spot intensity and the background speckle intensity can be varied to directly control the SNR and compression trade-off. These hybrid illumination patterns are also easy to generate and require fewer phase control pixels relative to the number of fiber modes. They are hence more feasible for implementation using a Grating Light Valve (GLV), which has a limited number of phase control pixels, but a much faster modulation speed. Future work could implement speckle imaging through MMFs using a GLV and employ hybrid speckle patterns as described above. This could improve the SNR, imaging frame rate, and provide a robust system suitable for imaging applications that require high temporal resolutions such as real-time calcium imaging.

6.2.2 Towards high SNR fluorescence imaging with optical sectioning through MMFs

We demonstrated MUSSIC microscopy through an MMF to achieve high-SNR confocal imaging in the reflection mode. Extending the technique to fluorescence mode is desirable to visualize specific regions of the tissue. Towards this end, we can calibrate the multispectral TM of the MMF [24, 128, 129]. Recently, simultaneous spatio-temporal calibration of the multi-spectral TM using

only spatial degrees of freedom was demonstrated by spatially separating out the different color bands using a microlens array and diffraction grating [24]. Using a similar approach, but with the same continuous wave laser used in our system, the fiber’s double-pass multispectral TM can be measured from the SLM to the proximal camera while a bright florescent screen is placed on the distal side.

With the help of the multispectral TM, one could, for instance, scan multi-spectral focal spots on the proximal side while speckle patterns are projected on the object at the distal end. With knowledge of the distal intensity patterns, the object can be recovered [33, 107]. An advantage of scanning focal spots on the proximal side is that it would eliminate the need for coherent back-propagation and enable imaging by solving a simpler intensity-only inverse problem.

6.2.3 Faster MUSSIC microscopy and better reconstruction algorithm

In our work on MUSSIC microscopy, we employed the classic pixel reassignment algorithm. While, effective, it does not achieve the best possible resolution gain. Better reconstruction algorithm such as a multi-view maximum likelihood deconvolution [154] can be adapted to shift variant systems and employed to improve the lateral resolution and optical sectioning in MMF imaging. Moreover, the imaging speed in MUSSIC microscopy is limited by the proximal camera speed instead of the wavefront shaper. Use of fast SPAD arrays or multi-pixel photomultiplier tubes in conjunction with the GLV can enable faster imaging speeds.

6.2.4 Deep learning for learning the multimode fiber model

The image quality in MMF imaging is critically dependent on how accurately the measured transmission matrix (TM) models the MMF. Currently, the TM is measured by a calibration approach requiring thousands of coherent measurements. Moreover, this TM describes a specific stationary state of the MMF and can change when the MMF is subject to mechanical or thermal perturbations.

Deep learning is emerging as a powerful tool for modelling complex systems and could be used

to simplify MMF imaging systems. Recent work on retrieving the input images using the output amplitude [150] or intensity patterns [25], or vice versa [56], controlling the output pattern using only amplitude measurements [149], characterizing ultrafast pulses through multimode fibers [188], controlling non-linearities [174], mode decomposition [9, 156], predicting input patterns transmitted through an MMF with continuously varying shape [57], and predicting the bend configuration using output speckle patterns [112] show great promise in the potential of deep learning for simplifying MMF. A particularly interesting deep learning application would be for bend correction without distal access using reflected speckle patterns as feedback.

6.2.5 Towards in-vivo microscopy with deep penetration in live animals

Finally, further work must be done to implement our methods with improved speed, SNR, optical sectioning and robustness, in an in-vivo environment to perform calcium imaging. This would involve a robust optical design with suitable accommodation for a live animal and designing a mechanism for implanting the endoscope in the site of interest. Further along this direction, it would be interesting to explore the potential of MMFs for deeper penetration by performing in-vivo experiments in bigger organisms like primates.

6.3 Outlook

Within the short span of a decade, the realm of applications of multimode fibers has expanded beyond optical communication to a vast range of fields such as endoscopy, sensing, manipulation, energy delivery, quantum key distribution and computation. However, we have only just begun to scratch the surface of possibilities with MMFs and more exciting times lie ahead.

Armed with high-speed wavefront shaping tools and techniques to achieve optical sectioning and better resolution in imaging through MMFs, it would be interesting to explore their applications not just for in-vivo calcium imaging, but also for optogenetic stimulation targeting specific molecules. Given their micron-scale resolution sufficient to resolve individual neurons and their potential to target specific neurons using genetically encoded markers, MMFs could cause a signif-

icant impact in the field of deep brain stimulation over more invasive and lower resolution, electrophysiological and other electrical signal-based brain stimulation tools, especially for applications requiring deep tissue penetration beyond the millimeter scale.

A significant challenge that must be countered to enable the MMF endoscopy technology is to solve the problem of bend and motion sensitivity of MMFs. While various interesting approaches have been proposed, a fast and robust mechanism that would enable correction for the changing transmission matrix of a bending MMF is desired, and could hold the key to realizing the various proposed endoscopic applications. An idea worth exploring is to employ a feedback mechanism to track the changing TM such as back-reflected speckle patterns.

In working towards the goal of building a minimally invasive MMF endoscope that could replace a microscope objective, exploring novel MMF designs is also an interesting research avenue. Thus far, telecommunication fibers are largely employed in various experiments for MMF imaging, sensing, manipulation etc., which do not necessarily possess optimal dispersion properties, non-linear response, peak-power tolerance, bend sensitivity or even geometrical design. It would be interesting to see how customization of MMF designs could help improve their performance in different applications.

Overall, this is an exciting time for MMF research, characterized by continuous advances. With further efforts, it is only a matter of time before MMFs will be enabling linear and non-linear in-vivo endoscopic applications in various body organs.

Bibliography

- [1] Min Ai, Weihang Shu, Tim Salcudean, Robert Rohling, Purang Abolmaesumi, and Shuo Tang. Design of high energy laser pulse delivery in a multimode fiber for photoacoustic tomography. Optics express, 25(15):17713–17726, 2017.
- [2] Duygu Akbulut, Thomas J Huisman, Elbert G van Putten, Willem L Vos, and Allard P Mosk. Focusing light through random photonic media by binary amplitude modulation. Optics express, 19(5):4017–4029, 2011.
- [3] Walter J Akers, Chulhong Kim, Mikhail Berezin, Kevin Guo, Ralph Fuhrhop, Gregory M Lanza, Georg M Fischer, Ewald Daltrozzo, Andreas Zumbusch, Xin Cai, et al. Noninvasive photoacoustic and fluorescence sentinel lymph node identification using dye-loaded perfluorocarbon nanoparticles. ACS nano, 5(1):173–182, 2010.
- [4] Milad I Akhlaghi and Aristide Dogariu. Compressive correlation imaging with random illumination. Optics letters, 40(19):4464–4467, 2015.
- [5] Lyubov V Amitonova and Johannes F De Boer. Compressive imaging through a multimode fiber. Optics letters, 43(21):5427–5430, 2018.
- [6] Lyubov V Amitonova and Johannes F de Boer. Endo-microscopy beyond the abbe and nyquist limits. Light: Science & Applications, 9(1):1–12, 2020.
- [7] Lyubov V Amitonova, Tristan BH Tentrup, Ivo M Vellekoop, and Pepijn WH Pinkse. Method for quantum key establishment through a multimode fiber. In European Quantum Electronics Conference, page eb_p-19. Optical Society of America, 2019.
- [8] A. Amphawan and D. O’Brien. Holographic mode field generation for a multimode fiber channel. In International Conference On Photonics 2010, pages 1–4, July 2010.
- [9] Yi An, Liangjin Huang, Jun Li, Jinyong Leng, Lijia Yang, and Pu Zhou. Deep learning-based real-time mode decomposition for multimode fibers. IEEE Journal of Selected Topics in Quantum Electronics, 26(4):1–6, 2020.
- [10] DZ Anderson, MA Bolshtyansky, and B Ya Zel’dovich. Stabilization of the speckle pattern of a multimode fiber undergoing bending. Optics letters, 21(11):785–787, 1996.
- [11] Esben Ravn Andresen, Siddharth Sivankutty, Viktor Tsvirkun, Géraud Bouwmans, and Hervé Rigneault. Ultrathin endoscopes based on multicore fibers and adaptive optics: a status review and perspectives. Journal of biomedical optics, 21(12):121506, 2016.

- [12] Roman Barankov and Jerome Mertz. High-throughput imaging of self-luminous objects through a single optical fibre. Nature communications, 5(1):1–6, 2014.
- [13] Robert PJ Barretto, Bernhard Messerschmidt, and Mark J Schnitzer. In vivo fluorescence imaging with high-resolution microlenses. Nature methods, 6(7):511, 2009.
- [14] Amir Beck and Marc Teboulle. A fast iterative shrinkage-thresholding algorithm for linear inverse problems. SIAM journal on imaging sciences, 2(1):183–202, 2009.
- [15] Claude Belleville and Gaetan Duplain. White-light interferometric multimode fiber-optic strain sensor. Optics letters, 18(1):78–80, 1993.
- [16] F Benabid. Hollow-core photonic crystal fibers: guidances and applications. In Specialty Optical Fibers, pages SoM4B–5. Optical Society of America, 2014.
- [17] Richard KP Benninger and David W Piston. Two-photon excitation microscopy for the study of living cells and tissues. Current protocols in cell biology, 59(1):4–11, 2013.
- [18] S Berdagué and P Facq. Mode division multiplexing in optical fibers. Applied optics, 21(11):1950–1955, 1982.
- [19] M Bertero, P Brianzi, and ER Pike. Super-resolution in confocal scanning microscopy. Inverse Problems, 3(2):195, 1987.
- [20] Mario Bertero, Paola Brianzi, Pat Parker, and ER Pike. Resolution in diffraction-limited imaging, a singular value analysis. Optica Acta: International Journal of Optics, 31(2):181–201, 1984.
- [21] Silvio Bianchi, VP Rajamanickam, Lorenzo Ferrara, E Di Fabrizio, Carlo Liberale, and Roberto Di Leonardo. Focusing and imaging with increased numerical apertures through multimode fibers with micro-fabricated optics. Optics letters, 38(23):4935–4938, 2013.
- [22] Baptiste Blochet, Laurent Bourdieu, and Sylvain Gigan. Focusing light through dynamical samples using fast continuous wavefront optimization. Optics letters, 42(23):4994–4997, 2017.
- [23] Maxim A Bolshtyansky and Boris Ya Zel’dovich. Transmission of the image signal with the use of a multimode fiber. Optics communications, 123(4-6):629–636, 1996.
- [24] Antoine Boniface, Ivan Gusachenko, Kishan Dholakia, and Sylvain Gigan. Rapid broadband characterization of scattering medium using hyperspectral imaging. Optica, 6(3):274–279, 2019.
- [25] Navid Borhani, Eirini Kakkava, Christophe Moser, and Demetri Psaltis. Learning to see through multimode fibers. Optica, 5(8):960–966, 2018.
- [26] Ronald E Bruck Jr. On the weak convergence of an ergodic iteration for the solution of variational inequalities for monotone operators in hilbert space. Journal of Mathematical Analysis and Applications, 61(1):159–164, 1977.
- [27] Sophie Brustlein, Pascal Berto, Richard Hostein, Patrick Ferrand, Cyrille Billaudeau, Didier Marguet, Alistair Muir, Jonathan Knight, and Hervé Rigneault. Double-clad hollow core photonic crystal fiber for coherent raman endoscope. Optics express, 19(13):12562–12568, 2011.

- [28] Elizabeth A Calle, Sam Vesuna, Sashka Dimitrievska, Kevin Zhou, Angela Huang, Liping Zhao, Laura E Niklason, and Michael J Levene. The use of optical clearing and multiphoton microscopy for investigation of three-dimensional tissue-engineered constructs. Tissue Engineering Part C: Methods, 20(7):570–577, 2014.
- [29] Emmanuel J Candès and Michael B Wakin. An introduction to compressive sampling. IEEE signal processing magazine, 25(2):21–30, 2008.
- [30] Antonio M Caravaca-Aguirre, Eyal Niv, Donald B Conkey, and Rafael Piestun. Real-time resilient focusing through a bending multimode fiber. Optics express, 21(10):12881–12887, 2013.
- [31] Antonio M Caravaca-Aguirre, Eyal Niv, and Rafael Piestun. High-speed phase modulation for multimode fiber endoscope. In Imaging Systems and Applications, pages ITh3C–1. Optical Society of America, 2014.
- [32] Antonio M Caravaca-Aguirre and Rafael Piestun. Single multimode fiber endoscope. Optics express, 25(3):1656–1665, 2017.
- [33] Antonio M Caravaca-Aguirre, Sakshi Singh, Simon Labouesse, Michael V Baratta, Rafael Piestun, and Emmanuel Bossy. Hybrid photoacoustic-fluorescence microendoscopy through a multimode fiber using speckle illumination. APL Photonics, 4(9):096103, 2019.
- [34] Joel Carpenter, Benjamin J Eggleton, and Jochen Schröder. 110x110 optical mode transfer matrix inversion. Optics express, 22(1):96–101, 2014.
- [35] Joel Carpenter, Benjamin J Eggleton, and Jochen Schröder. Observation of eisenbud–wigner–smith states as principal modes in multimode fibre. Nature Photonics, 9(11):751–757, 2015.
- [36] Joel Carpenter, Benn C Thomsen, and Timothy D Wilkinson. Degenerate mode-group division multiplexing. Journal of Lightwave Technology, 30(24):3946–3952, 2012.
- [37] Joel Carpenter and Timothy D Wilkinson. Characterization of multimode fiber by selective mode excitation. Journal of lightwave technology, 30(10):1386–1392, 2012.
- [38] Antonin Chambolle, Ronald A De Vore, Nam-Yong Lee, and Bradley J Lucier. Nonlinear wavelet image processing: variational problems, compression, and noise removal through wavelet shrinkage. IEEE Transactions on Image Processing, 7(3):319–335, 1998.
- [39] Youngwoon Choi, Changhyeong Yoon, Moonseok Kim, Juhee Yang, and Wonshik Choi. Disorder-mediated enhancement of fiber numerical aperture. Optics letters, 38(13):2253–2255, 2013.
- [40] Youngwoon Choi, Changhyeong Yoon, Moonseok Kim, Taeseok Daniel Yang, Christopher Fang-Yen, Ramachandra R Dasari, Kyoung Jin Lee, and Wonshik Choi. Scanner-free and wide-field endoscopic imaging by using a single multimode optical fiber. Physical review letters, 109(20):203901, 2012.
- [41] Tomáš Čižmár and Kishan Dholakia. Exploiting multimode waveguides for pure fibre-based imaging. Nature communications, 3(1):1–9, 2012.

- [42] Patrick L Combettes and Jean-Christophe Pesquet. Proximal splitting methods in signal processing. In Fixed-point algorithms for inverse problems in science and engineering, pages 185–212. Springer, 2011.
- [43] Donald B Conkey, Antonio M Caravaca-Aguirre, and Rafael Piestun. High-speed scattering medium characterization with application to focusing light through turbid media. Optics express, 20(2):1733–1740, 2012.
- [44] Donald B Conkey, Nicolino Stasio, Edgar E Morales-Delgado, Marilisa Romito, Christophe Moser, and Demetri Psaltis. Lensless two-photon imaging through a multicore fiber with coherence-gated digital phase conjugation. Journal of Biomedical Optics, 21(4):045002, 2016.
- [45] Ingrid Daubechies, Michel Defrise, and Christine De Mol. An iterative thresholding algorithm for linear inverse problems with a sparsity constraint. Communications on Pure and Applied Mathematics: A Journal Issued by the Courant Institute of Mathematical Sciences, 57(11):1413–1457, 2004.
- [46] Philip J Davis. Circulant matrices. American Mathematical Soc., 2013.
- [47] Hilton B de Aguiar, Sylvain Gigan, and Sophie Brasselet. Polarization recovery through scattering media. Science Advances, 3(9):e1600743, 2017.
- [48] X Luís Deán-Ben, Gali Sela, Antonella Lauri, Moritz Kneipp, Vasilis Ntziachristos, Gil G Westmeyer, Shy Shoham, and Daniel Razansky. Functional optoacoustic neuro-tomography for scalable whole-brain monitoring of calcium indicators. Light: Science & Applications, 5(12):e16201, 2016.
- [49] Hugo Defienne, Marco Barbieri, Ian A Walmsley, Brian J Smith, and Sylvain Gigan. Two-photon quantum walk in a multimode fiber. Science advances, 2(1):e1501054, 2016.
- [50] Sunan Deng, Damien Loterie, Georgia Konstantinou, Demetri Psaltis, and Christophe Moser. Raman imaging through multimode sapphire fiber. Optics express, 27(2):1090–1098, 2019.
- [51] Winfried Denk, James H Strickler, and Watt W Webb. Two-photon laser scanning fluorescence microscopy. Science, 248(4951):73–76, 1990.
- [52] Roberto Di Leonardo and Silvio Bianchi. Hologram transmission through multi-mode optical fibers. Optics express, 19(1):247–254, 2011.
- [53] Angélique Drémeau, Antoine Liutkus, David Martina, Ori Katz, Christophe Schülke, Florent Krzakala, Sylvain Gigan, and Laurent Daudet. Reference-less measurement of the transmission matrix of a highly scattering material using a dmd and phase retrieval techniques. Optics express, 23(9):11898–11911, 2015.
- [54] Marco F Duarte, Mark A Davenport, Dharmpal Takhar, Jason N Laska, Ting Sun, Kevin F Kelly, and Richard G Baraniuk. Single-pixel imaging via compressive sampling. IEEE signal processing magazine, 25(2):83–91, 2008.
- [55] P Facq, P Fournet, and J Arnaud. Observation of tubular modes in multimode graded-index optical fibres. Electronics Letters, 16(17):648–650, 1980.

- [56] Pengfei Fan, Liang Deng, and Lei Su. Light propagation prediction through multimode optical fibers with a deep neural network. In 2018 IEEE 3rd Advanced Information Technology, Electronic and Automation Control Conference (IAEAC), pages 1080–1084. IEEE, 2018.
- [57] Pengfei Fan, Tianrui Zhao, and Lei Su. Deep learning the high variability and randomness inside multimode fibers. Optics express, 27(15):20241–20258, 2019.
- [58] Salma Farahi, David Ziegler, Ioannis N Papadopoulos, Demetri Psaltis, and Christophe Moser. Dynamic bending compensation while focusing through a multimode fiber. Optics express, 21(19):22504–22514, 2013.
- [59] Yousef Fazea and Vitaliy Mezhuyev. Selective mode excitation techniques for mode-division multiplexing: A critical review. Optical Fiber Technology, 45:280–288, 2018.
- [60] Daniel Feldkhun, Omer Tzang, Kelvin H Wagner, and Rafael Piestun. Focusing and scanning through scattering media in microseconds. Optica, 6(1):72–75, 2019.
- [61] Shechao Feng, Charles Kane, Patrick A Lee, and A Douglas Stone. Correlations and fluctuations of coherent wave transmission through disordered media. Physical review letters, 61(7):834, 1988.
- [62] Xinhuan Feng, Hwa-yaw Tam, Weng-hong Chung, and PKA Wai. Multiwavelength fiber lasers based on multimode fiber bragg gratings using offset launch technique. Optics communications, 263(2):295–299, 2006.
- [63] Mário AT Figueiredo and Robert D Nowak. An em algorithm for wavelet-based image restoration. IEEE Transactions on Image Processing, 12(8):906–916, 2003.
- [64] John M Fini and Siddharth Ramachandran. Natural bend-distortion immunity of higher-order-mode large-mode-area fibers. Optics letters, 32(7):748–750, 2007.
- [65] Dirk E Boonzajer Flaes, Jan Stopka, Sergey Turtaev, Johannes F De Boer, Tomáš Tyc, and Tomáš Čižmár. Robustness of light-transport processes to bending deformations in graded-index multimode waveguides. Physical review letters, 120(23):233901, 2018.
- [66] Benjamin A Flusberg, Eric D Cocker, Wibool Piyawattanametha, Juergen C Jung, Eunice LM Cheung, and Mark J Schnitzer. Fiber-optic fluorescence imaging. Nature methods, 2(12):941–950, 2005.
- [67] Bernd Franz and Henning Bulow. Experimental evaluation of principal mode groups as high-speed transmission channels in spatial multiplex systems. IEEE photonics technology letters, 24(16):1363–1365, 2012.
- [68] Isaac Freund, Michael Rosenbluh, and Shechao Feng. Memory effects in propagation of optical waves through disordered media. Physical review letters, 61(20):2328, 1988.
- [69] AA Friesem, Uri Levy, and Yaron Silberberg. Parallel transmission of images through single optical fibers. Proceedings of the IEEE, 71(2):208–221, 1983.
- [70] Ling Fu, Ankur Jain, Huikai Xie, Charles Cranfield, and Min Gu. Nonlinear optical endoscopy based on a double-clad photonic crystal fiber and a mems mirror. Optics Express, 14(3):1027–1032, 2006.

- [71] Liang Gao, Chi Zhang, Chiye Li, and Lihong V Wang. Intracellular temperature mapping with fluorescence-assisted photoacoustic-thermometry. Applied Physics Letters, 102(19):193705, 2013.
- [72] OV Garibyan, IN Kompanets, AV Parfyonov, NF Pilipetsky, VV Shkunov, AN Sudarkin, AV Sukhov, NV Tabiryan, AA Vasiliev, and B Ya Zel'dovich. Optical phase conjugation by microwatt power of reference waves via liquid crystal light valve. Optics Communications, 38(1):67–70, 1981.
- [73] Jérôme Gateau, Hervé Rigneault, and Marc Guillon. Complementary speckle patterns: deterministic interchange of intrinsic vortices and maxima through scattering media. Physical Review Letters, 118(4):043903, 2017.
- [74] Snir Gazit, Alexander Szameit, Yonina C Eldar, and Mordechai Segev. Super-resolution and reconstruction of sparse sub-wavelength images. Optics express, 17(26):23920–23946, 2009.
- [75] D Gloge and EAJ Marcatili. Impulse response of fibers with ring-shaped parabolic index distribution. The Bell System Technical Journal, 52(7):1161–1168, 1973.
- [76] D Gloge and EAJ Marcatili. Multimode theory of graded-core fibers. Bell System Technical Journal, 52(9):1563–1578, 1973.
- [77] Salvador González and Zeina Tannous. Real-time, in vivo confocal reflectance microscopy of basal cell carcinoma. Journal of the American Academy of Dermatology, 47(6):869–874, 2002.
- [78] George SD Gordon, Milana Gataric, Alberto Gil CP Ramos, Ralf Mouthaan, Calum Williams, Jonghee Yoon, Timothy D Wilkinson, and Sarah E Bohndiek. Characterizing optical fiber transmission matrices using metasurface reflector stacks for lensless imaging without distal access. Physical Review X, 9(4):041050, 2019.
- [79] A Gover, CP Lee, and A Yariv. Direct transmission of pictorial information in multimode optical fibers. JOSA, 66(4):306–311, 1976.
- [80] A Gover, CP Lee, and A Yariv. f gs gsgss gs ggggs (2). J. Opt. Soc. Am, 66(4), 1976.
- [81] P Gregg, P Kristensen, and S Ramachandran. Conservation of orbital angular momentum in air-core optical fibers. Optica, 2(3):267–270, 2015.
- [82] Ruo Yu Gu, Elaine Chou, Cory Rewcastle, Ofer Levi, and Joseph M Kahn. Improved spot formation for flexible multi-mode fiber endoscope using partial reflector. arXiv preprint arXiv:1805.07553, 2018.
- [83] Ruo Yu Gu, Reza Nasiri Mahalati, and Joseph M Kahn. Design of flexible multi-mode fiber endoscope. Optics express, 23(21):26905–26918, 2015.
- [84] Stéphanie Guérit, Siddharth Sivankutty, Camille Scotté, John Alto Lee, Hervé Rigneault, and Laurent Jacques. Compressive sampling approach for image acquisition with lensless endoscope. arXiv preprint arXiv:1810.12286, 2018.
- [85] Andrew G Hallam. Mode control in multimode optical fibre and its applications. PhD thesis, Aston University, 2007.

- [86] Jae-Ho Han, Junghoon Lee, and Jin U Kang. Pixelation effect removal from fiber bundle probe based optical coherence tomography imaging. Optics express, 18(7):7427–7439, 2010.
- [87] Matthias Hofer and Sophie Brasselet. Manipulating the transmission matrix of scattering media for nonlinear imaging beyond the memory effect. Optics letters, 44(9):2137–2140, 2019.
- [88] Erich E Hoover and Jeff A Squier. Advances in multiphoton microscopy technology. Nature photonics, 7(2):93–101, 2013.
- [89] Pei-Lin Hsiung, Jonathan Hardy, Shai Friedland, Roy Soetikno, Christine B Du, Amy P Wu, Peyman Sahbaie, James M Crawford, Anson W Lowe, Christopher H Contag, et al. Detection of colonic dysplasia in vivo using a targeted heptapeptide and confocal microendoscopy. Nature medicine, 14(4):454–458, 2008.
- [90] Rick CJ Hsu, Alireza Tarighat, Akhil Shah, Ali H Sayed, and Bahram Jalali. Capacity enhancement in coherent optical mimo (comimo) multimode fiber links. IEEE Communications letters, 10(3):195–197, 2006.
- [91] Song Hu. Listening to the brain with photoacoustics. IEEE Journal of Selected Topics in Quantum Electronics, 22(3):117–126, 2016.
- [92] Jonathan D Ingham, Richard V Penty, and Ian H White. Bidirectional multimode-fiber communication links using dual-purpose vertical-cavity devices. Journal of lightwave technology, 24(3):1283, 2006.
- [93] I Jalbert, F Stapleton, E Papas, DF Sweeney, and M Coroneo. In vivo confocal microscopy of the human cornea. British Journal of Ophthalmology, 87(2):225–236, 2003.
- [94] Pierre Jobez, Nuala Timoney, Cyril Laplane, Jean Etesse, Alban Ferrier, Philippe Goldner, Nicolas Gisin, and Mikael Afzelius. Towards highly multimode optical quantum memory for quantum repeaters. Physical Review A, 93(3):032327, 2016.
- [95] Benjamin Judkewitz, Roarke Horstmeyer, Ivo M Vellekoop, Ioannis N Papadopoulos, and Changhui Yang. Translation correlations in anisotropically scattering media. Nature physics, 11(8):684–689, 2015.
- [96] Peter Kairouz and Andrew Singer. Mimo communications over multi-mode optical fibers: Capacity analysis and input-output coupling schemes. arXiv preprint arXiv:1304.0422, 2013.
- [97] Eirini Kakkava, Marilisa Romito, Donald B Conkey, Damien Loterie, Konstantina M Stankovic, Christophe Moser, and Demetri Psaltis. Selective femtosecond laser ablation via two-photon fluorescence imaging through a multimode fiber. Biomedical optics express, 10(2):423–433, 2019.
- [98] Ori Katz, Yaron Bromberg, and Yaron Silberberg. Compressive ghost imaging. Applied Physics Letters, 95(13):131110, 2009.
- [99] Ralf Kiesslich, Juergen Burg, Michael Vieth, Janina Gnaendiger, Meike Enders, Peter Delaney, Adrian Polglase, Wendy McLaren, Daniela Janell, Steven Thomas, et al. Confocal laser endoscopy for diagnosing intraepithelial neoplasias and colorectal cancer in vivo. Gastroenterology, 127(3):706–713, 2004.

- [100] Ralf Kiesslich, Martin Goetz, Juergen Burg, Manfred Stolte, Ekkehard Siegel, Markus J Maeurer, Steven Thomas, Dennis Strand, Peter R Galle, and Markus F Neurath. Diagnosing helicobacter pylori in vivo by confocal laser endoscopy. Gastroenterology, 128(7):2119–2123, 2005.
- [101] Chulhong Kim, Kwang Hyun Song, Feng Gao, and Lihong V Wang. Sentinel lymph nodes and lymphatic vessels: noninvasive dual-modality in vivo mapping by using indocyanine green in rats—volumetric spectroscopic photoacoustic imaging and planar fluorescence imaging. Radiology, 255(2):442–450, 2010.
- [102] Jonathan C Knight. Photonic crystal fibres. nature, 424(6950):847–851, 2003.
- [103] Demirhan Kobat, Michael E Durst, Nozomi Nishimura, Angela W Wong, Chris B Schaffer, and Chris Xu. Deep tissue multiphoton microscopy using longer wavelength excitation. Optics express, 17(16):13354–13364, 2009.
- [104] Simon Labouesse, Sakshi Singh, and Rafael Piestun. Random speckle illumination patterns for compressed imaging through a multimode fiber, 2018. Oral presentation at EOS Waves in Complex Photonics Media, Anacapri.
- [105] Mingying Lan, Di Guan, Li Gao, Junhui Li, Song Yu, and Guohua Wu. Robust compressive multimode fiber imaging against bending with enhanced depth of field. Optics express, 27(9):12957–12962, 2019.
- [106] Gregoire PJ Laporte, Nicolino Stasio, Christophe Moser, and Demetri Psaltis. Enhanced resolution in a multimode fiber imaging system. Optics express, 23(21):27484–27493, 2015.
- [107] Szu-Yu Lee, Brett Bouma, and Martin Villiger. Confocal imaging through a multimode fiber without active wave-control. In 2019 IEEE Photonics Conference (IPC), pages 1–2. IEEE.
- [108] WM Lee and SH Yun. Adaptive aberration correction of grin lenses for confocal endomicroscopy. Optics letters, 36(23):4608–4610, 2011.
- [109] Saroch Leedumrongwatthanakun, Luca Innocenti, Hugo Defienne, Thomas Juffmann, Alessandro Ferraro, Mauro Paternostro, and Sylvain Gigan. Programmable linear quantum networks with a multimode fibre. Nature Photonics, 14(3):139–142, 2020.
- [110] Shuhui Li, Simon AR Horsley, Tomas Tyc, Tomas Cizmar, and David B Phillips. Guide-star assisted imaging through multimode optical fibres. arXiv preprint arXiv:2005.06445, 2020.
- [111] Yan Liu, Puxiang Lai, Cheng Ma, Xiao Xu, Alexander A Grabar, and Lihong V Wang. Optical focusing deep inside dynamic scattering media with near-infrared time-reversed ultrasonically encoded (true) light. Nature communications, 6(1):1–9, 2015.
- [112] Yan Liu, Guangde Li, Qi Qin, Zhongwei Tan, Muguang Wang, and Fengping Yan. Bending recognition based on the analysis of fiber specklegrams using deep learning. Optics & Laser Technology, 131:106424, 2020.
- [113] Yan Liu, Cheng Ma, Yuecheng Shen, Junhui Shi, and Lihong V Wang. Focusing light inside dynamic scattering media with millisecond digital optical phase conjugation. Optica, 4(2):280–288, 2017.

- [114] Yu Liu and Li Wei. Low-cost high-sensitivity strain and temperature sensing using graded-index multimode fibers. *Applied optics*, 46(13):2516–2519, 2007.
- [115] W Löffler, TG Euser, ER Eliel, M Scharrer, P St J Russell, and JP Woerdman. Fiber transport of spatially entangled photons. *Physical review letters*, 106(24):240505, 2011.
- [116] Alberto Lombardini, Vasyl Mytskaniuk, Siddharth Sivankutty, Esben Ravn Andresen, Xueqin Chen, Jérôme Wenger, Marc Fabert, Nicolas Joly, Frédéric Louradour, Alexandre Kudlinski, et al. High-resolution multimodal flexible coherent raman endoscope. *Light: Science & Applications*, 7(1):1–8, 2018.
- [117] Damien Loterie, Salma Farahi, Ioannis Papadopoulos, Alexandre Goy, Demetri Psaltis, and Christophe Moser. Digital confocal microscopy through a multimode fiber. *Optics express*, 23(18):23845–23858, 2015.
- [118] Damien Loterie, Sebastianus A Goorden, Demetri Psaltis, and Christophe Moser. Confocal microscopy through a multimode fiber using optical correlation. *Optics letters*, 40(24):5754–5757, 2015.
- [119] Damien Loterie, Demetri Psaltis, and Christophe Moser. Bend translation in multimode fiber imaging. *Optics express*, 25(6):6263–6273, 2017.
- [120] Azusa Maeda, Jiachuan Bu, Juan Chen, Gang Zheng, and Ralph S DaCosta. Dual in vivo photoacoustic and fluorescence imaging of her2 expression in breast tumors for diagnosis, margin assessment, and surgical guidance. *Molecular imaging*, 14(1):7290–2014, 2015.
- [121] Mhlambululi Mafu, Angela Dudley, Sandeep Goyal, Daniel Giovannini, Melanie McLaren, Miles J Padgett, Thomas Konrad, Francesco Petruccione, Norbert Lütkenhaus, and Andrew Forbes. Higher-dimensional orbital-angular-momentum-based quantum key distribution with mutually unbiased bases. *Physical Review A*, 88(3):032305, 2013.
- [122] Reza Nasiri Mahalati, Daulet Askarov, Jeffrey P Wilde, and Joseph M Kahn. Adaptive control of input field to achieve desired output intensity profile in multimode fiber with random mode coupling. *Optics express*, 20(13):14321–14337, 2012.
- [123] Reza Nasiri Mahalati, Ruo Yu Gu, and Joseph M Kahn. Resolution limits for imaging through multi-mode fiber. *Optics express*, 21(2):1656–1668, 2013.
- [124] Mohammad Mirhosseini, Omar S Magaña-Loaiza, Malcolm N O’Sullivan, Brandon Rodenburg, Mehul Malik, Martin PJ Lavery, Miles J Padgett, Daniel J Gauthier, and Robert W Boyd. High-dimensional quantum cryptography with twisted light. *New Journal of Physics*, 17(3):033033, 2015.
- [125] Edgar E Morales-Delgado, Salma Farahi, Ioannis N Papadopoulos, Demetri Psaltis, and Christophe Moser. Delivery of focused short pulses through a multimode fiber. *Optics express*, 23(7):9109–9120, 2015.
- [126] Edgar E Morales-Delgado, Demetri Psaltis, and Christophe Moser. Two-photon imaging through a multimode fiber. *Optics express*, 23(25):32158–32170, 2015.

- [127] Paul Morris, Andrew Hurrell, Adam Shaw, Edward Zhang, and Paul Beard. A fabry-pérot fiber-optic ultrasonic hydrophone for the simultaneous measurement of temperature and acoustic pressure. The Journal of the Acoustical Society of America, 125(6):3611–3622, 2009.
- [128] Mickael Mounaix, Daria Andreoli, Hugo Defienne, Giorgio Volpe, Ori Katz, Samuel Grésillon, and Sylvain Gigan. Spatiotemporal coherent control of light through a multiple scattering medium with the multispectral transmission matrix. Physical review letters, 116(25):253901, 2016.
- [129] Mickael Mounaix, Hugo Defienne, and Sylvain Gigan. Deterministic light focusing in space and time through multiple scattering media with a time-resolved transmission matrix approach. Physical Review A, 94(4):041802, 2016.
- [130] Claus B Müller and Jörg Enderlein. Image scanning microscopy. Physical review letters, 104(19):198101, 2010.
- [131] Mon Thiri Myaing, Daniel J MacDonald, and Xingde Li. Fiber-optic scanning two-photon fluorescence endoscope. Optics letters, 31(8):1076–1078, 2006.
- [132] Moussa N’Gom, Theodore B Norris, Eric Michielssen, and Raj Rao Nadakuditi. Mode control in a multimode fiber through acquiring its transmission matrix from a reference-less optical system. Optics letters, 43(3):419–422, 2018.
- [133] Shay Ohayon, Antonio Caravaca-Aguirre, Rafael Piestun, and James J DiCarlo. Minimally invasive multimode optical fiber microendoscope for deep brain fluorescence imaging. Biomedical optics express, 9(4):1492–1509, 2018.
- [134] Robert Olshansky. Mode coupling effects in graded-index optical fibers. Applied optics, 14(4):935–945, 1975.
- [135] Eben Olson, Michael J Levene, and Richard Torres. Multiphoton microscopy with clearing for three dimensional histology of kidney biopsies. Biomedical optics express, 7(8):3089–3096, 2016.
- [136] Taisuke Ota, Hiroya Fukuyama, Yasuhige Ishihara, Hideo Tanaka, and Tetsuro Takamatsu. In situ fluorescence imaging of organs through compact scanning head for confocal laser microscopy. Journal of biomedical optics, 10(2):024010, 2005.
- [137] Stephen W Paddock. Principles and practices of laser scanning confocal microscopy. Molecular biotechnology, 16(2):127–149, 2000.
- [138] Ioannis N Papadopoulos, Salma Farahi, Christophe Moser, and Demetri Psaltis. Focusing and scanning light through a multimode optical fiber using digital phase conjugation. Optics express, 20(10):10583–10590, 2012.
- [139] Ioannis N Papadopoulos, Salma Farahi, Christophe Moser, and Demetri Psaltis. High-resolution, lensless endoscope based on digital scanning through a multimode optical fiber. Biomedical optics express, 4(2):260–270, 2013.

- [140] Ioannis N Papadopoulos, Salma Farahi, Christophe Moser, and Demetri Psaltis. Increasing the imaging capabilities of multimode fibers by exploiting the properties of highly scattering media. Optics letters, 38(15):2776–2778, 2013.
- [141] Gregory B Passty. Ergodic convergence to a zero of the sum of monotone operators in hilbert space. Journal of Mathematical Analysis and Applications, 72(2):383–390, 1979.
- [142] Martin Plöschner, Tomáš Tyc, and Tomáš Čížmár. Seeing through chaos in multimode fibres. Nature Photonics, 9(8):529, 2015.
- [143] Florian Poisson, Nicolino Stasio, Christophe Moser, Demetri Psaltis, and Emmanuel Bossy. Multiple speckle illumination for optical-resolution photoacoustic imaging. In Photons Plus Ultrasound: Imaging and Sensing 2017, volume 10064, page 100641O. International Society for Optics and Photonics, 2017.
- [144] F Poletti, NV Wheeler, MN Petrovich, N Baddela, E Numkam Fokoua, JR Hayes, DR Gray, Zhihong Li, R Slavík, and DJ Richardson. Towards high-capacity fibre-optic communications at the speed of light in vacuum. Nature Photonics, 7(4):279, 2013.
- [145] SM Popoff, G Lerosey, R Carminati, M Fink, AC Boccara, and S Gigan. Measuring the transmission matrix in optics: an approach to the study and control of light propagation in disordered media. Physical review letters, 104(10):100601, 2010.
- [146] SM Popoff, Geoffroy Lerosey, Mathias Fink, Albert Claude Boccara, and Sylvain Gigan. Controlling light through optical disordered media: transmission matrix approach. New Journal of Physics, 13(12):123021, 2011.
- [147] L Raddatz, IH White, DG Cunningham, and MC Nowell. An experimental and theoretical study of the offset launch technique for the enhancement of the bandwidth of multimode fiber links. Journal of Lightwave Technology, 16(3):324, 1998.
- [148] Babak Rahmani, Damien Loterie, Eirini Kakkava, Navid Borhani, Uğur Teğın, Demetri Psaltis, and Christophe Moser. Competing neural networks for robust control of nonlinear systems. arXiv, pages arXiv–1907, 2019.
- [149] Babak Rahmani, Damien Loterie, Eirini Kakkava, Navid Borhani, Ugur Tegin, Demetri Psaltis, and Christophe Moser. Multimode fiber projection with machine learning. In Digital Holography and Three-Dimensional Imaging, pages HTu5B–3. Optical Society of America, 2020.
- [150] Babak Rahmani, Damien Loterie, Georgia Konstantinou, Demetri Psaltis, and Christophe Moser. Multimode optical fiber transmission with a deep learning network. Light: Science & Applications, 7(1):1–11, 2018.
- [151] Milind Rajadhyaksha, Melanie Grossman, Dina Esterowitz, Robert H Webb, and R Rox Anderson. In vivo confocal scanning laser microscopy of human skin: melanin provides strong contrast. Journal of Investigative Dermatology, 104(6):946–952, 1995.
- [152] David R Rivera, Christopher M Brown, Dimitre G Ouzounov, Ina Pavlova, Demirhan Kobat, Watt W Webb, and Chris Xu. Compact and flexible raster scanning multiphoton endoscope capable of imaging unstained tissue. Proceedings of the National Academy of Sciences, 108(43):17598–17603, 2011.

- [153] Sheryl Roberts, Markus Seeger, Yuanyuan Jiang, Anurag Mishra, Felix Sigmund, Anja Stelzl, Antonella Lauri, Panagiotis Symvoulidis, Hannes Rolbieski, Matthias Preller, et al. Calcium sensor for photoacoustic imaging. Journal of the American Chemical Society, 140(8):2718–2721, 2017.
- [154] Clemens Roider, Rainer Heintzmann, Rafael Piestun, and Alexander Jesacher. Deconvolution approach for 3d scanning microscopy with helical phase engineering. Optics Express, 24(14):15456–15467, 2016.
- [155] Stefan Rothe, Hannes Radner, Nektarios Koukourakis, and Jürgen Czarske. Transmission matrix measurement of multimode optical fibers by mode-selective excitation using one spatial light modulator. Applied Sciences, 9(1):195, 2019.
- [156] Stefan Rothe, Qian Zhang, Nektarios Koukourakis, and Jürgen W Czarske. Deep learning for computational mode decomposition in optical fibers. Applied Sciences, 10(4):1367, 2020.
- [157] Roland Ryf, Sebastian Randel, Alan H Gnauck, Cristian Bolle, Alberto Sierra, Sami Mumtaz, Mina Esmaeelpour, Ellsworth C Burrows, René-Jean Essiambre, Peter J Winzer, et al. Mode-division multiplexing over 96 km of few-mode fiber using coherent 6×6 mimo processing. Journal of Lightwave technology, 30(4):521–531, 2011.
- [158] Simon R Schultz, Caroline S Copeland, Amanda J Foust, Peter Quicke, and Renaud Schuck. Advances in two-photon scanning and scanless microscopy technologies for functional neural circuit imaging. Proceedings of the IEEE, 105(1):139–157, 2016.
- [159] Nadav Shabairou, Benjamin Lengenfelder, Martin Hohmann, Florian Klämpfl, Michael Schmidt, and Zeev Zalevsky. All-optical, an ultra-thin endoscopic photoacoustic sensor using multi-mode fiber. Scientific Reports, 10(1):1–8, 2020.
- [160] CJ R SHEPPARD. Super-resolution in confocal imaging. Optik (Stuttgart), 80(2):53–54, 1988.
- [161] CJR Sheppard and A Choudhury. Image formation in the scanning microscope. Optica Acta: International Journal of Optics, 24(10):1051–1073, 1977.
- [162] Colin JR Sheppard, Marco Castello, Giorgio Tortarolo, Takahiro Deguchi, Sami V Koho, Giuseppe Vicidomini, and Alberto Diaspro. Pixel reassignment in image scanning microscopy: a re-evaluation. JOSA A, 37(1):154–162, 2020.
- [163] Colin JR Sheppard, Shalin B Mehta, and Rainer Heintzmann. Superresolution by image scanning microscopy using pixel reassignment. Optics letters, 38(15):2889–2892, 2013.
- [164] Jaewook Shin, Bryan T Bosworth, and Mark A Foster. Compressive fluorescence imaging using a multi-core fiber and spatially dependent scattering. Optics letters, 42(1):109–112, 2017.
- [165] Sakshi Singh, Antonio M Caravaca-Aguirre, and Rafael Piestun. Focusing through a multi-mode fiber with selective mode control. In Mathematics in Imaging, pages MTu3C–5. Optical Society of America, 2017.

- [166] Siddharth Sivankutty, Esben Ravn Andresen, Rosa Cossart, Géraud Bouwmans, Serge Monneret, and Hervé Rigneault. Ultra-thin rigid endoscope: two-photon imaging through a graded-index multi-mode fiber. *Optics express*, 24(2):825–841, 2016.
- [167] Siddharth Sivankutty, Viktor Tsvirkun, Géraud Bouwmans, Dani Kogan, Dan Oron, Esben Ravn Andresen, and Hervé Rigneault. Extended field-of-view in a lensless endoscope using an aperiodic multicore fiber. *Optics letters*, 41(15):3531–3534, 2016.
- [168] Siddharth Sivankutty, Viktor Tsvirkun, Olivier Vanvincq, Géraud Bouwmans, Esben Ravn Andresen, and Hervé Rigneault. Nonlinear imaging through a fermat’s golden spiral multicore fiber. *Optics letters*, 43(15):3638–3641, 2018.
- [169] Erich Spitz and Alain Werts. Transmission des images à travers une fibre optique. *Comptes Rendus Hebdomadaires Des Seances De L Academie Des Sciences Serie B*, 264(14):1015–+, 1967.
- [170] Nicolino Stasio, Christophe Moser, and Demetri Psaltis. Calibration-free imaging through a multicore fiber using speckle scanning microscopy. *Optics letters*, 41(13):3078–3081, 2016.
- [171] Grzegorz Stepniak, Lukasz Maksymiuk, and Jerzy Siuzdak. Binary-phase spatial light filters for mode-selective excitation of multimode fibers. *Journal of lightwave technology*, 29(13):1980–1987, 2011.
- [172] Vivien Szabo, Cathie Ventalon, Vincent De Sars, Jonathan Bradley, and Valentina Emiliani. Spatially selective holographic photoactivation and functional fluorescence imaging in freely behaving mice with a fiberscope. *Neuron*, 84(6):1157–1169, 2014.
- [173] Alireza Tarighat, Rick CJ Hsu, Akhil Shah, Ali H Sayed, and Bahram Jalali. Fundamentals and challenges of optical multiple-input multiple-output multimode fiber links [topics in optical communications]. *IEEE communications Magazine*, 45(5):57–63, 2007.
- [174] Uğur Teğın, Babak Rahmani, Eirini Kakkava, Navid Borhani, Christophe Moser, and Demetri Psaltis. Controlling spatiotemporal nonlinearities in multimode fibers with deep neural networks. *APL Photonics*, 5(3):030804, 2020.
- [175] Johanna Trägårdh, Tomáš Pikálek, Mojmír Šerý, Tobias Meyer, Jürgen Popp, and Tomáš Čižmár. Label-free cars microscopy through a multimode fiber endoscope. *Optics express*, 27(21):30055–30066, 2019.
- [176] Santosh Tripathi, Richard Paxman, Thomas Bifano, and Kimani C Toussaint. Vector transmission matrix for the polarization behavior of light propagation in highly scattering media. *Optics express*, 20(14):16067–16076, 2012.
- [177] Sergey Turtaev, Ivo T Leite, Tristan Altwegg-Boussac, Janelle MP Pakan, Nathalie L Rochefort, and Tomáš Čižmár. High-fidelity multimode fibre-based endoscopy for deep brain in vivo imaging. *Light: Science & Applications*, 7(1):1–8, 2018.
- [178] Omer Tzang, Antonio M Caravaca-Aguirre, Kelvin Wagner, and Rafael Piestun. Adaptive wavefront shaping for controlling nonlinear multimode interactions in optical fibres. *Nature Photonics*, 12(6):368–374, 2018.

- [179] Omer Tzang, Eyal Niv, Sakshi Singh, Simon Labouesse, Greg Myatt, and Rafael Piestun. Wavefront shaping in complex media with a 350 khz modulator via a 1d-to-2d transform. Nature Photonics, 13(11):788–793, 2019.
- [180] George C Valley, George A Seffler, and T Justin Shaw. Multimode waveguide speckle patterns for compressive sensing. Optics letters, 41(11):2529–2532, 2016.
- [181] Ivo M Vellekoop. Feedback-based wavefront shaping. Optics express, 23(9):12189–12206, 2015.
- [182] Ivo M Vellekoop and AP Mosk. Focusing coherent light through opaque strongly scattering media. Optics letters, 32(16):2309–2311, 2007.
- [183] Andong Wang and Long Zhu. Deep learning based mode group recognition for mode division multiplexing in conventional multimode fiber. In 2019 Asia Communications and Photonics Conference (ACP), pages 1–3. IEEE, 2019.
- [184] Guoqing Wang, Chaitanya K Mididoddi, Fangliang Bai, Stuart Gibson, Lei Su, Jinchao Liu, and Chao Wang. Ultrafast optical imaging using multimode fiber based compressed sensing and photonic time stretch. arXiv preprint arXiv:1803.03061, 2018.
- [185] Yu Wang, Konstantin Maslov, Chulhong Kim, Song Hu, and Lihong V Wang. Integrated photoacoustic and fluorescence confocal microscopy. IEEE transactions on bio-medical engineering, 57(10):2576, 2010.
- [186] Robert H Webb. Confocal optical microscopy. Reports on Progress in Physics, 59(3):427, 1996.
- [187] Wolfgang Wiegand, Andreas A Thaer, Peter Kroll, Otto-C Geyer, and Alberto J Garcia. Optical sectioning of the cornea with a new confocal in vivo slit-scanning videomicroscope. Ophthalmology, 102(4):568–575, 1995.
- [188] Wen Xiong, Brandon Redding, Shai Gertler, Yaron Bromberg, Hemant D Tagare, and Hui Cao. Deep learning of ultrafast pulses with a multimode fiber. APL Photonics, 5(9):096106, 2020.
- [189] Amnon Yariv, John AuYeung, Dan Fekete, and David M Pepper. Image phase compensation and real-time holography by four-wave mixing in optical fibers. Applied Physics Letters, 32(10):635–637, 1978.
- [190] D Yelin, BE Bouma, SH Yun, and GJ Tearney. Double-clad fiber for endoscopy. Optics letters, 29(20):2408–2410, 2004.
- [191] Chao Zhang, Yong Zhang, Kai Hong, Shu Zhu, and Jie Wan. Photoacoustic and fluorescence imaging of cutaneous squamous cell carcinoma in living subjects using a probe targeting integrin $\alpha v \beta 6$. Scientific reports, 7:42442, 2017.
- [192] Benyuan Zhu, Thierry F Taunay, Man F Yan, Michael Fishteyn, George Oulundsen, and Durgesh Vaidya. 70-gb/s multicore multimode fiber transmissions for optical data links. IEEE Photonics Technology Letters, 22(22):1647–1649, 2010.

- [193] Peyman Zirak, Gregor Matz, Bernhard Messerschmidt, Tobias Meyer, Michael Schmitt, Jürgen Popp, Ortrud Uckermann, R Galli, Matthias Kirsch, MJ Winterhalder, et al. Invited article: A rigid coherent anti-stokes raman scattering endoscope with high resolution and a large field of view. APL Photonics, 3(9):092409, 2018.